(2)

Final Report
to the
Air Force Office of Scientific Research
on
Grant No. AFOSR F49620-88-C-0090

Experiments, Theory, and Simulation on the Evolution of Fabric in Granular Materials

Department of Theoretical and Applied Mechanics
Cornell University
Ithaca, New York 14853-1503

REPORT DOCUMENTATION PAGE

Form Approved
OMB No. 0704-0188

1. AGENCY USE ONLY (Leave blank)	2. REPORT DATE	3. REPORT TYPE AND DATES COVERED
	July 27, 1992	FINAL 8/1/88 - 12/31/91

4. TITLE AND SUBTITLE
EXPERIMENTS, THEORY, AND SIMULATION ON THE EVOLUTION OF FABRIC IN GRANULAR MATERIAL

5. FUNDING NUMBERS
F49620-88-C-0090

6. AUTHOR(S)
Jenkins, J.T.; Cundall, P.A.; and Ishibashi, I.

7. PERFORMING ORGANIZATION NAME(S) AND ADDRESS(ES)
Cornell University
Theoretical and Applied Mechanics
212 Kimball Hall
Ithaca, New York 14853-1503

8. PERFORMING ORGANIZATION REPORT NUMBER
2302
6.1102F

9. SPONSORING/MONITORING AGENCY NAME(S) AND ADDRESS(ES)
AFOSR / N A
Bldg 410
Bolling AFB DC 20332-6448

10. SPONSORING/MONITORING AGENCY REPORT NUMBER
F49620-88-C-0090
E80-8430

11. SUPPLEMENTARY NOTES
--

12a. DISTRIBUTION/AVAILABILITY STATEMENT
Approved for Public Release;
Distribution Unlimited

Approved for Public Release; Distribution Unlimited

12b. DISTRIBUTION CODE
UL

13. ABSTRACT *(Maximum 200 words)*

In this research, we have attempted to characterize the anisotropy in particle arrangement and particle interactions that develop when a granular material is deformed and to determine the influence of this anisotropy on the subsequent behavior of the material. The research has dealt with the behavior of an idealized granular material consisting of glass spheres and has involved the close interaction between physical experiments, numerical simulations, and the development of theory.

We have focused on: (1) Understanding the relationship between the developing anisotropy of the material and the changes in volume observed in deformations in which the mean stress is held constant. In particular, we have considered the volume change of a hollow cylindrical sample in triaxial compression and extension; (2) Using elastic waves to probe the evolution of the internal structure of the granular material as it is being deformed; and (3) Developing constitutive relations for general stress paths in the triaxial/torsional device through the combined efforts of theoretical modeling and numerical simulation.

14. SUBJECT TERMS	15. NUMBER OF PAGES
Granular material, fabric, volume change, boundary effects, wave propagation, anisotropic elasticity, numerical simulation, triaxial compression, polycrystalline plasticity	107
	16. PRICE CODE

17. SECURITY CLASSIFICATION OF REPORT	18. SECURITY CLASSIFICATION OF THIS PAGE	19. SECURITY CLASSIFICATION OF ABSTRACT	20. LIMITATION OF ABSTRACT
UNCLASSIFIED	UNCLASSIFIED	UNCLASSIFIED	SAR

Table of Contents

Introduction

James T. Jenkins

This final report provides an overview of the research accomplished during the course of the grant. It also serves as access to the publications resulting from the grant. In these publications, all aspects of the activity are elaborated upon. In this Introduction, we provide a summary of the accomplishments and indicate where more information can be found in the Chapters that follow.

In the research, we have attempted to characterize the anisotropy in particle arrangement and particle interactions that develop when a granular material is deformed and to determine the influence of this anisotropy on the subsequent behavior of the material. The research has dealt with the behavior of an idealized granular material consisting of glass spheres and has involved the close interaction between physical experiments, numerical simulations, and the development of theory.

We have focused on: (1) Understanding the relationship between the developing anisotropy of the material and the changes in volume observed in deformations in which the mean stress is held constant. (2) Using elastic waves to probe the evolution of the internal structure of the granular material as it is being deformed; and (3) Developing constitutive relations for general stress paths in the triaxial/torsional device through the combined efforts of theoretical modeling and numerical simulation.

Volume Change

The goal of the work on volume change was to develop an understanding of how various types of anisotropy induced in a granular material influence its volume change in subsequent deformations. Such an understanding should lead to a quantitative measure of the liquefaction potential of a saturated material.

Much of our effort has been to understand the volume change of a hollow cylindrical sample held at constant pressure in a triaxial/torsion device. The sample was found to expand when subjected to triaxial compression and contract when subjected to triaxial extension. The theory predicted such behavior only if there was anisotropy in the orientational distribution of contacts. Consequently, an effort was made in the simulations to establish an initial anisotropy in the orientational distribution of contacts alone. However, any such initial anisotropy disappeared when the material was loaded with an isotropic stress and the particles rearranged to accommodate it. The indication was that depositional anisotropy was not responsible

for the difference in the volume change in triaxial compression and extension.

In Chapter One, Ishibashi and Choi describe how it was determined that the methods used to prepare the sample might have induced an anisotropy that was impossible to reproduce in the numerical simulations. During the construction of the sample, regions of ordered grains may form near the boundaries of the mold resulting in a strong but localized anisotropy. Also, and perhaps more importantly, because of the difference between the boundaries at the ends and sides of the hollow cylindrical sample, it is likely that triaxial compression is strain controlled while triaxial extension is stress controlled. Consequently, there is an anisotropy associated with the experimental device.

Strain control in triaxial compression occurs because the rigid platens at top and bottom can exert contact forces of essentially arbitrary magnitude to impose the specified displacement. As a consequence, they support the development of load bearing particle chains along the axis of the sample. In contrast, the lateral membranes are limited in the magnitude of the contact force that they can support. The particle displacements must accommodate themselves to this, and, consequently, they are not controlled. In triaxial extension, load bearing particle chains are suppressed near the boundary. Expansion of the sample is assumed to be associated with anisotropy aligned in the major principal direction. In triaxial compression, this anisotropy is allowed to develop; in triaxial extension, it is not.

In Chapter Two, Cundall employs the numerical program FLAC to investigate the response of an isotropic, linear elastic material with elastic moduli that fluctuate in space about their average values. Holding the mean stress constant and using combinations of stress controlled and strain controlled boundaries, he determines the possible deformations of this isotropic but statistically inhomogeneous material. He finds that volume changes inevitably occur.

The implications for soils testing of hollow samples confined by lateral membranes and rigid end platens are rather profound. For these, stress paths between triaxial compression and extension involve a mixture of stress control and strain control. Consequently, along such paths information about the confinement is being confused with information about the material behavior. The solution is to employ thick-walled samples or to provide additional stiffening to the lateral boundaries.

Wave Propagation

The research on wave propagation has as it goal the determination of the anisotropy of the granular material from the measurements of the speeds of shear waves and pressure waves propagating through the material. This should lead to the capability of predicting the anisotropy of a granular material in the field.

Experiments involving wave propagation through a granular material during its deformation were carried out in a true triaxial/torsion device equipped as a resonant column and in a cubical cell with bending bimorphs as transducers. In both configurations the development of anisotropy with deformation could be determined from the wave speed measurements. In the cubical cell, the evolution of the complete set of elastic moduli could be followed. This research is described in detail in Chapter Three. The interpretation of the experiments was facilitated by the simultaneous development of theory and numerical simulations.

As outlined in Chapter Four, algorithms were developed for the optimal determination of the elastic constants of an anisotropic material from wave speed measurements. These are most easily implemented when the axes of anisotropy of the material is known beforehand, but can be applied to determine these axes in materials of the common symmetry classes. In the experiments on granular materials carried out so far, the algorithms have been employed to determine the elastic constants of a material in which a transverse isotropy is developing.

The theoretical calculations of Chapter Five, based on the mean field assumption, were used to determine the elastic constants of a random array of spheres in which the distribution of contacts exhibited transverse isotropy. The mean field assumption usually equates the rotation of particles and the displacement of the centers of neighboring particles to the average strain and rotation of the sample. However, the calculations show that when the contact distribution is anisotropic, in order to maintain a symmetric stress, it is necessary to permit the average rotations of the particles to differ from the average rotation of the sample. Using the resulting theory, wave speeds could be calculated and compared with numerical simulations and experiment.

The numerical simulation program TRUBAL was used to provide the effective moduli governing the wave propagation in an isotropic array. As discussed in Chapter Six, these numerical simulations were in good agreement with the moduli measured in the corresponding experiments, but the shear modulus was about one third that predicted by theory. In an effort to understand this discrepancy, the distribution of the normal component of the contact force was obtained from the simulation and found to be exponential. However the difference between the

measured and predicted wave speed did not have its origin in this distribution. What did become clear during the course of the simulation was the extent to which the detailed motions of individual particles differed from those consistent with the mean-field assumption.

Chapter Seven describes an attempt to characterize the local strains and rotations and to compare them to their average values. TRUBAL is used together with a least-squares procedure to determine the local strain, rotation, and displacement of the particles in a simulation. Increments in the average strain and rotation tensors calculated from the local values are compared with increments in the overall strain and rotation tensors. There is a surprisingly large difference between two kinds of averages.

We are presently carrying out similar simulations on larger samples in an effort to understand this discrepancy. In order to make correct quantitatively predictions of wave speeds as the anisotropy of a deforming granular material evolves, it seems necessary to characterize the deviations of the local particle displacements and rotations from those associated with the average strain and rotation and to incorporate measures of these deviations into the theory.

Constitutive Relations

The mean-field assumption was also used to determine the response of the material when is was subjected to triaxial compression and extension. A simplification of the Hertz-Mindlin contact law was assumed in which the tangential component of the contact force was assumed to depend linearly and reversibly on the tangential displacement of contacting spheres until frictional slip occlude. It was assumed that the shear strains were rather modest, never exceeding by much the volume strain associated with the isotropic part of the stress. In this case it is reasonable to suppose that the particle arrangement remains unchanged, although some contacts are effectively lost as their contact forces relax to zero.

The calculation of the stress-strain relation for triaxial compression is given in Chapter Eight. The predicted response of the material is in qualitative agreement with the experiments and numerical simulations, but it is again too stiff. The indication is that here, too, measures of the deviations from the mean field assumption must be incorporated into the theory.

The theoretical model also permits the calculation of the inelastic parts of the response such as the average plastic strain, the yield function, the plastic potential, and the hardening function, although the utility of these in describing the material must await our calculation of its behavior upon unloading.

An effort was begun to formulate theory for shear strains large compared to the volume strain associated with the pressure. Here substantial rearrangement of particle positions were expected to accompany the particles' sliding and rotation. In an effort to educate ourselves to the appropriate type of theory to employ, we turned to the literature on the polycrystalline plasticity. Here the elements of the aggregate are single crystals that deform and rotate by rate-independent slip. In trying to understand this subject, we found that we could contribute to it.

Chapter Nine describes a micromechanical theory for the development of orientational anisotropy in a simple planar polycrystalline aggregate comprised of single crystals with two slip planes. The introduction of the appropriate form of the mean-field assumption leads to an equation of evolution for the orientation of a single crystal which, in turn, may be used to determine the evolution of the distribution of orientations. Average properties can be calculated using the orientational distribution. A quantity of particular interest is the average plastic spin. When this quantity is calculated, its evolution is found to depend on only the second moment of the distribution function, the analog of the geometric fabric tensor in granular materials.

Similar calculations have been made in three dimensions for single crystals with an arbitrary number of slip planes and applied to face-centered cubic crystals. The analogous theory for frictional slip of random arrays of contacting spheres is presently being developed.

Publications Supported by the Air Force Office of Scientific Research on this Contract

Journal Articles

Castagnede, B., Jenkins, J.T., Sachse, W.S., and Baste, S. (1990) Optimal determination of the elastic constants of composite materials from ultrasonic wave-speed measurements. *Journal of Applied Physics 67*, p. 2753–2761.

Jenkins, J. T., and Strack, O. D. L. (1992) "Mean-field stress-strain relations for random arrays of identical spheres in triaxial compression," *Mechanics of Materials* (in press).

Prantil, V. C., Jenkins, J. T., and Dawson, P. R. (1992) An analysis of texture and plastic spin for planar polycrystals. *Journal of the Mechanics and Physics of Solids* (under review).

Zhang, Y., and Jenkins, J. T. (1992) The evolution of the texture of a polycrystalline aggregate. *Journal of the Mechanics and Physics of Solids* (under review).

Proceedings

Ishibashi, I., Agarwal, T. K., and Ashraf, S, A. (1989) Anisotropic behavior of glass spheres by a discrete element method and laboratory experiment. In Proceedings of the *First U. S. Conference on Discrete Element Methods.*

Castagnede, B. and Jenkins, J.T. (1989) Determination of the principal acoustic axes in anisotropic solids from wavespeed measurements. In *Wave Propagation in Granular Materials*, AMD-Vol. 101, (D. Karamanlidis and R.B. Stout, eds.) pp.107–115, ASME, New York.

Cundall, P.A., Jenkins, J.T., and Ishibashi,I. (1989) Evolution of elastic moduli in a deforming granular assembly. In *Powders and Grains* (J. Biarez and R. Gourves, eds.) pp. 319–322, A.A. Balkema: Rotterdam.

Jenkins, J.T., Cundall, P.A., and Ishibashi,I. (1989) Micromechanical modeling of granular materials with the assistance of experiments and numerical simulations. In *Powders and Grains* (J. Biarez and R. Gourves, eds.) pp. 257–264, A.A. Balkema: Rotterdam.

Agarwal, T. K., and Ishibashi, I. (1991) Multi-directional wave velocity measurements in dry granular materials using piezoelectric crystals. In *Recent Advances in Instrumentation in Soil Dynamics.* ASCE.

Ishibashi, I. , and Agarwal, T. K. (1991) Numerical experiments for anisotropic behavior of granular materials. In *Mechanics Computing in the 1990's and Beyond*, Volume 2. (H. Adeli and R. L. Sierakowski, Eds.) pp.1239–1243 ASCE: New York.

Jenkins, J. T. (1991) Anisotropic elasticity for random arrays of identical spheres. In *Modern Theory of Anisotropic Elasticity and Applications* (J. Wu, T. C. T. Ting, and D. M. Barnett, Eds.) pp. 368–377, SIAM: Philadelphia.

Jenkins, J. T., and Strack, O. D. L. (1992) Mean-field stress-strain relations for random arrays of identical spheres in triaxial compression. In *Advances in Micromechanics of Granular Materials* (H. Shen, et al., Eds.) pp. 41–50, Amsterdam: Elsvier.

Ishibashi, I. and Kiku, K. (1992) Change of directional rigidities of anisotropic granular materials by discrete element model. In Proceedings of the 27th National Meeting on Soil Mechanics and Foundation Engineering (in press).

Ishibashi, I. and Kiku, K. (1992) Liquefaction potentials of different anisotropic specimens by a discrete element model. In Proceedings of the 47th Annual Conference of the Japan Society of Civil Engineers (in press).

Prantil, V. C., Jenkins, J. T., and Dawson, P. R. (1992) Using orientation averaging to model plastic anisotropy for planar polycrystalline aggregates. In *MECAMAT'91* (in press).

Theses

Choi, J. W. (1991) An experimental study on anisotropic behavior of granular materials. *MS Thesis*, Department of Civil Engineering, Old Dominion University.

Agarwal, T. K. (1991) Micromechanics of granular materials and its relation to wave velocity. *Ph.D. Dissertation*, Department of Civil Engineering, Old Dominion University.

Prantil, V. C, (1992) An analytical description of macroscopic anisotropy for planar polycrystalline aggregates. *Ph.D. Dissertation.* Department of Mechanical and Aerospace Engineering. Cornell University.

Participants

Supported by the Air Force Office of Scientific Research

T. K. Agarwal
Graduate Student
Department of Civil Engineering
Old Dominion University

J. W. Choi
Graduate Student
Department of Civil Engineering
Old Dominion University

P. A. Cundall
Adjunct Professor
Department of Civil and Mineral Engineering
University of Minnesota

I. Ishibashi
Professor
Department of Civil Engineering
Old Dominion University

J. T. Jenkins
Professor
Department of Theoretical and Applied Mechanics
Cornell University

V. C. Prantil
Graduate Student
Department of Mechanical and Aerospace Engineering
Cornell University

Y. Zhang
Postdoctoral Associate
Department of Theoretical and Applied Mechanics
Cornell University

Participants Not Supported by AFOSR

B. Castagnede
Postdoctoral Associate
Department of Theoretical and Applied Mechanics
Cornell University

P. R. Dawson
Professor
Department of Mechanical and Aerospace Engineering
Cornell University

W. H. Sachse
Professor
Department of Theoretical and Applied Mechanics
Cornell University

O. D. L. Strack
Professor
Department of Civil and Mineral Engineering
University of Minnesota

Chapter One

Influence of Specimen Boundary and Shape on Volumetric Behavior of Granular Materials

Isao Ishibashi James T.Jenkins Jong W. Choi

Abstract

Laboratory shear tests were conducted on large and small glass bead assemblies with both stress and strain controlled lateral boundaries in both an ordinary solid cylinder triaxial device and in a hollow cylinder device. The specimens were sheared in triaxial compression and extension keeping the mean stress constant and volumetric strains were monitored. The results showed that (1) the mold used in preparing the specimen created a strong but localized ordering of particles at the specimen boundary and this type of initial fabric had a dominant effect on the volumetric behavior of the hollow cylinder specimens, and (2) the strain and the stress controlled boundaries produced significantly different volumetric strains, particularly at the initial stage of the shearing.

1 Introduction

During the past several years, the authors and co-researchers (Chen et al., 1988, Ishibashi et al., 1988, Jenkins, 1988, Cundall, 1988, Jenkins et al., 1989, Ishibashi et al., 1989, Ishibashi and Agarwal, 1991) have been investigating anisotropic behavior of granular materials, experimentally, numerically, and theoretically. A special focus was placed on the volumetric behavior along various stress paths. The stress paths that we have had a particular interest in are triaxial compression and extension tests

with constant mean stress (i.e., $(\sigma_1 + \sigma_2 + \sigma_3)/3 = \text{constant}$). Typical experimental volumetric strain data on assemblies of glass spheres from hollow cylinder tests (Chen et al., 1988) and ordinary solid cylinder triaxial tests (Ishibashi et al., 1989) are shown in Figure 1.

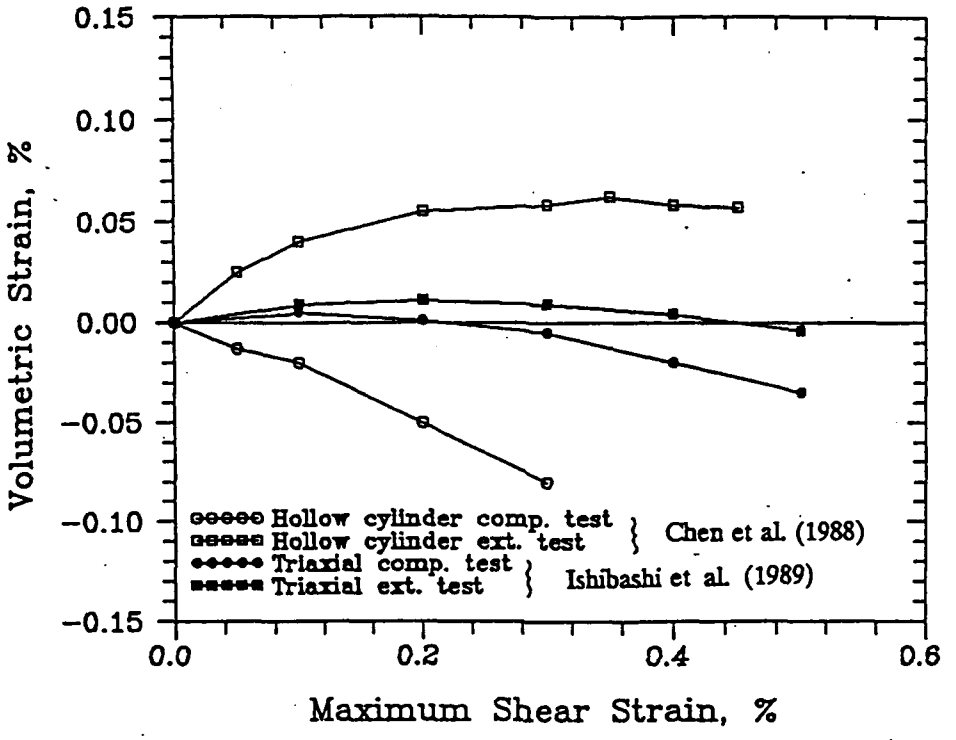

Figure 1: Volumetric strains of a fine glass bead assembly in triaxial compression and extension in hollow and solid cylinder specimens (Chen et al. (1988), Ishibashi et al. (1989)).

Figures 2 and 3 show computer simulated results using a discrete element code "TRUBAL" for nearly isotropic and highly anisotropic specimens (Ishibashi and Agarwal, 1991), respectively. Two questions were asked based on these results; (1) what is the reason for the big difference in volumetric strain between the triaxial compression and extension tests in the hollow cylinder specimen? and (2) why do total dilations occur at the beginning of shear in the triaxial compression tests in the hollow specimen and in triaxial extension in the numerical simulations but not in the solid cylinder specimens? The researchers made two hypotheses to explain the above phenomena; (1) hollow cylindrical specimens have a peculiar inherent fabric due to their relatively small thickness, and (2) the differences in the volumetric strain of the specimen may be attributed to the differences between the side and end boundary conditions. The first hypothesis was based on the observation that during the specimen preparation an ordered arrangement of the particles around the lateral

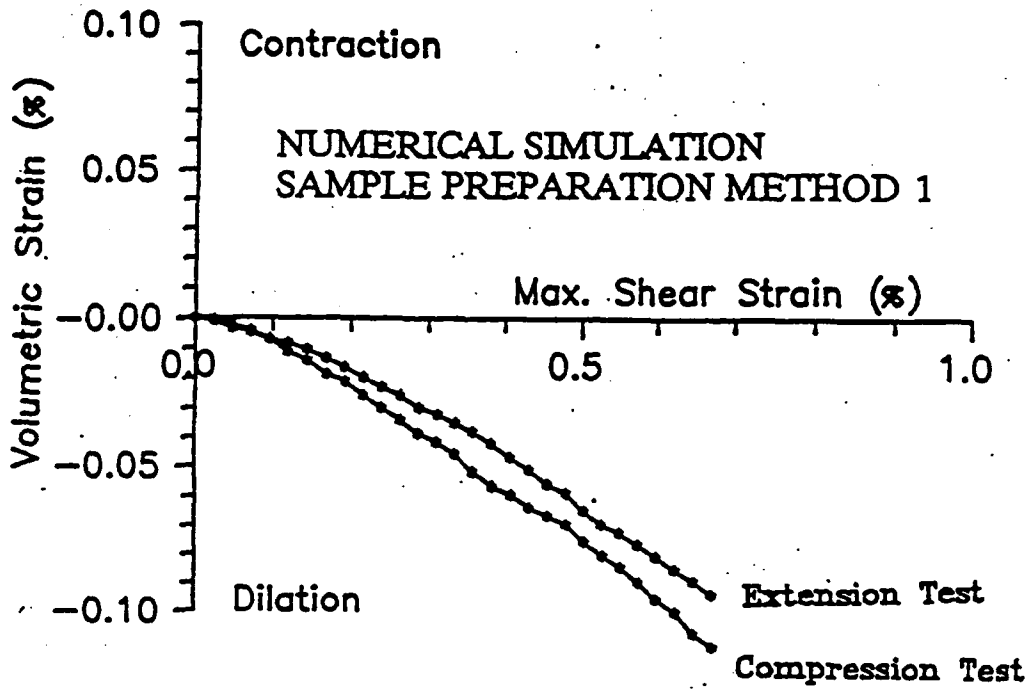

Figure 2: Computer simulated volumetric strain for an isotropic specimen (Ishibashi and Agarwal, 1991).

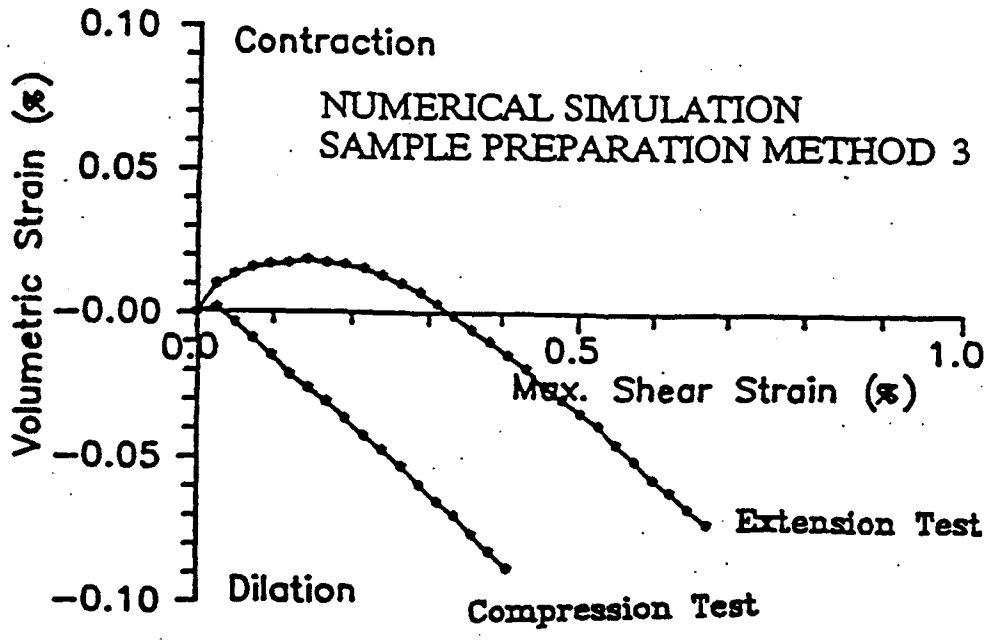

Figure 3: Computer simulated volumetric strain for a presheared specimen (Ishibashi and Agarwal, 1991).

boundaries of the molds might be created and thus the initial specimen might have a peculiar inherent fabric. Because in the hollow device the specimen is relatively thin in terms of particle diameters, the effect of these ordered boundary particles might have a significant influence on the entire volumetric behavior. The second hypothesis is based on the fact that in the triaxial specimen the top and bottom boundaries are made of rigid plates which induce a uniform displacement (strain controlled boundary), while the lateral confinement with thin rubber membranes imposes a stress that is limited in magnitude.

The authors reviewed a number of papers that employed similar testing conditions such as:

(a) Yamada and Ishihara, 1979,

(b) Haruyama, 1981,

(c) Hight et al., 1983,

(d) Ochiai and Lade, 1983,

(e) Miura et al., 1986,

(f) Sture et al., 1987, and

(g) Lam and Tatsuoka, 1988.

These testing devices included hollow cylindrical specimens (references (c) and (e) above), solid cylindrical specimens (reference (g) above), and cubical specimens (references (a), (b), (d) and (f) above). Those boundary conditions were stress boundaries (references (a) and (b) above) and mixed boundaries (references (c), (d), (e), (f) and (g) above). No experiments involving strain controlled boundaries were reported relevant to this study. It should be noted, however, that the numerical simulations by TRUBAL (Cundall, 1988, Ishibashi et al., 1989, Ishibashi and Agarwal, 1991) are purely strain controlled.

From this review no clear conclusions could be drawn regarding the effect of sample shape and the boundary conditions on the volumetric behavior, probably because the importance of these conditions was not recognized at the time of the experiments. However, some interesting and relevant observations were made. A dense hollow cylinder specimen preloaded in the vertical direction (Hight et al., 1983) and a loose specimen of glass beads in the cubical true triaxial device (Haruyama, 1981) showed a very similar volumetric behavior as that in Figure 1., while Yamada and Ishihara's cubical specimens (1979) for a loose river sand showed both contractive volume changes. Lam and Tatsuoka's experiment (1988) showed a clear effect of stress and strain boundaries in volumetric strain, although their tests were not under a constant mean stress.

2 Experimental Procedures

Two types of glass bead mixtures were used. The first mixture, called the "small bead assembly", was composed of two sizes of glass beads with 0.215 mm and 0.256 mm diameters in a number ratio of 1 to 1 or weight ratio of 1 to 1.688. The second mixture, called the "large bead assembly", was composed of two larger sizes of bead, 3 mm and 4 mm, in a number ratio of 4.728 to 1 or weight ratio of 2 to 1.

Two different specimen boundaries were created. For a lateral strain controlled boundary relatively rigid plastic or aluminum liners were employed. The plastic liner (126.0 mm high x 212.9 mm wide x 1.143 mm thick) is easily bent and was preshaped to the same curvature as the surface of the specimen. The aluminum liners consisted of eight pieces of longitudinal aluminum plates(126.0 mm high x 26.7 mm wide x 1.143 mm thick) that also had the same curvature as the surface of the specimen. The liners were placed around the specimen just inside of the membrane so that the confining pressure would be indirectly imposed on the specimen via the liners. The liners were used only in the solid specimens and not in the hollow specimens.

The majority of the experiments were conducted in a solid cylindrical triaxial compression device, which accommodated a specimen of about 71.8 mm in diameter and 152.4 mm in height. One series of tests was performed in a torsional simple shear apparatus (Chen et al., 1988), which employed a specimen with a 71.12 mm inside diameter, 101.6 mm outside diameter and about 142 mm in height.

All of the specimens were compacted (tamped) in equal layers, four for the solid specimens and five for the hollow specimens, to an average relative density of 60%. A burette was connected to the bottom for measuring the volume change of the fully saturated specimen.

Each specimen was isotropically consolidated from 34.5 kPa to 138 kPa prior to being sheared along the desired stress paths. For all tests, the mean effective stress, $(\sigma_1 + \sigma_2 + \sigma_3)/3$, was kept constant at 138 kPa throughout the shearing stage by controlling the vertical stress and the radial stress (equal to the tangential stress). The following results on volumetric strain were obtained after correcting for the penetration of the membrane into the voids of the glass beads at the boundary. A detailed discussion on the membrane penetration correction can be found in Choi and Ishibashi (1992).

3 Test Results

3.1 Vertical and Lateral Strains Under Isotropic Compression

Figures 4(a) and (b) show the relationship between the measured vertical strain ε_z and the calculated radial strain ε_r during isotropic compressions fo the small bead assemblies with lateral stress and strain controlled boundaries, respectively, in the solid triaxial device. The radial strain ε_r was calculated from measured volumetric strain ε_v and the vertical strain ε_z with an assumption of tangential strain ε_θ was equal to the radial strain ε_r. It is generally accepted that this assumption is a valid approximation for transversely anisotropic media. These figures show a nearly isotropic behavior except at the very beginning of the compression.

Figures 5(a) and (b) show the same relationships as Figures 4(a) and (b) but for the large bead assemblies. These figures show a highly anisotropic nature throughout the entire compression.

3.2 Volumetric Behavior During Triaxial Compression and Extension Tests

Figures 6(a) and (b) show the relationship between volumetric strain and the maximum shear strain for solid cylindrical assemblies of small beads with stress and strain controlled boundaries during triaxial compression and extension lateral tests. Both the triaxial compression and extension results are very similar.

Figures 7(a) and (b) show similar plots for the large beads. In contrast to Figures 6 (a) and (b), the extension test data shows a large initial contraction while the triaxial compression tests show very little (stress controlled lateral boundary) or no (strain controlled lateral boundary) initial contraction of the speciman. These specimen seem to be extremely anisotropic initially.

4 Discussion

4.1 Anisotropy Due to the Specimen Preparation Mold

The mold confinement during specimen preparation could create a strong anisotropic fabric in the vertical direction near the boundaries and the size of this region (the cross-hatched zones in Figure 8) will increase as the average grain size increases.

From this point of view, the large glass beads in the solid triaxial device are expected to provide a similar volumetric behavior to that from the hollow cylinder specimen with the small glass beads. This is because the maximum number of the large grains across the diameter of the solid specimen is 22 which is comparable to

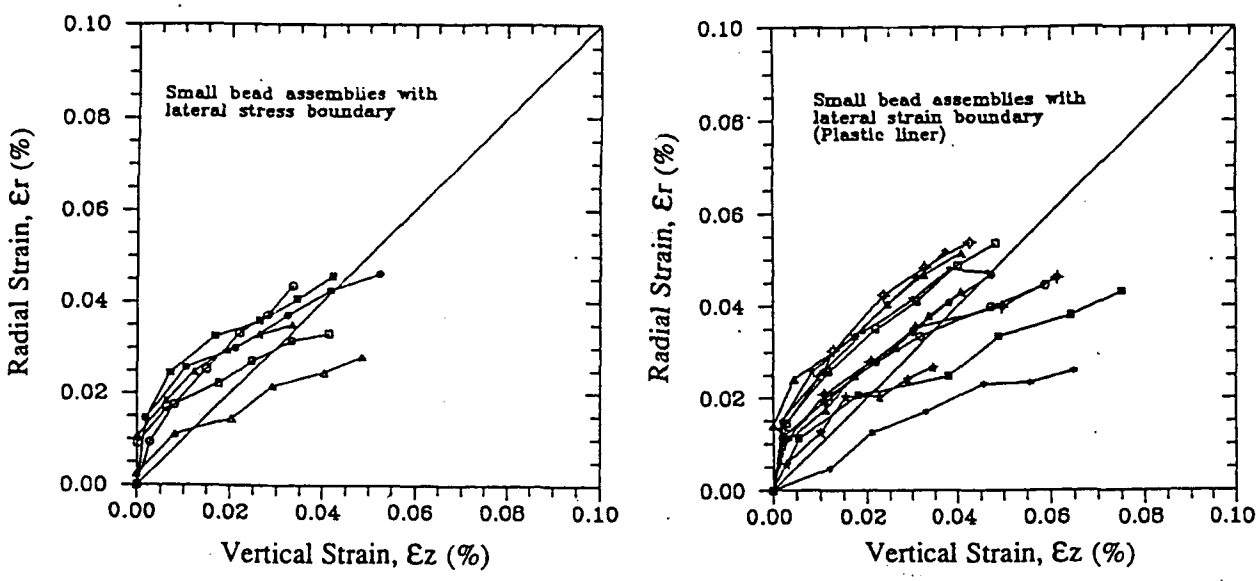

Figure 4: Relationship between radial and vertical strains under isotropic compression test for small bead assemblies: (a) lateral stress boundary, (b) lateral strain boundary

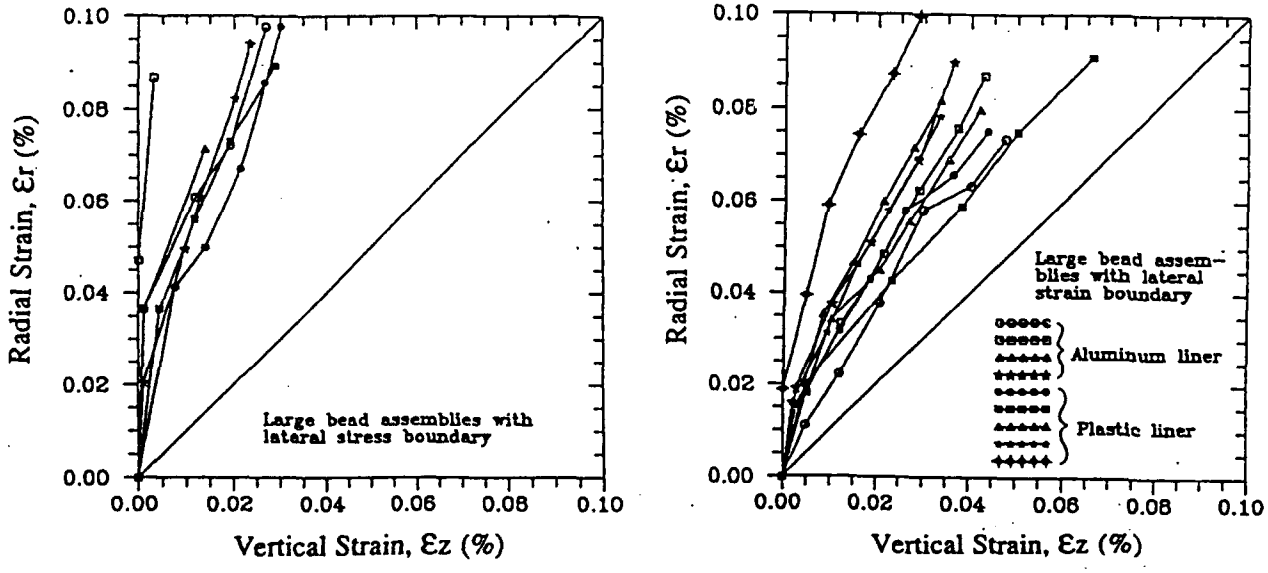

Figure 5: Relationship between radial and vertical strains under isotropic compression test for large bead assemblies: (a) lateral stress boundary, (b) lateral strain boundary.

70 small beads across the 15.2 mm thick wall of the hollow specimen. Meanwhile, in the solid specimen the maximum number of small galss beads across the diameter is about 308 so that the mold confinement effect should be small. Figure 9, which shows volumetric strains obtained from the hollow specimens, is consistent with the above observation. That is, Figure 9 is very similar to Figure 7(a).

As a demonstration, one solid specimen of small beads was presheared up to $\tau_{max} = 97$ kPa (or $\sigma_1/\sigma_3 = 3.58$) in triaxial compression and unloaded to the initial isotropic stress. A specimen with an induced fabric is expected to exhibit a strongly anisotropic volume change during reshearing. The results of reshearing are shown in Figure 10. The difference between two orthogonal stress paths (triaxial compression and extension) is remarkable, and these are very similar to the ones seen in Figures 7 and 9.

4.2 Boundary Effects

When the small bead assemblies with the stress controlled lateral boundary are compressed in the radial direction they seem to develop stronger force chains in the radial direction within a relatively narrow region at the outer boundary (refer to Figure 11).

Thus, the small bead specimens with both stress and strain controlled lateral boundaries show similar behavior when they have a comparable fabric (Figures 4 and 6). On the other hand, the large bead assemblies with the stress controlled lateral boundary showed larger strain in the radial direction as compared to the strain controlled lateral boundary (compare Figure 5(a) and (b)). The specimens with the two different lateral boundary conditions are supposed to have had a similar initial fabric. Thus, any changes in the isotropic compression test should be due to the difference in the boundary conditions. The more uniform stress distribution in the radial direction due to its stress controlled lateral boundary is thought to be responsible for the larger radial strain in isotropic compression (see Figure 5 (a)) and large initial contraction during the extension tests (see Figures 7 (a) and (b)). Uniformly distributed stress and the absence force chains may cause unstable internal structures, local mismatches, and collapse, and may lead to a radial larger strain than the vertical strain. In a large bead assembly there are not enough particle diameters inside the specimen to develop full force chains, in contrast to the small bead assembly.

In the cases of the triaxial compression tests, the average volumetric behaviors of two specimen with different particle sizes are similar to each other (compare Figures 6(a) and 7(a)), both showing and initial small densification and a rather high rate of dilation at a large strain. The fact that the specimens in these cases

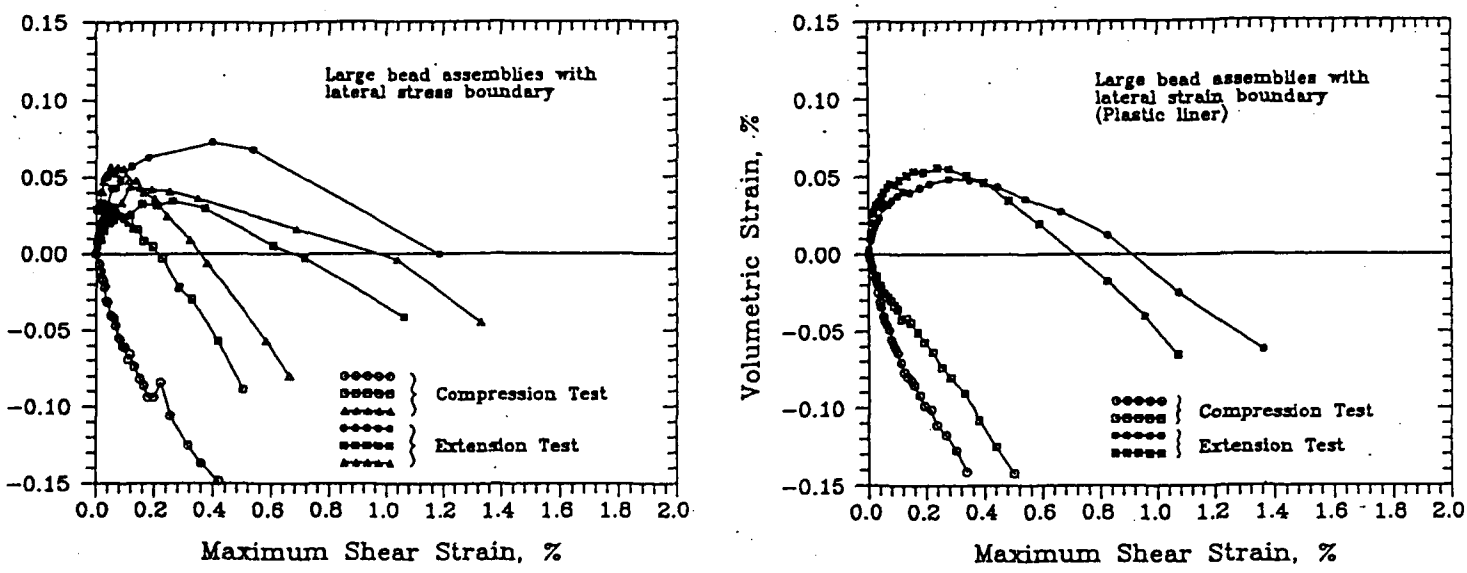

Figure 6: Volumetric strains of small bead assemblies in triaxial compression and extension: (a) lateral stress boundary, (b) lateral strain boundary.

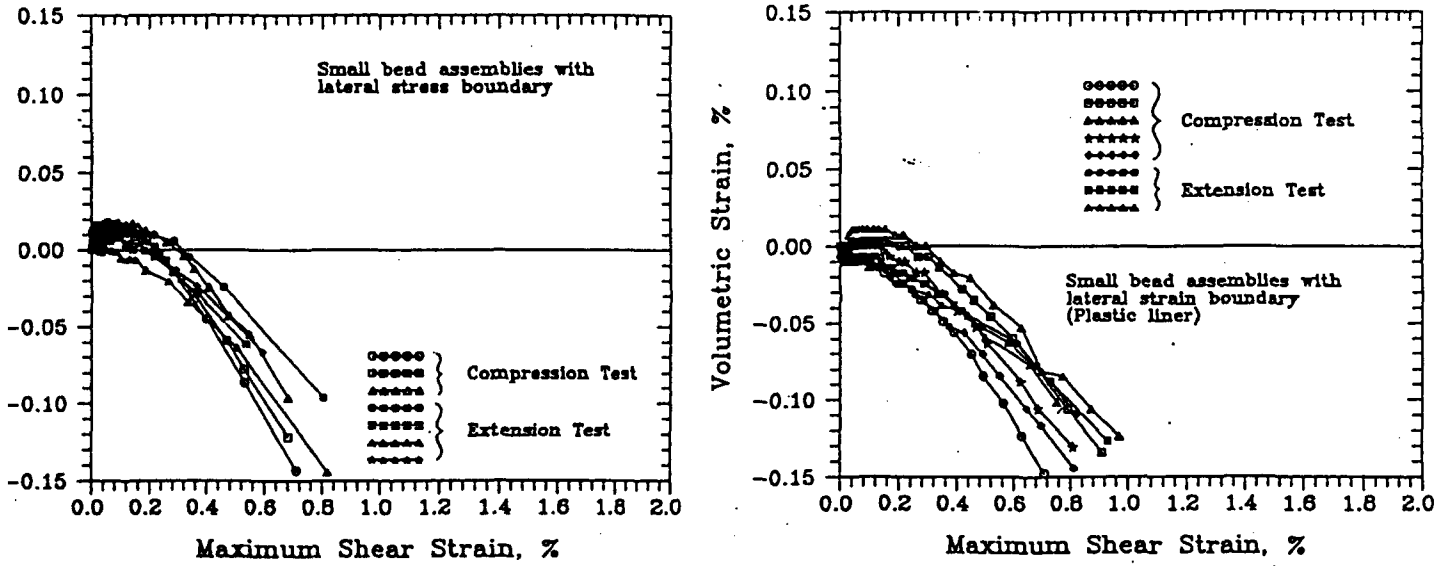

Figure 7: Volumetric strains of large bead assemblies in triaxial compression and extension (a) lateral stress boundary, (b) lateral strain boundary.

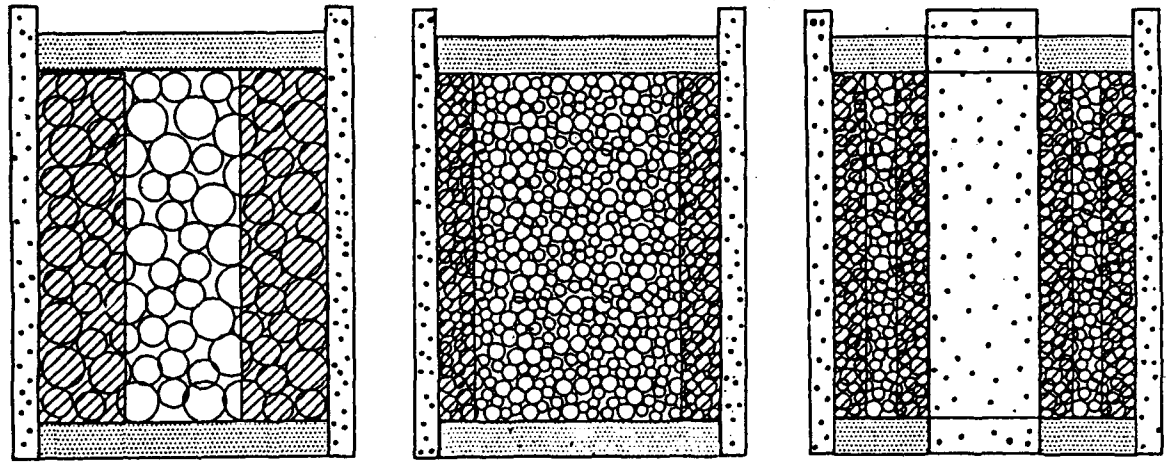

(a) Solid large bead assembly (b) Solid small bead assembly (c) Hollow small bead assembly

Figure 8: Solid and hollow cylinder specimens with specimen preparation molds.

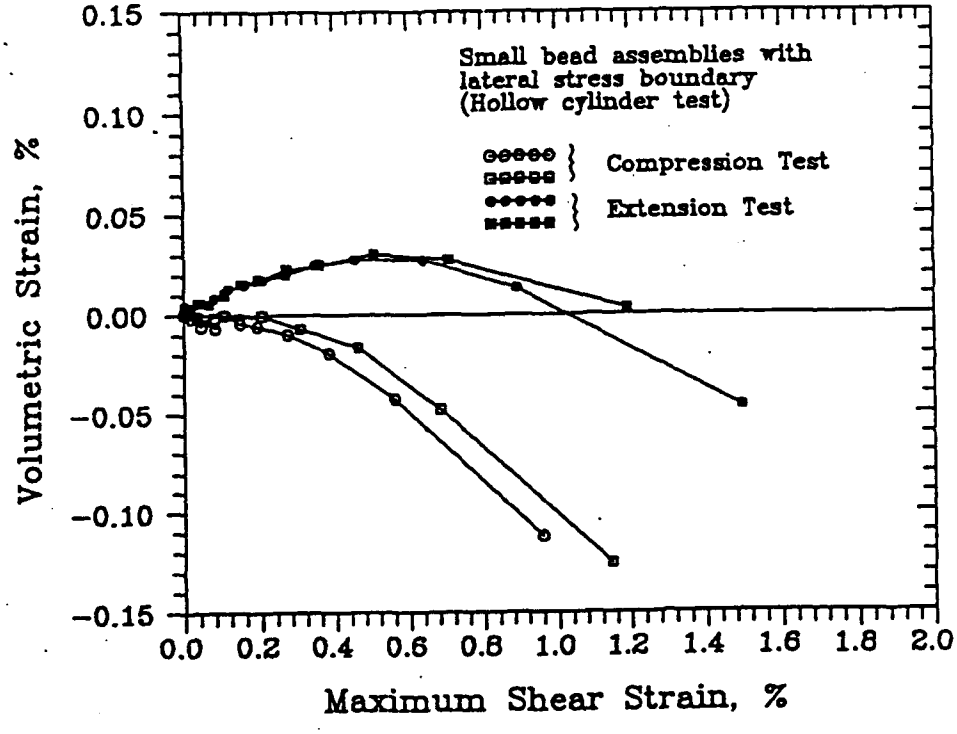

Figure 9: Volumetric strain for small bead specimens from hollow cylinder triaxial compression and extension tests.

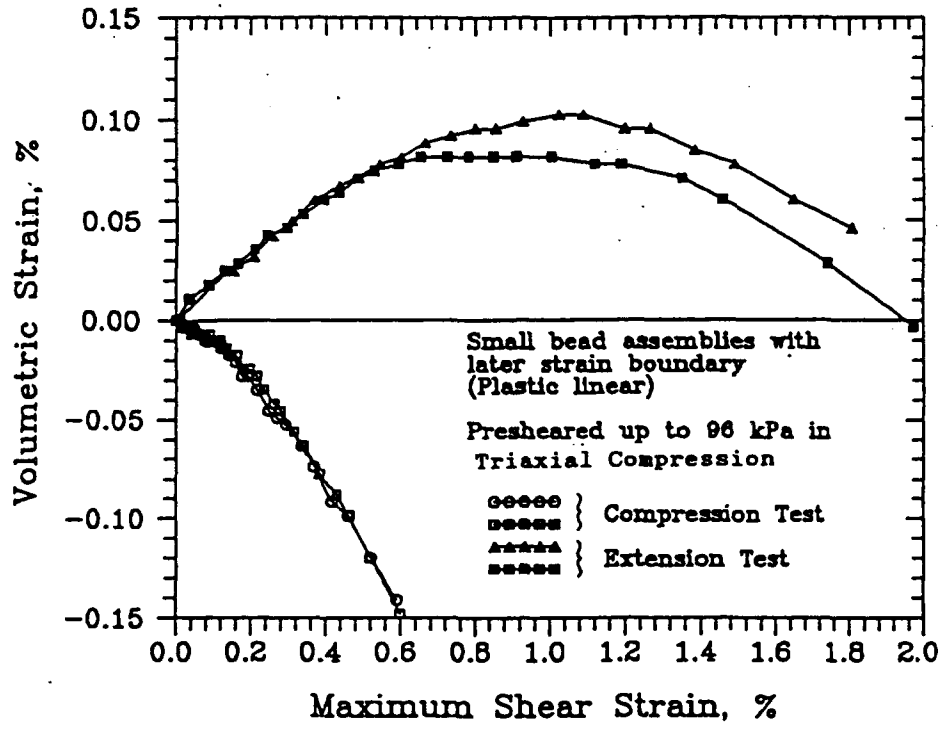

Figure 10: Volumetric strain for presheared small bead specimens in solid cylinder device.

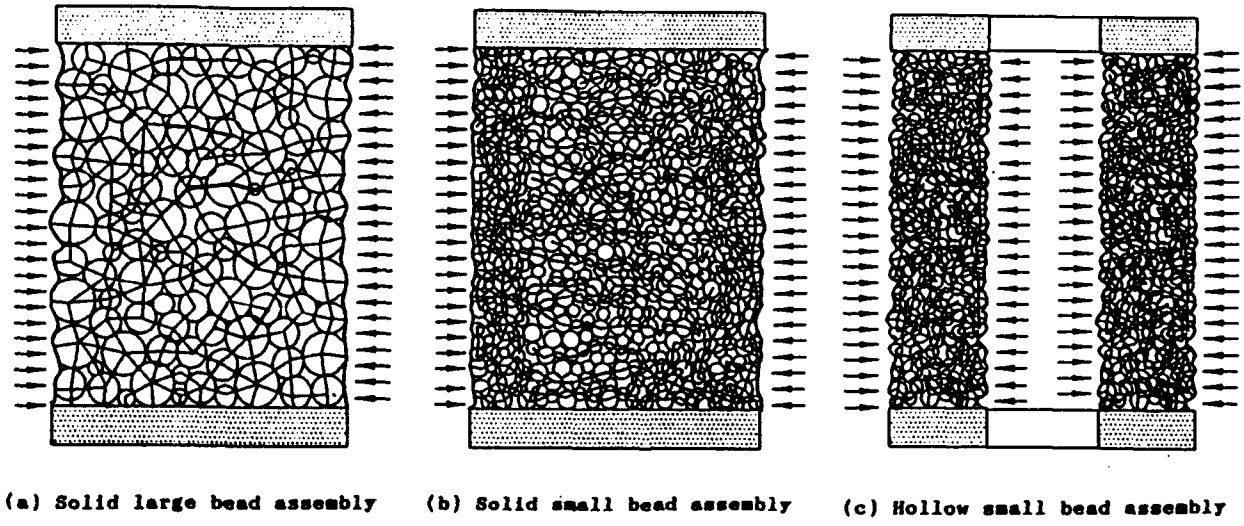

Figure 11: Schematic diagrams of force chains developed in various specimens during triaxial extension tests.

had rigid top and bottom platens suggests that similar force chains have developed to carry the major principal stress across the specimens in the vertical direction (see Figure 12).

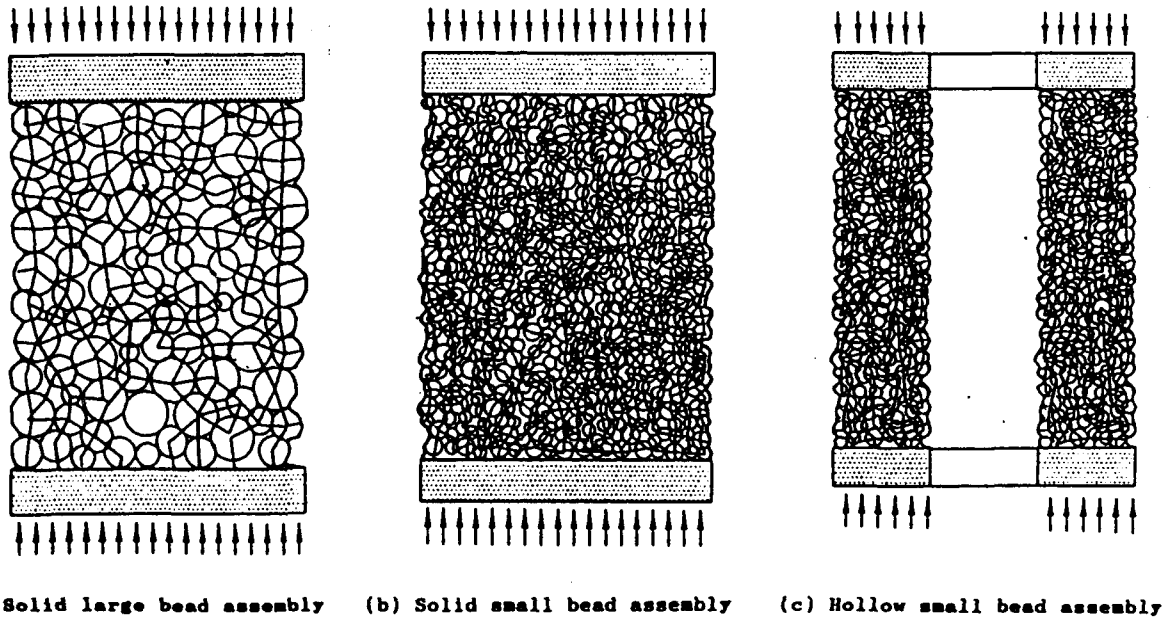

Figure 12: Schematic diagrams of force chains developed in various specimens during triaxial compression tests.

It is worth noting that there is rather large scatter in the data from the large bead assemblies (Figure 7(a)). This could be due to the insufficient number of grains in the radial directions which might lead to a greater deviation in internal structure. Another plausible explanation of the scatter is the variation in surface packing, which might require a unique membrane penetration correction for each test case.

5 Conclusions

From those experiments, the researchers' two hypotheses were found to be valid and the following conclusions can be made:

1. The preparation mold creates an ordered arrangement of particles and hence a strong but localized fabric around the lateral boundary. The thickness of material influenced by the mold increases as the grain size increases. Thus,

consideration of the specimen thickness relative to the grain size is important;

2. The strain controlled boundary and the stress controlled boundary produce different volumetric strains, particularly at the initial stage of the shearing. The strain controlled boundary applies different magnitude of forces to the particles in contact, and thus generate force chains through the specimen. The formation of strong force chains makes the specimen more expansive from the beginning. In contrast, the stress controlled boundary exerts a uniform forces on the particles causing local compaction and initial contraction of the specimen, and
3. The volumetric behavior of the thin-wall hollow cylinder specimens showed very similar behavior to the solid cylinder specimens with induced fabric by preshear. From this it can be concluded that the strong anisotropy in the hollow cylinder specimen stems mostly from a strong initial fabric created by the specimen preparation mold.

References

Chen, Y.C., Ishibashi, I. and Jenkins, J.T. (1988). Dynamics Shear Modulus and Fabric: Part I, Depositional and Induced Anisotropy, Geotechnique, 38, No. 1, pp.25–32.

Choi, J. W. and Ishibashi, I. (1992). An Experimental Method for Determining Membrane Penetration, Geotechnical Testing Journal, ASTM, Vol.15, No.4.

Cundall, P. A. (1988). Computer Simulations of Dense Sphere Assemblies, Micromechanics of Granular Materials, Elsevier, Amsterdam, ed. by M. Satake and J. T. Jenkins, pp. 113–123.

Haruyama, M. (1981). Anisotropic Deformation-Strength Characteristics of an Assembly of Spherical Particles Under Three Dimensional Stresses, Soils and Foundations, Japanese Society of Soil Mechanics and Foundation Engineering, Vol. 21, No. 4, pp. 41–55.

High, D. W., Gens, A., and Symes, M. J. (1983). The Development of a New Hollow Cylinder Apparatus for Investigating the Effects of Principal Stress Rotation in Soils, Geotechnique, 33, No. 4, pp. 355–383.

Ishibashi, I., Chen, Y.C. and Jenkins, J. T. (1988). Dynamic Shear Modulus and Fabric: Part II, Stress Reversal, Geotechnique, 38, No. 1, pp. 33–37.

Ishibashi, I., and Chen, Y.C. (1988). Dynamic Shear Moduli and Their Relationship to Fabric of Granular Materials, Micromechanics of Granular Materials, ed. by M. Satake and J. T. Jenkins, Elsevier, Amsterdam, Holland, pp. 113–123.

Ishibashi, I., Agarwal, T. K. and Ashraf, S. A. (1989). Anisotropic Behaviors of Glass Spheres by a Discrete Element Model and Laboratory Experiment, Proceedings of 1st U.S Conference on Discrete Element Methods, Golden, Co.

Ishibashi I. and Agarwal, T. K. (1991). Numerical Experiments for Anisotropic Behavior of Granular Materials, Mechanics Computing in 1990 and Beyond, ASCE Engineering Mechanics Specialty Conference, Columbus, Ohio, pp. 1239–1243.

Jenkins, J. T. (1988). Volume Change in Small Strain Axisymmetric Deformations of a Granular Materials, Micromechanics of Granular Materials, ed. by M. Satake and J.T. Jenkins, Elsevier, Amsterdam, pp. 245–252.

Jenkins, J. T., Cundall, P. A. and Ishibashi, I. (1989). Micromechanical Modeling of Granular Materials with the Assistance of Experiments and Numerical Simulations, Powders and Grains, ed. by Biarez and Gourves, Balkema, Rotterdam, pp. 257–264.

Lam W. K. and Tatsuoka, F. (1988). Effects of Initial Anisotropic Fabric and σ_2 on Strength and Deformation Characteristics, Soils and Foundations, Japanese Society of Soil Mechanics and Foundation Engineering, Vol. 28, No. 1, pp.89–106.

Miura, K., Miura, S., and Toki, S. (1986). Deformation Behavior of Anisotropic Dense Sand under Principal Stress Axes Rotation, Soils and Foundations, Japanese Society of Soil Mechanics and Foundation Engineering, Vol. 26, No. 1, pp.36–52.

Ochiai, H., and Lade, P. V. (1983). Three Dimensional Behavior of Sand with Anisotropic Fabric, Journal of Geotechnical Engineering Division, Vol. 109, No. 10, pp. 1313–1328.

Sture, S., Budiman, J. S., Ontuna, A. K., and Ko, H. Y. (1987). Directional Shear Cell Experiments on a Dry Cohesionless Soil, Geotechnical Testing Journal, ASTM, Vol. 10, No. 2, pp.71–79.

Yamada, Y. and Ishihara, K. (1979). Anisotropic Deformation Characteristics of Sand under Three Dimensional Stress Conditions, Soils and Foundations, Japanese Society of Soil Mechanics and Foundation Engineering, Vol. 19, No. 2, pp. 79–94.

Chapter Two

Volume Change in Inhomogeneous Samples

Peter A. Cundall

Abstract

Using the numerical program FLAC, we consider biaxial deformations of an isotropic linearly elastic material carried out at fixed means stress between combinations of rigid and flexible boundaries. We show that when the bulk and shear moduli vary in space in a quasi-random fashion, a change in the volume of the sample inevitably occurs.

1 Discussion

Physical triaxial tests exhibit behavior that is not observed in numerical simulations with TRUBAL or in the results of simple theoretical calculations: under constant mean stress, samples exhibit volume expansion during a compression test and volume contraction during an extension test. An explanation is proposed in Chapter One: in the compression test, the major principal stress is transmitted via rigid platens, whereas it is transmitted through a flexible membrane in the extension test. Force-chains are known to break down at a flexible boundary, but are preserved at a rigid boundary. Consequently, more "collapse"—and thereby volume decrease—occurs in the extension test.

Although the proposed explanation is expressed in terms of discrete force chains, a similar mechanism may occur if any type of inhomogeneity exists in a sample. To test this, the program FLAC [Cundall and Board, 1988; Cundall, 1989]

is used to simulate biaxial tests on inhomogeneous samples, with combinations of rigid and flexible boundaries. FLAC models a continuum, but each element may be assigned a different set of properties. In the tests described here, an istropic, linear elastic material is used—the bulk and shear moduli vary in space in a quasi-random fashion. In order to avoid mesh-dependence, the distribution of moduli is generated by a sum of spacial sine waves: the shortest wavelength is greater than the element size, and the longest wavelength is less than the sample size (which, in all runs, is 10 units). The shear modulus at any location (x,y) is computed as

$$G = G_o + A \sum_{n=1}^{50} \sin\left\{ \frac{2\pi\sqrt{(x_n^\circ - x)^2 + (y_n^\circ - y)^2}}{\lambda_n} \right\} \qquad (1)$$

where (x_n°, y_n°) is a random pair of numbers, chosen from a uniform random number distribution in the range $0 < x^\circ < 10$ and $0 < y^\circ < 10$. The wavelength is also chosen as a random number in the range $\lambda_{\min} < \lambda_n < \lambda_{\max}$. For all tests reported here, $\lambda_{\min} = 2$ units and $\lambda_{\max} = 10$ units. The bulk modulus was taken to be $5G/3$, corresponding to a Poisson's ratio of 0.25. Each element in the grid is assigned K and G according to its centroid location (x, y), using the given formula. The constants A and G_o in equation 1 are chosen so that there is no element in which G becomes zero or negative.

Figure 1 illustrates a typical distribution of shear moduli, with magnitude denoted by intensity of shading; note that the biaxial sample is square. A histogram of modulus values for a similar 50×50 sample is provided in Figure 2. Four tests are done for each sample, as shown in Figure 3.

Tests (a) and (b) have rigid platens at top and bottom; constant stress is applied to the side boundaries. The tests—extension and compression—are done by moving the rigid platens until the average platen stresses are equal and opposite to the applied side stresses. For a uniform sample, no net volume change is observed. However, in a non-uniform sample there is a volume decrease for the extension test and a volume increase for the compression test. For the case of an elastic material, these two volume changes are exactly equal and opposite, so only one test needs to be done, for each boundary condition. In order to eliminate the effects of anisotropy that may exist in the sample, two further tests are done, with the boundary conditions interchanged—these correspond to cases (c) and (d) of Figure 3. The results of all four cases are averaged, to give the final estimate of the volume change. In order to achieve the desired average platen stresses, a numerical servo-control is employed; this, and other special functions, are written in FLAC's embedded language, FISH. A sample data file is provided in the Appendix.

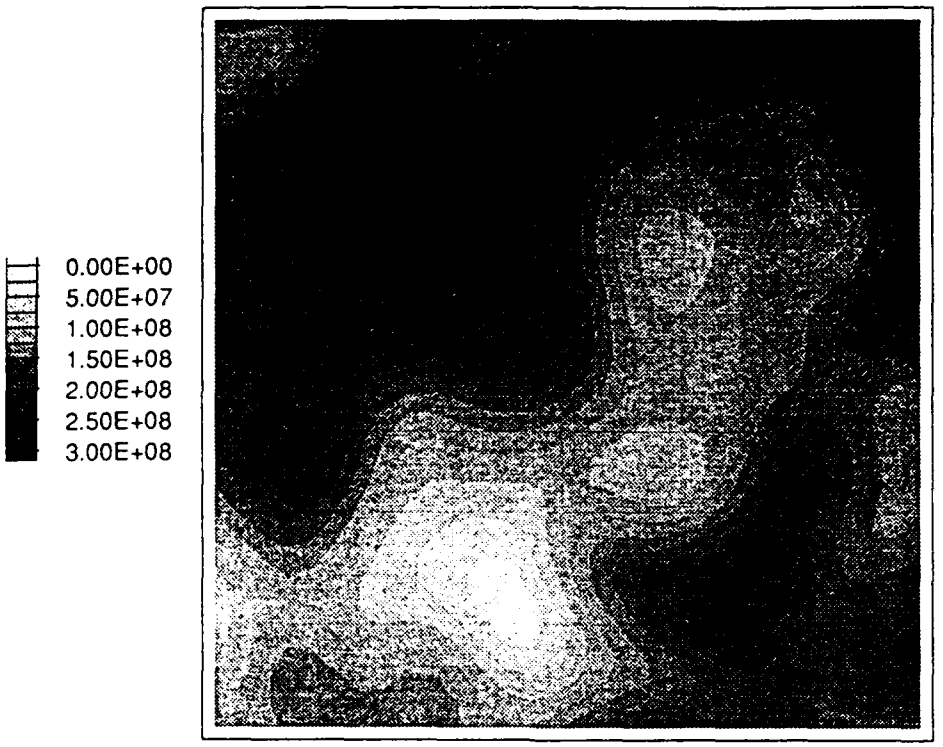

Figure 1: Shear modulus distribution – 30×30 sample

The total volume change is found from

$$\Delta V = \sum_{\text{all zones}} \frac{(\sigma_{11} + \sigma_{22} + \sigma_{33})\,\Delta x \Delta y}{3\,K} \tag{2}$$

where Δx and Δy are the element widths in x and y, respectively (the elements are rectangular). This formula was checked against a direct calculation involving displacements rather than stresses: the results were identical.

In all runs, a volume decrease was observed in the extension test, and an equal volume increase in the compression test. Results are expressed as the ratio, R, of volumetric strain to axial strain. The following table records the values of R for the same pattern of inhomogeneous moduli, but different grid sizes.

Grid	R
20×20	2.60×10^{-2}
30×30	2.74×10^{-2}
40×40	2.83×10^{-2}
50×50	2.90×10^{-2}

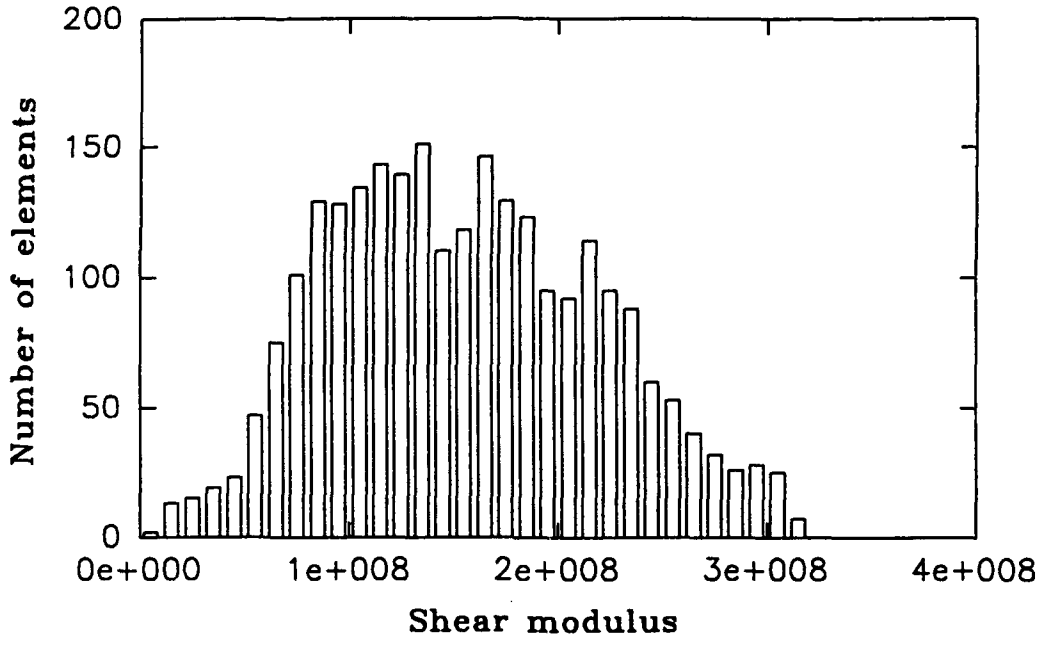

Figure 2: Histogram of shear modulus values – 50×50 sample

It is seen that the volume strain is rather small – around 3% of the axial strain. However, it is remarkable that volume strain occurs *at all* in a linear, elastic sample in which moduli vary in a smooth fashion. We might expect more of a "collapse" type of mechanism in a discrete, nonlinear material, where extreme local fluctuations in stiffness are present (in the form of chains of particles). As expected, the results tend towards an asymptotic value as the grid resolution is increased, suggesting that the measured volume change is a physical effect, rather than a numerical artifact.

Although the numerical experiments were intended to represent (in a smoothed-out way) the microscopic fluctuations in moduli of a granular material, it is possible to view the inhomogeneities as representing real nonuniformities introduced by the process of sample preparation. In this case, we might predict that physical samples would exhibit large variations in volume-change behavior, unless great care were taken in the preparation.

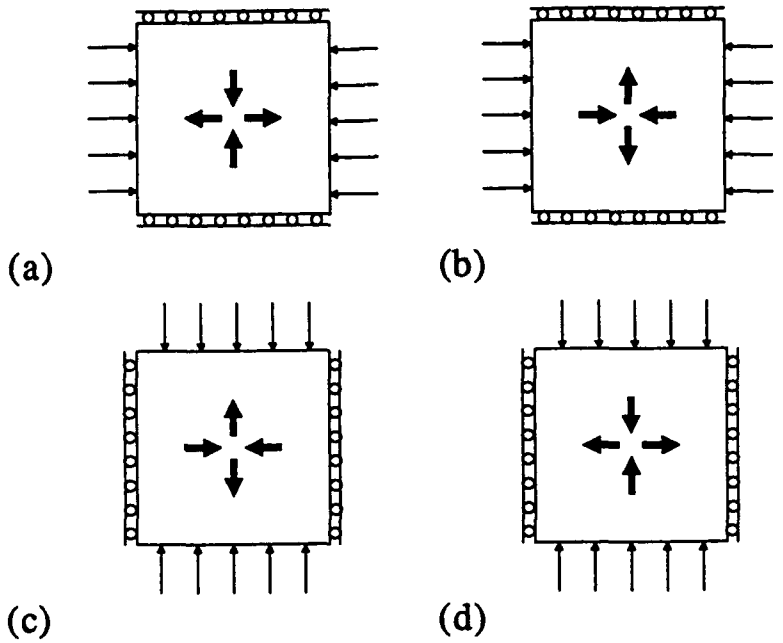

Figure 3: Four test configurations

References

Cundall, P.A. Numerical experiments on localization in frictional materials. Ingenieur-Archiv **59**: pp. 148–159, 1989.

Cundall, P.A. & M. Board. A microcomputer program for modelling large-strain plasticity problems. In: Swoboda, C. (Ed.) Numerical methods in geomechanics. Proc. 6th Int. Conf. on numerical methods in geomechanics, Innsbruck: pp. 2101–2108. Balkema, 1988.

APPENDIX: listing of FLAC data file for volume-change test

```
set log on
conf extra=5
g 30 30      ;Change this line, for different grid sizes
set echo off
gen 0,0 0,10 10,10 10,0
m e
prop dens=1000
;--- Sum of 50 spacial waves; wavelengths picked at random
;--- in the range L_min to L_max; positions are also random
def cover
  g_zero = 1.5e8
  top    = jgp
  right  = igp
  loop i (1,izones)
    loop j (1,jzones)
      shear_mod(i,j) = g_zero
    end_loop
  end_loop
  loop n (1,50)
    x0     = urand * 10.0
    y0     = urand * 10.0
    lambda = L_min + urand * (L_max - L_min)
    fac    = 2.0 * pi / lambda
    loop i (1,izones)
      loop j (1,jzones)
        xr = (x(i,j)+x(i+1,j)+x(i,j+1)+x(i+1,j+1))/4.0
        yr = (y(i,j)+y(i+1,j)+y(i,j+1)+y(i+1,j+1))/4.0
        z  = sqrt((x0-xr)^2 + (y0-yr)^2)
        shear_mod(i,j) = shear_mod(i,j) + amp * sin(fac * z)
        bulk_mod(i,j)  = shear_mod(i,j) * 5.0 / 3.0
      end_loop
    end_loop
  end_loop
;--- check on lower limit of G ---
  gmin = g_zero
  loop i (1,izones)
    loop j (1,jzones)
```

```
      gmin = min(gmin,shear_mod(i,j))
    end_loop
  end_loop
  command
; ---- smallest shear modulus is ...
    print gmin
; --- should reject run if gmin is negative or zero !!!
  end_command
end
;--- servo control to get mean stress to zero ---
def servo
  while_stepping
  sum   = 0.0
  nz2   = izones * jzones * 2.0
  loop i (1,izones)
    loop j (1,jzones)
      sum = sum + sxx(i,j) + syy(i,j)
    end_loop
  end_loop
  sum   = sum / nz2
  s_vel = min(gain*sum,0.0001)
  if yplat = 1 then
    loop i (1,igp)
      yvel(i,1)   =  s_vel
      yvel(i,jgp) = -s_vel
    end_loop
  else
    loop j (1,jgp)
      xvel(1,j)   =  s_vel
      xvel(igp,j) = -s_vel
    end_loop
  end_if
end
;--- analysis function ---
def analyse
  d_vol = 0.0
  loop i (1,izones)
    loop j (1,jzones)
```

```
      d_vol = d_vol + (sxx(i,j)+syy(i,j)+szz(i,j))/bulk_mod(i,j)
    end_loop
  end_loop
  d_vol = d_vol * x(2,1) * y(1,2) / 3.0
  if yplat = 1 then
    ax_strain = (ydisp(1,jgp)-ydisp(1,1)) / (y(1,jgp)-y(1,1))
  else
    ax_strain = (xdisp(igp,1)-xdisp(1,1)) / (x(igp,1)-x(1,1))
  end_if
  v_strain = d_vol / (x(igp,1) * y(1,jgp))
  rat      = v_strain / ax_strain
end
set echo on
; Fourier parameters -------------------
    set L_min=2 L_max=10  amp=1.0e7
; ---------------------------------------
cover
set gain=1e-8
save
; y-platen tests
set yplat=1
fix y j=1
fix y j=top
; extension test
tit
30*30 y=platen extension
;
appl p=1e5 i=1
appl p=1e5 i=right
his yvel i=1 j=1
his sum
step 3000
analyse
print d_vol, v_strain, ax_strain, rat
save yext.sav
;
rest
; x-platen tests
```

```
set yplat=0
fix x i=1
fix x i=right
; extension test
tit
30*30 x-platen extension
appl p=1e5 j=1
appl p=1e5 j=top
his xvel i=1 j=1
his sum
step 3000
analyse
print d_vol, v_strain, ax_strain, rat
save xext.sav
ret
```

Chapter Three

Anisotropic Elastic Constants of a Granular Assembly From Wave Velocity Measurements

Isao Ishibashi Tarun K. Agarwal

Abstract

Isotropic compression, triaxial compression, and triaxial extension tests on cubical granular specimens ($4'' \times 4'' \times 4''$) are performed in the laboratory. Concurrently, P-wave and S-wave velocities are measured along several directions relative to the principal stress axis in the specimen. Anisotropic elastic constants are recovered from those measurements. The recovered constants clearly showed the level of anisotropy at the different stages of the stress paths. Therefore the directional wave velocity measurements could be used as a useful tool to quantitatively identify the anisotropy of the granular assembly.

1 Introduction

The elastic constants of a granular assembly and the wave speeds through the media are fundamental macro-properties. These parameters can also be used effectively for comparison and validation of numerical and theoretical micromechanics models through experiments (Jenkins et al., 1988). A method for recovery of elastic constants from wave speed measurements is discussed in this paper. Theory for wave propagation in isotropic, homogeneous elastic material is readily available, however, wave propagation theory for anisotropic media has been dealt with very little. An effort is made to examine the existing theory, and its application to wave

velocity data obtained from granular media.

2 Elastic Theory of Wave Propagation

Elasticity and inertia are the properties of a medium essential for the transmission of waves. They are described by the following equations in tensor notation:

$$\text{(a) Equilibrium Equation} \qquad \sigma_{ij,j} + \rho f_i = \rho \ddot{u}_i \tag{1}$$

$$\text{(b) Constitutive Equation} \qquad \sigma_{ij} = C_{ijkl}\epsilon_{kl} \tag{2}$$

$$\text{(c) Strain-Displacement Equation} \qquad \varepsilon_{ij} = \frac{1}{2}(u_{i,j} + u_{j,i}) \tag{3}$$

where σ_{ij} and ε_{ij} are stress and strain tensors, repectively, C_{ijkl} is the fourth order constitutive tensor, u_i are diplacements, and f_i are body forces. One solution of the above equations is the plane wave:

$$u_k = Ad_k \exp[i\omega(x_p q_p - t)] \tag{4}$$

where ω is the real-valued angular frequency, i is unit imaginary number, q_p is the component of the slowness vector defined as n_p/c, with n_p a unit vector along the direction of propagation and c the velocity of propagation, x_p are the coordinates, and d_k is the direction of particle motion. Substituting for the strains and accelerations in terms of the displacement of a plane wave, the following solution emerges:

$$(C_{ijkl}q_j q_l - \rho\delta_{ik})d_k = 0 \tag{5}$$

$$\det|C_{ijkl}q_j q_l - \rho\delta_{ik}| = 0 \tag{6}$$

where δ_{ik} is the Kroneckor delta and the propagation tensor or Green-Christoffel stiffness matrix is defined by $\Gamma_{ik} = C_{ikjl}n_j n_l$. Equation (6) involves a determinant of a 3×3 matrix, and defines the eigenvalues that are related to three distinct wave speeds. These are the wave speeds of bulk waves propagating through the continuous media. The three waves are the pressure, or P, wave and two shear, or S waves. All three have mutual orthogonal displacement vectors that are the eigenvectors of the problem. In general, given C_{ijkl} and the direction of propagation n_j, the three wave velocities and the associated directions can be evaluated by solving the eigenvalue-eigenvector problem.

3 Recovery of Elastic Constants from Wave Velocity

The inverse problem of obtaining elastic constants from experimental data of wave propagation requires: (a) expanding the Equation (6) in terms of associated elastic constants E_{ij}, which are related to the elements of constitutive tensor C_{ijkl}; (b) obtaining wave speeds in multiple directions in experiments; (c) combining steps (a) and (b) for each wave speed and developing the nonlinear equation involving the direction cosines, wave speeds, elastic constants and material density; and (d) solution of the multiple nonlinear equations for the optimal evaluation of the elastic constants. The use of the Newton-Raphson procedure with a good initial guess gives an optimal solution. As described in Chapter Four, Castagnede and Jenkins(1989), and Castagnede et al. (1990) have applied this method to composites and crystals.

The number of elastic constants depends upon the type of symmetry in the material and can range from two for an isotropic material to 21 for a general elastic material without any symmetry. The number of wave speed measurements should be greater than the number of distinct elastic constants. For example, a transversely isotropic material described using five distinct elastic constants, will require five or more wave speed measurements. Greater redundancy in data provides higher accuracy in the optimized elastic constants.

The above procedure is a general approach, as wave paths can be selected in any plane in the continuum. A more simplified procedure requires that the measurements of the wave speeds be done in the principal material planes. For those wave paths, the cubic equation factorizes easily avoiding the complication of solving nonlinear equations. The three eigenvalues related to wave speeds are each obtained in separate relations involving the elastic constants, direction cosines of the wave paths, and the material density. The difference between the experimental velocity and the velocity from the elastic constants provides the error function. The summation of error functions from various wave speed directions is then minimized to obtain an optimal solution for the elastic constants. In the following we will discuss the theory for transversely isotropic materials.

A transversely isotropic stiffness matrix contains 5 distinct elastic constants. The stress-strain relation for such material is given as:

$$\begin{Bmatrix} \sigma_{11} \\ \sigma_{22} \\ \sigma_{33} \\ \sigma_{12} \\ \sigma_{13} \\ \sigma_{23} \end{Bmatrix} = \begin{bmatrix} E_{11} & E_{12} & E_{12} & 0 & 0 & 0 \\ E_{12} & E_{22} & E_{23} & 0 & 0 & 0 \\ E_{12} & E_{23} & E_{22} & 0 & 0 & 0 \\ 0 & 0 & 0 & E_{44} & 0 & 0 \\ & 0 & 0 & 0 & E_{44} & 0 \\ 0 & 0 & 0 & 0 & 0 & E_{66} \end{bmatrix} \begin{Bmatrix} \varepsilon_{11} \\ \varepsilon_{22} \\ \varepsilon_{33} \\ 2\varepsilon_{12} \\ 2\varepsilon_{13} \\ 2\varepsilon_{23} \end{Bmatrix} \quad (7)$$

where $E_{66} = \frac{1}{2}(E_{22} - E_{23})$ is a dependent elastic constant. Using the definition of the wave propagation tensor and the wave path in the 1-2 plane, the components of propagation tensor can be written as:

$$\Gamma_{11} = n_1^2 E_{11} + n_2^2 E_{44};\ \Gamma_{22} = n_1^2 E_{44} + n_2^2 E_{22};$$
$$\Gamma_{33} = n_1^2 E_{44} + \frac{1}{2} n_2^2 (E_{22} - E_{23}) \tag{8}$$
$$\Gamma_{12} = (E_{12} + E_{44}) n_1 n_2;\ \Gamma_{23} = 0; \quad \Gamma_{31} = 0 \tag{9}$$

When equation (6) is developed using the above stiffness matrix constants, one eigenvalue is trivial and relates to shear wave velocity:

$$\text{Shear wave:} \qquad \Gamma_{33} = \rho c^2 \rightarrow c_s = \sqrt{[n_1^2 E_{44} + \frac{1}{2} n_2^2 (E_{22} - E_{23})]/\rho} \tag{8}$$

The other two eigenvalues are obtained from the following equation:

$$(\rho c^2)^2 - (\Gamma_{11} + \Gamma_{22})\rho c^2 + (\Gamma_{11}\Gamma_{22} - \Gamma_{12}^2) = 0 \tag{9}$$

The solution of above equation gives the velocity of the two other waves as:

$$\text{P Wave: } \rho c_p^2 = \frac{1}{2}(-b_1 + \sqrt{b_1^2 - 4b^2}); \qquad \text{S wave: } \rho c_{sl}^2 = \frac{1}{2}(-b_1 - \sqrt{b_1^2 - 4b_2}) \tag{10}$$

where b_1 and b_2 are given by the following:

$$-b_1 = (\Gamma_{11} + \Gamma_{22}) = n_1^2(E_{11} + e_{44}) + n_2^2(E_{22} + E_{44}); \tag{11}$$
$$b_2 = (\Gamma_{11}\Gamma_{22} - \Gamma_{12}^2) = (n_1^2 E_{11} + n_2^2 E_{44}) + (n_1^2 E_{44} n_2^2 E_{22}) - (E_{12} + E_{44})^2 n_1^2 n_2^2 \tag{12}$$

In transversely isotropic materials, the 1-3 plane is similar to the 1-2 plane, hence the wave velocity—elastic constant relations are similar. Using the above relations, the least square error function can be written as the square of the difference of the experimental velocity and the theoretical velocity given by the above equations. The summation of the errors is done for all wave paths. This least square nonlinear problem is then solved using a modified Levenberg-Marquardt algorithm and a finite difference Jacobian from the IMSL library. The algorithm requires a good initial guess for the elastic constants, which is based on the expected ratio of the various elastic constants.

4 Wave Measurements Experiments

4.1 Cubic Shear Box

The generation and measurements of ultrasonic waves is done in a triaxial cubical box device with bender bimorphs as transducers (Agarwal and Ishibashi, 1991). The specimen is a $4'' \times 4'' \times 4''$ cube. Three independent normal stresses are applied through rubber bags installed inside three adjoining aluminum boundaries of the box by means of regulated water pressures. The other three boundaries of the box are made of solid lucite plates. The average axial strains are measured by the water replaced in the pressurized rubber bags. A glass sphere mixture (two sizes with average diameters of .215 mm and .256 mm and a weight ratio of 1.688 to 1) is used in the experiments. The dry mixture is loosely placed in the box by a spoon and compacted with a vibrating rod to the initial density (approximately 60% of relative density, equivalent porosity = 0.367).

4.2 Wave Path Configurations

All wave paths are located at the central section of the cube on the vertical planes as shown in Figure 1.

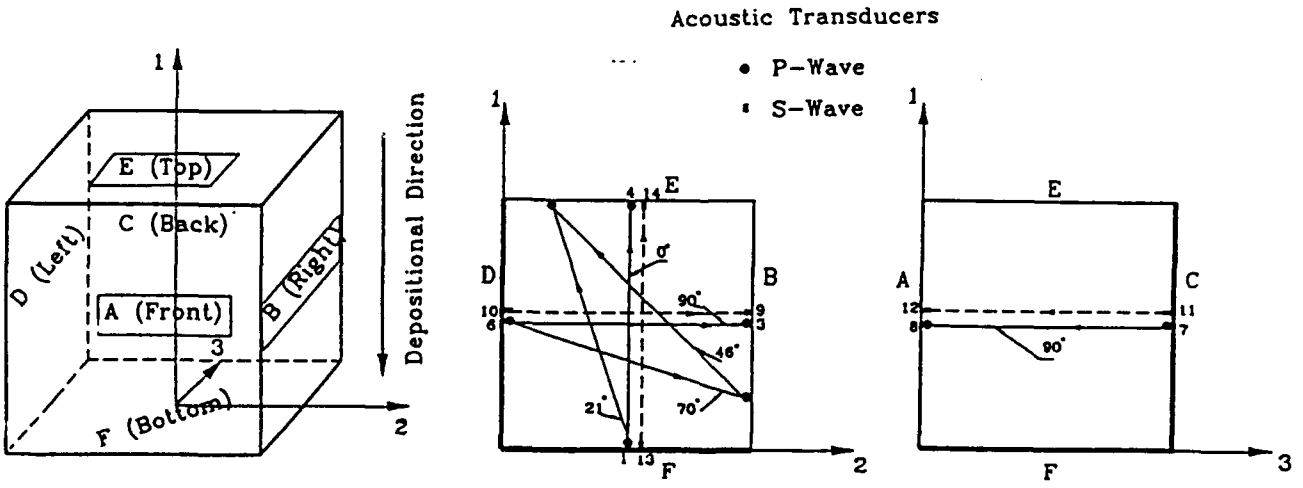

Figure 1: Wave Path Configuration

Overall, six wave paths for compression and three wave paths for shear are employed. The number of wave paths was selected based upon the five dynamic

elastic constants required for transversely isotropic granular assemblies. The shear waves propagate along three central axes of the cube.

4.3 Stress Paths

A specimen of granular material possess an initial anisotropy that is due to its deposition under gravity. This anisotropy is considered here to be transversely isotropic. This symmetry is also assumed for all applied stress paths as the paths are irrotational. In Test one, an isotropic stress is increased from 4 psi to 20 psi in increments of 4 psi. In Test two, after an isotropic consolidation of 20 psi, a compression test is conducted until failure maintaining a constant mean stress (20 psi). The vertical (axis 1) normal stress is increased while the normal stresses in two horizontal directions (axes 2 and 3) are decreased equally. In Test three, after an isotropic consolidation of 20 psi, the specimen is sheared in extension (a decrease in the vertical stress and equal increase in horizontal stresses), again maintaining a constant mean stress of 20 psi.

5 Results and Discussions

Wave speed measurements for P-waves (6 paths) and S-waves (2 paths) are presented in Tables I, II, and III. The angle β refers to the inclination of the wave path from the vertical in the vertical planes of propagation. The first five wave speed measurements are conducted in the 1-2 plane and the sixth wave path lies in the 1-3 plane. Both shear wave paths lie in 1-2 plane.

Table I shows that in all the measurements the wave velocities increase with increasing confining pressure. Different wave velocity measurements in the two orthogonal directions $= 0^o$ and $= 90^o$ indicate the existence of an inherent fabric formed during the deposition of the specimen. The strain under isotropic pressure showed that the specimen was more compressible in the horizontal direction than in the vertical direction as seen in Figure 2.

This is expected, since the deposition under gravity will induce a relatively larger number of contacts in the vertical direction and thus the specimen will be less compressible in that direction. In terms of the static elastic modulus, then, the specimen was softer in the horizontal direction than in the vertical direction. Similarly, wave speeds were larger in the vertical direction compared to those in the horizontal direction. It is noted, however, that Knox et al. (1982) conducted P-wave tests on the cubic specimens of sand that showed a higher wave velocity in the horizontal directions. It is difficult to explain their experimental data from consideration of the depositional fabric.

Table II shows wave velocities until near failure in the compression test. Upon

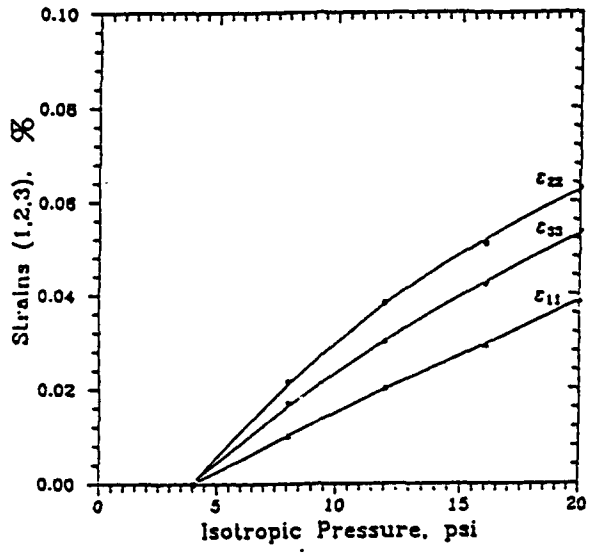

Figure 2: Strain responses during istoropic pressure test.

the application of 12 psi maximum shear stress, the increase in the P-wave velocity in the vertical direction is 5.4% while the decrease in P-wave velocity in the horizontal direction is between 13.4% and 10.7% . The two shear wave measurements show very small changes (a 5 to 6% drop). This is significantly different from the decreases in the shear wave velocity of 15% to 20% in the hollow cylindrical experiments (Chen et al., 1988).

Table III summarizes wave velocities for the extension test. The P-wave velocity drops by 16.9% in the vertical direction and increases by 9.7% in the horizontal direction during the shear. The shear wave velocity also shows greater changes compared to the compression test.

Table IV and Figure 3 show recovered elastic constants for the transversely isotropic specimen during the isotropic stress application.

Both dynamic elastic and shear modulus are larger in the 1-2 vertical plane than in the 2-3 horizontal plane. The changes in elastic modulus in two directions follow an often-used equation $E = K\sigma^{\alpha}$, where K and α are constants and σ is the isotropic confining stress. Values of K and α for different directions are calculated as follows: for E_{11}: $K = 351.0$, $\alpha = .169$; for E_{22}: $K = 225.1$, $\alpha = .255$; for E_{44}: $K = 87.7$, $\alpha = .296$; for E_{66}: $K = 79.6$, $\alpha = .325$. Tests conducted in hollow cylindrical samples (Chen et al., 1988) showed $\alpha = .40$ for the shear modulus in the

Table I: Wave velocity in m/sec during isotropic stress application.

Pressure (psi)	P_{12}-Wave at $\beta = 0°$	P_{12}-Wave at $\beta = 21°$	P_{12}-Wave at $\beta = 46°$	P_{12}-Wave at $\beta = 70°$	P_{12}-Wave at $\beta = 90°$	P_{13}-Wave at $\beta = 90°$	S_{12}-Wave at $\beta = 90°$	S_{12}-Wave at $\beta = 0°$
4	432.2	425.8	451.1	425.1	415.7	435.7	246.4	240.2
8	455.5	430.9	465.6	429.4	449.7	473.0	268.7	263.7
12	481.4	461.5	489.1	487.1	500.6	503.4	291.7	279.4
16	491.7	486.6	527.6	520.0	524.5	524.6	314.4	295.9
20	510.2	500.1	544.1	538.1	556.0	538.6	298.3	323.8

Table II: Wave velocity in m/sec during compression test.

Shear Stress (psi)	P_{12}-Wave at $\beta = 0°$	P_{12}-Wave at $\beta = 21°$	P_{12}-Wave at $\beta = 46°$	P_{12}-Wave at $\beta = 70°$	P_{12}-Wave at $\beta = 90°$	P_{13}-Wave at $\beta = 90°$	S_{12}-Wave at $\beta = 90°$	S_{12}-Wave at $\beta = 0°$
0	510.2	500.1	544.1	538.1	556.0	538.6	298.3	323.8
1.5	517.1	503.5	540.6	528.8	537.8	533.1	298.4	325.1
3.0	512.1	497.6	539.8	517.3	525.9	520.8	292.3	318.8
4.5	525.3	504.3	524.7	490.7	547.0	530.9	274.8	322.1
6.0	535.1	498.8	521.9	530.6	530.5	510.7	290.5	324.2
7.5	540.7	505.1	543.4	497.1	508.8	493.6	274.8	323.6
9.0	549.3	500.6	526.6	480.0	491.9	455.9	274.1	319.3
10.5	564.3	502.8	520.1	460.8	477.0	423.4	292.3	319.5
12.0	569.6	505.3	507.7	448.0	464.3	413.4	292.8	319.9

Table III: Wave velocity in m/sec during extension test.

Shear Stress (psi)	P_{12}-Wave at $\beta = 0°$	P_{12}-Wave at $\beta = 21°$	P_{12}-Wave at $\beta = 46°$	P_{12}-Wave at $\beta = 70°$	P_{12}-Wave at $\beta = 90°$	P_{12}-Wave at $\beta = 90°$	S_{12}-Wave at $\beta = 90°$	S_{12}-Wave at $\beta = 0°$
90	517.4	495.2	517.3	500.8	534.4	538.6	297.3	323.6
1.5	489.1	480.2	546.1	492.2	532.5	533.1	302.5	314.9
3.0	471.8	465.2	512.2	541.7	550.9	552.9	306.4	310.7
4.5	465.3	448.2	522.7	565.7	617.0	619.1	311.8	311.1
6.0	439.5	422.8	509.9	575.6	637.5	634.7	312.5	300.1
7.5	410.7	400.2	499.4	585.1	652.8	652.6	308.8	290.6
8.6	383.3	366.6	496.6	583.1	652.9	653.1	309.1	293.3

Table IV: Dynamic elastic constants in MPa during isotropic stress application.

Pressure (psi)	E_{11}	E_{12}	E_{22}	E_{44}	E_{66}
4	286.6	149.5	282.4	95.3	90.6
8	313.7	93.9	324.4	113.4	109.2
12	352.5	104.1	393.0	133.6	122.6
16	370.1	166.8	430.8	155.2	137.4
20	397.0	129.0	467.7	139.7	164.6

Table V: Dynamic elastic constants in MPa during compression test.

Shear Stress (psi)	E_{11}	E_{12}	E_{22}	E_{44}	E_{66}
0	397.0	129.0	467.7	139.7	164.6
1.5	407.4	122.5	448.4	139.8	165.8
3.0	398.0	140.2	427.3	134.1	159.5
4.5	425.1	55.9	438.6	118.5	162.8
6.0	427.0	77.8	432.3	132.5	165.0
7.5	435.9	127.5	390.6	118.5	164.4
9.0	444.2	103.9	351.6	118.0	160.1
10.5	463.8	83.2	317.2	134.2	160.3
12.0	473.3	49.7	301.4	134.6	160.7

Table VI: Dynamic elastic constants in MPa during extension test.

Shear Stress (psi)	E_{11}	E_{12}	E_{22}	E_{44}	E_{66}
0	410.2	45.1	440.7	138.8	164.4
1.5	364.6	140.4	430.2	143.6	155.6
3.0	341.0	76.3	478.9	147.5	151.6
4.5	330.7	0.0	585.1	152.6	151.9
6.0	293.3	0.0	616.5	153.3	135.4
7.5	256.7	0.0	639.7	149.7	123.0
8.6	217.3	0.0	638.1	150.0	118.7

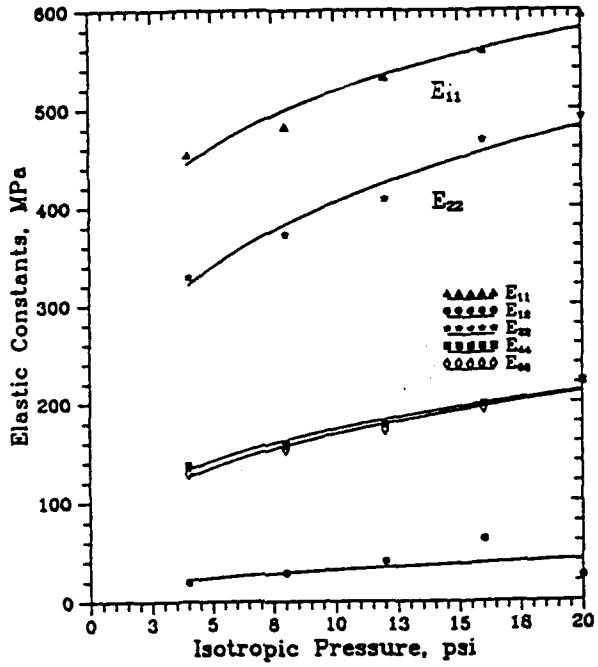

Figure 3: Dynamic elastic constants during isotropic pressure.

horizontal plane.

The elastic modulus E_{12} is found to change erratically with change in the pressure. The other elastic moduli follow much more systematic chages in magnitude. The exact identification of the shear wave arrival was difficult in some cases and this might have created some errors in E_{12}.

Table V shows elastic modulus during the compression test and Figure 4 plots the same data with respect to the maximum shear stress.

The increase in E_{11} is smaller than the decrease in E_{22}. This may indicate that the increase in number of contact normals in the vertical direction is low compared to the loss in number of contact normals in and around the horizontal plane. Note that overall contacts are lost during shearing in numerical tests (Ishibashi et al., 1989). These fabric changes are reflected only by moderate gains in elastic modulus in vertical direction (10.6%) and significant drops in horizontal modulus (29%). Therefore the dynamic elastic modulus is an important reflection of fabric changes inside the granular material during shear. The changes in shear modulus are 10% to 17%. In comparison, the tests with hollow cylindrical specimens has shown significant drops in shear modulus during shear. The difference in the wavelengths in the two type of tests could be a reason for this difference. In the cube specimens, the wavelength is about 10 particle diameters while the hollow cylindrical tests use

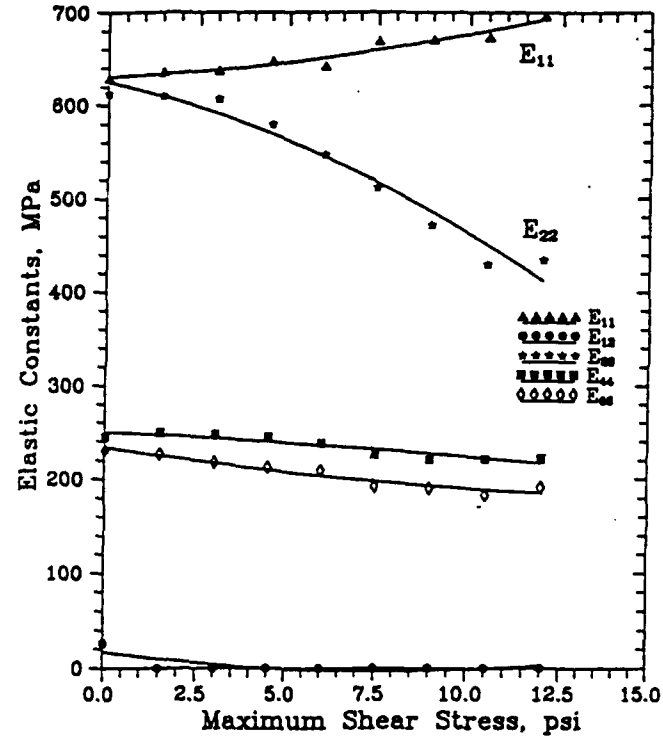

Figure 4: Dynamic elastic constants during compression test.

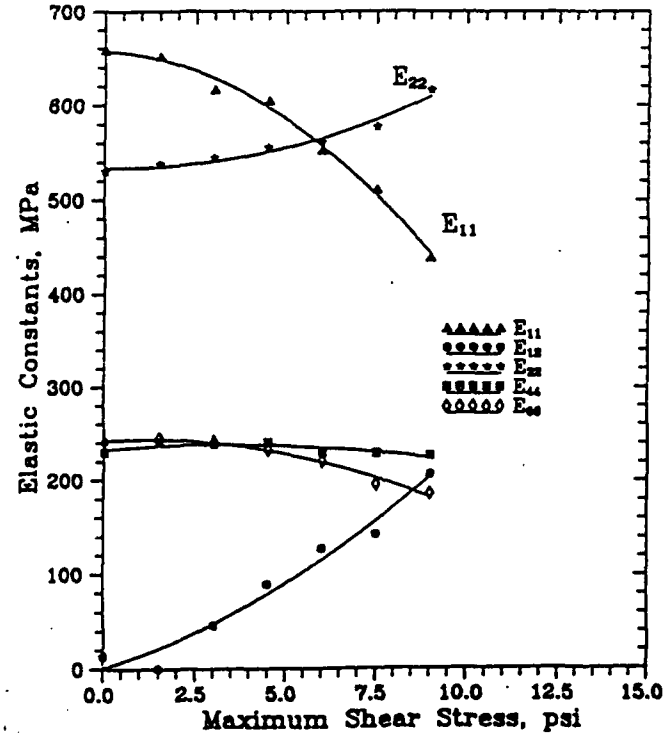

Figure 5: Dynamic elastic constants during extension test.

a wavelength of the order of specimen height (7.6 inches).

Table VI and Figure 5 show changes in elastic modulus during the extension tests. The changes in the two directional elastic modulus E_{11} and E_{22} are relatively large compared to the compression test. The specimen, initially has less contact normals in the horizontal direction compared to the vertical direction due to deposition under gravity. During the extension test, increases in the contact normals in the horizontal direction are significantly larger than the increases of contact normals in the vertical direction during the compression tests. This difference probably causes large increase in E_{22}. Simultaneously, the contact normals decrease in the vertical direction and thus the elastic modulus E_{11} reduces. The shear modulus in the horizontal plane shows reduction similar to the compression test. It should be noted that the initial isotropic stage of two specimens (Figures 4 and 5) are different and thus caused slightly dissimilar E_{11} and E_{22} values.

Conclusion

A general procedure for relating dynamic elastic constants of anisotropic materials to wave speeds is presented and detailed mathematical relations for transvesely isotropic specimens has been discussed. The approach is applied successfully to the multi directional wave speed measurements in cubic specimens of granular assembly of spherical particles for three different stress paths. In an isotropic stress test, the compression wave speeds in horizontal direction were lower compared to the speeds in the vertical direction due to depositional fabric. The recovered dynamic elastic moduli also followed this pattern. This behavior is similar to the static elastic modulus as is calculated from the three axial strain measurements. The recovered elastic moduli showed a systematic change during compression and extension tests. The importance of changes in internal structure as characterized by contact normals is qualitatively associated with the recovered elastic moduli. In summary, the evaluation of dynamic elastic moduli for granular assembly is a useful tool for studying internal character of granular materials.

References

Agarwal T.K., and Ishibashi, I (1991), "Multi Directional Wave Velocity Measurementsin Dry Granular Materials Using Piezoelectric Crystals," Proceedings of Session on Recent Advances in Instrumentation Data Acquisition and Testing in Soil Dynamics, ASCE Convention, Orlando, Florida.

Castagnede, B., and Jenkins, J.T. (1989), "Determination of the Principal Acoustic Axesin Anisotropic Solids from Wave Speed Measurements," *Wave Propagation in Granular Media*, ASME, AMD-Vol. 101, pp. 107–115.

Castagnede, B., and Jenkins, J.T., Sachse, W., and Baste, S. (1990), "OptimalDetermination of the Elastic Constants of Composite Materials from Ultrasonic Wave-Speed Measurements," *Journal of Applied Physics*, American Institute of Physics, Vol 67(6), pp. 2753–2761.

Chen, Y.-C., Ishibashi, I., and Jenkins, J.T. (1988), "Dynamic Shear Modulus and Fabric: Part I, Depositional and Induced Anisotropy," *Géotechnique*, Vol. 38, No. 1, pp. 25–32.

Ishibashi, I., Agarwal, T.K., and Ashraf, S.A. (1989), "Anisotropic Behaviors of GlassSpheres by A Discrete Element Model and Laboratory Experiments," First U.S. Conference on Discrete Element Methods, Golden, Colorado.

Jenkins, J.T., Cundall, P.A., and Ishibashi, I. (1988), "Micromechanical Modeling ofGranular Materials with the Assistance of Experiments and Numerical Simulations," In Powder and Grains (Biarez, J., and Gourvés, R., Eds., Balkema, Rotterdam, pp. 257–264.

Knox, D.P., Stokoe II, K.H., and Kopperman, S.E. (1982), " Effect of State of Stress onVelocity of Low-Amplitude Shear Waves Propagating along Principal State Directionsin Dry Sand," Research Report 82–83, Department of Civil Engineering, University of Texas at Austin, pp. 420.

Chapter Four

Determination of the Principal Acoustic Axes in Anisotropic Solids from Wavespeed Measurements

B. Castagnede J.T. Jenkins

Abstract

We outline and provide references to procedures that are employed to determine the anisotropy of linearly elastic solids from experimental measurements of the speeds of elastic waves propagating through them and apply one of the numerical methods to the analysis of some data. We indicate how the procedures might be extended to characterize the anisotropy of a granular material.

1 Disscussion

Prediction of the incremental behavior of a homogeneous sample of a granular material requires information about its current state. The identification of the variables that characterize the state of the materials is currently an area of active research, *e.g.* (**1**). Certain to be included on any list of state variables are the porosity and stress. Other candidates are the orientational distribution of contacts and contact area. The hope is that measurements of wavespeed and attenuation in relatively homogeneous samples can help to characterize the state subsequent to some loading history. For example, Chen, et al. (**2,3**) measure the speed of a shear wave propagating down the axis of a hollow cylindrical sample in a torsional/triaxial device. They relate the observed decrease in wavespeed with increasing deviatoric stress to a net loss of contacts associated with the development of anisotropy. Here

we wish to discuss how wavespeed measurements in classical linear elastic solids can provide rather complete characterizations of the acoustic anisotropy. Our expectation is that similar methods can be employed to determine the evolving anisotropy in granular materials.

An elastic solid is typically produced with a symmetry that does not change when the material is subjected to small strains. An example is an epoxy matrix reinforced by parallel fibers. The linear elastic behavior is governed by the stiffness tensor C_{ijkl} that relates the stress t_{ij} and the infinitesimal strain e_{kl} :

$$t_{ij} = C_{ijkl} e_{kl}. \tag{1}$$

Because of the symmetry of the stress and the strain, the stiffness tensor satisfies the conditions $C_{ijkl} = C_{jikl} = C_{ijlk}$. The existence of a strain energy provides the additional condition $C_{ijkl} = C_{klij}$. Other reductions in the number of independent components of the stiffness, or the elastic constants, depend upon the symmetry of the material (**4**).

If the solid is subjected to a large deformation, its symmetry is, in general, changed. For example, if the epoxy composite is greatly compressed in a direction perpendicular to the fibers, its symmetry is transformed from hexagonal to orthorhombic. The description of wave propagation through a material that is experiencing a large deformation is complicated by the presence of the stress t^0_{ij} that maintains the deformation. In this case the increment t'_{ij} of stress associated with the wave results from both the additional increment of strain e_{ij} and the increment in the antisymmetric part w_{ij} of the displacement gradients,

$$t'_{ij} = w_{ik} t^0_{kj} - t^0_{ik} w_{kj} + (1/2)(e_{ik} t^0_{kj} + t^0_{ik} e_{kj}) - e_{kk} t^0_{ij} + C_{ijkl} e_{kl}, \tag{2}$$

where the stiffness tensor C_{ijkl} depends upon the symmetry of the finitely deformed material (**5**).

The situation in granular materials is complicated by the fact that a part of the anisotropy that is induced by a history of deviatoric stress remains upon unloading. However it is precisely this anisotropy that endows the material with the memory of its history. The difficulty is that this anisotropy does not, in general, fall into one of the common classes (**6**). Nevertheless we think that it is worthwhile to review existing schemes for the determination of the elastic constants and the orientation of the principal acoustic axes in crystals and in anisotropic engineering materials. This is a very practical problem that has been studied and solved for various material symmetries using numerous numerical methods.

When the symmetry of the material is known, the symmetry axes induce a natural orthonormal basis. The directions parallel to these vectors are called the

principal acoustic axes. The elastic constants are to be determined, so we need to write down the characteristic equation associated with propagation in a direction with cosines n_i,

$$\det |\Gamma_{ij} - \rho v^2 \delta_{ij}| = 0. \tag{3}$$

Here Γ_{ij} is the Green-Christoffel tensor, given by

$$\Gamma_{ik} = C_{ijkl} n_j n_l, \tag{4}$$

ρ is the density of the material, δ_{ij} is the Kronecker delta, and v is the wavespeed of a bulk mode.

When the acoustic axes of the material are not known, these equations are still valid, but the natural basis is unavailable. The direction cosines n_i' are then given with respect to some other basis convenient to the experiment:

$$n_i' = a_{ij} n_j, \tag{5}$$

where a_{ij},the transformation matrix, is given in terms of Euler angles (**7**) that must be determined as part of the solution to the problem.

Equation (3) is a cubic equation for the eigenvalues of the propagation tensor, ρv^2. These eigenvalues are measured experimentally for a number of orientations n_i'. Then, in order to obtain the elastic constants of the material, equation (3) must be inverted.

To accomplish this inversion, several methods have been proposed during the last 40 years including:

A numerical procedure (**8**) and series expansion (**9**);

Approximations valid near the principal axes of symmetry (**10**);

Perturbation series expansion with an iterative numerical method (**11–15**);

Use of the three invariants of the Christoffel matrix (**16**, **17**); and

Algebraic manipulations of the characteristic equation (**18**, **19**).

In the general case, the use of this last method provides a new cubic equation (**20**, **21**) for the determination of the column vector X_A of unknown elastic constants.

$$(1/3!) A_{ABC} X_A X_B X_C + (1/2!) B_{AB} X_A X_B + C_A X_A + D \doteq 0 \tag{6}$$

where the dimension of X_A ranges from 3 for cubic symmetry to 21 in triclinic materials. The coefficients depend upon the density, the direction cosines, and the

Euler angles. They are given elsewhere (**21**) for the hexagonal and orthohombic symmetries.

Generally, the systems of equations (**6**) is overdetermined, as there is more experimental data than unknown elastic constants. An optimal solution of the overdetermined system is obtained using a Newton-Raphson numerical scheme. The recovery of the Euler angles has been achieved using this method or other procedures for various systems of symmetry. The problem has been solved for the cubic (**17**, **22**), the hexagonal (**21**) and even for the more intricate monoclinic (**23**, **24**) systems.

When the type of symmetry is not known, equation (6) may still be employed with the dimension of X_A taken to be the number of independent elastic constants of a candidate symmetry. If the material exhibits more symmetry, the calculated stiffness tensor will be seen to have fewer independent components than initially expected (**25**). Using such a procedure, experimental data on some engineering materials may be fit equally well by either of two symmetries. In granular materials we expect this to be the case more often than not, but we anticipate greater difficulty in recognizing what symmetry we may be close to.

2 An Example

The above approach is illustrated in one of the simplest cases, the recovery of a single Euler angle for the hexagonal system of symmetry. This, for example, is the case when considering the recovery of the alignment of the fibers in a unidirectional composite material. Figure 1 provides the geometry for this problem when dealing with a thin plate of the composite. We suppose that this plate was cut with an angular parallax θ_{23} and that this parameter is unknown. The idea is then to propagate elastic waves in the planes $(1, 2')$ and $(1, 3')$ and assume them to be principal planes. In fact, the principal planes are the coordinate planes of the unprimed coordinate system.

Figure 2 shows the three dimensional mapping of the slownesses (the inverse of the wave speeds) for the quasi-transverse ($q.T.$) mode of propagation in the hexagonal symmetry. In general, there are two other bulk waves that should be considered. These are omitted here in order to simplify the drawing. This mapping is a surface of revolution that intersects the (1,2) plane in a circle. The 3-axis is the true orientation of the fibers of the composite. However these fibers are believed to be oriented along the axis $3'$ in the coordinate system of the experiment.

When the elastic waves are propagated in the plane (1,3), the two dimensional slice (TE) is experimentally generated. Due to the invariance of the slownesses to a rotation around axis 3, other slices such as (B_1E) and (B_2E) are identical to

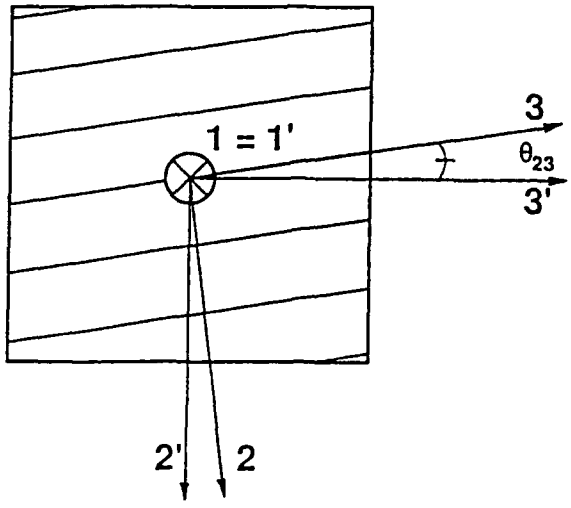

Figure 1: Definition of the angular parallax θ_{23}

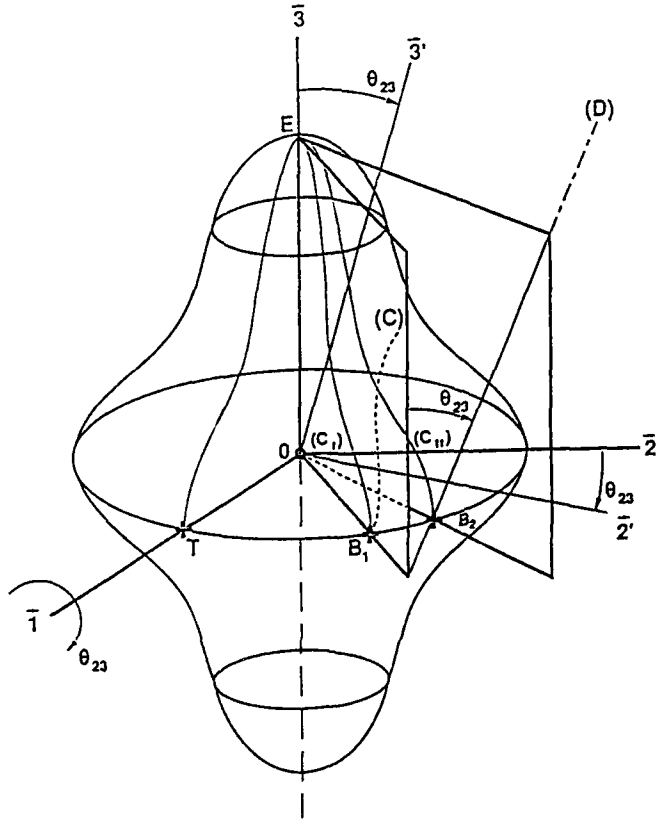

Figure 2: Three-dimensional mapping of the slowness for the quasi-transverse mode in the hexagonal symmetry.

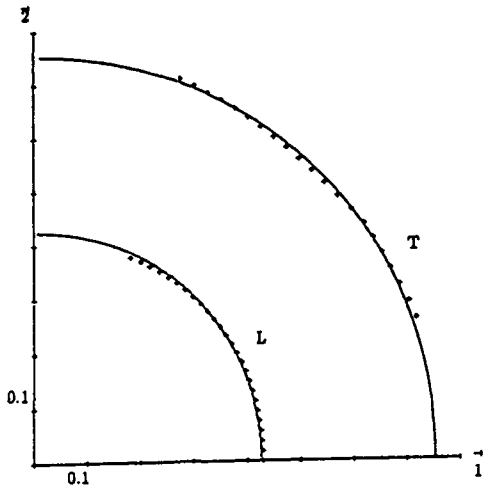

Figure 3: Normalized slowness for a unidirectional glass/epoxy composite material in the istropic plane (1,2). Crosses: Experimental slownesses; Continuous lines: Recovered slowness without angular parallax.

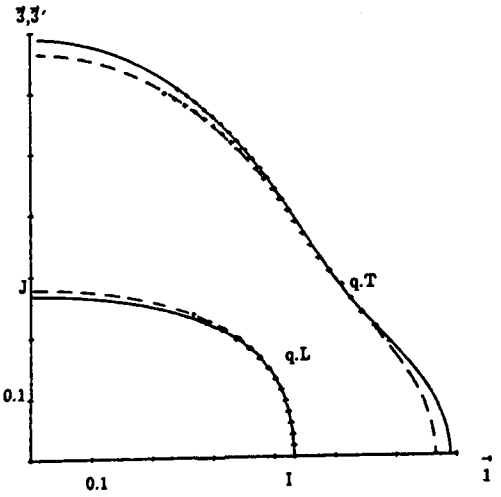

Figure 4: Noramalized slowness for a unidirectional glass/epoxy composite material in the anisotropic plane. Crosses: Experimental slowness; Continuous lines: Recovered slowness without angular parrallax-plane (1,3); Dashed lines: Recovered slowness with 8 degrees parallax-plane$(1, 3')$.

segment (ET). By introducing the Euler angle θ_{23}, we determine what the situation

is when the propagation takes place in $(1, 3')$ plane. In this case, we have to examine the projection of the straight line (D) onto the surface of revolution, *i.e.* the curve (C). This new slowness curve crosses (C_I) and (C_{II}), indicating that it is different from the corresponding curve in the principal plane (1,3).

Figure 3 and 4 show results for a unidirectional fiberglass/epoxy composite. In Figure 3 there is isotropy in the plane (1,2) that is orthogonal to the fibers. In Figure 4 the slownesses in the (1,3) and $(1, 3')$ planes are given. The crosses represent experimental data obtained by using an advanced ultrasonic spectro-interferometer (**19**). The lines are the recovered slownesses generated after optimally solving equation (6). The solid lines correspond to $\theta_{23} = 0^o$ (no angular parallax) and the dashed lines are for the case $\theta_{23} = 8^o$ (the sample is simply rotated on its stage by 8^o around the 1-axis). The shape of the recovered slownesses with and without parallax is similar. It is interesting to note that there is no change in the quasi-longitudinal $(q.L.)$ wavespeed along the 1-axis (the point labelled I in Figure 4) due to the fact that $1 \equiv 1'$. For the same mode, the wavespeed along the 3-axis (the point labelled J) is smaller when $\theta_{23} = 8^o$ compared to the case with no parallax. Again, this is not surprising as the largest wavespeed of this mode is along the fibers. After rotating the sample by θ_{23}, J no longer corresponds to the orientation of the fibers.

Using a double-iterative algorithm derived from the set of equations (6) in the primed coordinate system (**21**), we were able to recover a value for the Euler angle of $8.368^o \pm 0.319^o$. The elastic constants may be recovered with even greater accuracy. The precision in the recovery was obtained using a numerical simulation in which the parameters were selected to closely match those of the experiment (**21**).

References

1. Satake, M., and Jenkins, J.T., eds., "Micromechanics of Granular Materials," Elsevier, Amsterdam, 1988.

2. Chen, Y.C., Ishibashi, I., and Jenkins, J.T., "Dynamic shear modulus and fabric: part I, depositional and induced anisotropy, *Géotechnique*, Vol. 38, 1988, pp. 25–32.

3. Ishibashi, I., Chen, Y.C., and Jenkins, J.T., "Dynamic Shear modulus and fabric: part II, stress reversal," *Géotechnique*, Vol. 38, 1988, pp. 33-37.

4. Auld, B.A. "Acoustic Fields and Waves in Solids", Vol. 1, John Wiley, New York,

1973

5. Hoger, A., "On the determination of the residual stress in an elastic body," *Journal of Elasticity*, Vol. 16, 1986, pp. 303–324.

6. Nye, J.F., "Physical Properties of Crystals", Clarendon Press, Oxford, 1985, pp. 276–301.

7. Morse, P.H. and Feshbach, H., "Methods of Theoretical Physics", Vol. 1, McGraw Hill, New York, 1953, p. 28.

8. Miller, G.F. and Musgrave, M.J.P., "On the propagation of elastic waves in aelotropic media", *Proceedings of the Royal Society*, London, Vol. A 236, 1956, pp. 352–383.

9. Orth, W., "Analytische *Näherung für* elastiche Wellen in anisotropen kubischen Kristallen", *Physics of Condensed Matter*, Vol. 17, 1974, pp. 293–305.

10. Waterman, P.C., "Orientation Dependence of Elastic Waves in Single Crystals", *Physical Review*, Vol. 113, 1959, pp. 1240–1253.

11. Neighbours, J.R. and Smith, C.S., "An Approximation Method for the Determination of the Elastic Constants of Cubic Single Crystals", *Journal of Applied Physics*, Vol. 21, 1950, pp. 1338–1339.

12. Neighbours, J.R., "An Approximation Method for the Determination of the Elastic Constants of Single Crystals", *Journal of Applied Physics*, Vol. 26, 1954, pp. 865–869.

13. Featherston, F.H. and Neighbours, J.R., "Elastic Constants of Tantalum, Tungsten, and Molybdenum", *Physical Review*, Vol. 130, 1963, pp. 1324–1333.

14. Neighbours, J.R. and Schacher, G.E., "Determination of Elastic Constants from Sound-Velocity Measurements in Crystals of General Symmetry", *Journal of Applied Physics*, Vol. 38, 1967, pp. 5366–5375.

15. Neighbours, J.R., "Convergence of the calculations of elastic constants from wave velocities in cubic crystals", *Journal of Applied Physics*, Vol. 51, 1980, pp. 5801–

5803.

16. Every, A.G., "General, closed-form expressions for acoustic waves in cubic crystals", *Physical Review Letters*, Vol. 42, 1979, pp. 1065–1068.

17. Every, A.G., "General closed-form expressions for acoustic waves in elastically anisotropic solids, *Physical Review B*, Vol. 22, 1980, pp. 1746–1760.

18. Hosten, B. and Castagnede, B., "Optimisation du calcul des constantes elastiques a partir des mesures de vitesses *d'une* onde ultrasonore.", *Comptes Rendus a l'Academie des Sciences* (Paris), Vol. II 296, 1983, pp. 297–300.

19. Roux, J., Hosten, B., Castagnede, B. and Deschamps, M., "Caracterisation mecanique des solides par spectro-interferometrie ultrasonore", *Revue de Physique Appliquee*, Vol. 20, 1985, pp. 351-358.

20. Castagnede, B. and Sachse, W. "Optimized determination of elastic constants of anisotropic solids from wavespeed measurements", in Review of *Quantitative Nondestructive Evaluation*, Vol. 8B, Plenum Publishing Corporation, New York 1989, pp. 1855-1862.

21. Castagnede, B., Jenkins, J.T., Sachse, W., and Baste, J.-S., "Optimal determination of the elastic constants of composite materials and recovery of the orientation of principal acoustical axes of symmetry from measurements of wavespeeds in arbitrary non-principal planes", *Journal of Applied Physics*, Vol. 67, 1990, pp. 2753–2761.

22. Marx, A., *Krüger*, J.K. and Unruth, H.-G., "Brillouin Spectroscopy of Monodomains of Thin Polycrystalline Layers of Molecular Crystals", *Applied Physics A*, Vol. 47, 1988, pp. 367–371.

23. Kulver, R., Brose, K.-H., and Eckhardt, C.J., "Calculation of the elastic constants of phenanthreme crystals", *Chemical Physics*, Vol. 115, 1987, pp. 239–242.

24. Dye, R.C. and Eckhardt, C.J., "A complete set of elastic constants of crystalline anthracene by Brillouin scattering", *Journal of Chemical Physics*, Vol. 90, 1989, pp. 2090–2096.

25. Ross, C.A. and Sierakowski, "Elastic waves in fiber-reinforced composites", *Shock and Vibration Digest*, Vol. 7, 1975, 96–107.

Chapter Five

Anisotropic Elasticity for Random Arrays of Identical Spheres

James T. Jenkins

Abstract

We derive a relation between the average stress and the average strain in a homogeneous deformation of a transversely isotropic but otherwise random array of identical spheres that interact through noncentral contact forces. We assume that the displacement of a contact relative to a center may be calculated from the average strain of the aggregate and the average rotation of the spheres relative to that of the sample. In a homogeneous deformation of an anisotropic aggregate, the average rotation of the spheres is determined from the requirement that the stress be symmetric. In general, it differs from the average rotation of the sample. Then, having raised the issue of the different rotations, we focus on strongly inhomogeneous deformations, derive general expressions for the stress and couple stress, and, as an illustration, calculate the constitutive relations for small strains and rotations of an isotropic array with elastic contacts.

1 Introduction

We are interested first in the average small strain response of random granular assemblies that, by virtue of the process by which they are formed, possess an inherent anisotropy [1]. This interest originated in attempts to explain the volume changes observed in triaxial extension and triaxial compression of a granular material at a fixed pressure. These experiments were carried out on hollow cylindrical samples of essentially identical glass spheres confined within a membrane in a true

triaxial/torsion device [2]. As Jenkins [3] shows, the observed volume changes can be explained in the context of the anisotropic elasticity theory developed here for homogeneous deformations. However, as described in Chapter 1, more recent efforts to simulate these volume changes numerically have indicated that boundaries probably played the dominant role in the experiments. In any case, the theory for homogeneous deformations of an anisotropic aggregate has one important feature with several interesting consequences. Because the contact forces are noncentral, symmetry of the stress requires that the average rotation of the particles be different from the average rotation of the sample. We illustrate this in the context of a theory derived for arrays in which the geometric arrangement exhibits transverse anisotropy and the strains are so small that the behavior is elastic.

The interest in strongly inhomogeneous deformations arises from recent attempts to explain the structure of narrow regions of rather extreme inhomogeneity, called shear bands, in granular materials. An example of this activity is the work of Mühlhaus and Vardoulakis [4]. Such attempts involve the introduction of the additional degrees of freedom associated with the independence of the mean rotation of the particles. In existing treatments, energy arguments are used to obtain the constitutive relations that link the stress and couple stress to the strain and rotations. Here, we illustrate how such relations may be obtained from considerations of force and moment alone and provide a simple example that is appropriate for the small strain elastic response of an isotropic assembly. In these developments, the anisotropy of the aggregate is not crucial, although in granular materials it is likely that some form of anisotropy is always present.

For simplicity, we focus our attention on an idealized material consisting of identical spherical grains. We suppose that the particles are in contact and that the location of their centers is random. In reality, arrays of identical spheres often organize themselves into domains in which their centers are arranged periodically, but we ignore this or imagine that there is sufficient dispersion in the diameters to prevent the formation of such crystalline regions.

2 Homogeneous Deformations

We suppose that the diameter of a sphere is and that there are n of them per unit volume. We take $\boldsymbol{\alpha}$ to be the unit vector from the center of a sphere to a contact on its surface and introduce the orientational distribution of contacts $A(\boldsymbol{\alpha})$ so that $A(\boldsymbol{\alpha})d\boldsymbol{\alpha}$ is the probable number of contacts in the element $d\boldsymbol{\alpha}$ of solid angle centered at $\boldsymbol{\alpha}$. In homogeneous situations, this distribution function is independent of position and, because a contact is common to two spheres, $A(-\boldsymbol{\alpha}) = A(\boldsymbol{\alpha})$.

When the distribution of contacts is isotropic, $A(\boldsymbol{\alpha}) = k/4\pi$, where k, called the coordination number, is the average number of contacts per particle. When the contact distribution is not isotropic, but there are orthogonal planes of symmetry or an axis of symmetry, the distribution of contacts can be expressed in terms of a symmetric, traceless tensor A [5, 6] :

$$A(\boldsymbol{\alpha}) = \frac{k}{4\pi}(1 + A_{ij}\alpha_i\alpha_j). \tag{1}$$

For transversely isotropic materials, $\boldsymbol{A}$ may be expressed in terms of the unit vector $\boldsymbol{h}$ in the direction of the axis of anisotropy and the strength ε (1) of the anisotropy:

$$A_{ij} = -\varepsilon(\delta_{ij} - 3h_ih_j), \tag{2}$$

where $-\frac{1}{2} \leq \varepsilon \leq 1$. Then

$$A(\alpha) = \frac{k}{4\pi}\left[(1-\varepsilon) + 3\varepsilon(h_i\alpha_i)^2\right]. \tag{3}$$

The force $\boldsymbol{F}(\boldsymbol{\alpha})$ exerted by the sphere at a contact with orientation (3) has components parallel and perpendicular to $\boldsymbol{\alpha}$:

$$F_i = P\alpha_i - T_i, \tag{4}$$

where $T\cdot\boldsymbol{\alpha} = 0$. In a homogeneous deformation, we assume that $\boldsymbol{F}$is independent of position. Because the force exerted by the sphere at a contact is equal and opposite to the force exerted on the sphere, $\boldsymbol{F}(-\boldsymbol{\alpha}) = -\boldsymbol{F}(\boldsymbol{\alpha})$. The normal and tangential components depend upon the displacement of a contact relative to the center and are, in general, functions of (4). Following Hertz [7], the normal component P is related to the magnitude (4) of the normal component of the displacement s:

$$P = M(6\delta/\sigma)^{3/2}, \tag{5}$$

where M is given in terms of the shear modulus μ and Poissons ratio ν of the material of the spheres by

$$M = \frac{2}{9\sqrt{3}}\frac{\mu\sigma^2}{(1-\nu)}. \tag{6}$$

Here, for the tangential component of the contact force, we are content with the relationship between the initial increment of its magnitude T and that of the tangential displacement s:

$$T = Ks. \tag{7}$$

The modulus K has been determined by Mindlin [8] for the initial shearing at a contact subsequent to the application of the normal force :

$$K = \frac{2^{5/3}\mu^{2/3}}{(2-\nu)}[3(1-\nu)\sigma P]^{1/3}. \tag{8}$$

The assumptions are that there is Coulomb friction at contacts and that either the relative tangential displacement of the centers of contacting spheres is very small or the coefficient of friction is very large. In either case, there is no slip at contacts and the tangential deformation is recoverable. Following Cauchy, as outlined by Love [7] in his Note B, an expression for the average stress tensor $\boldsymbol{t}$ associated with a homogeneous deformation of the aggregate may be obtained by considering the force transmitted over an arbitrary element of area by pairs of contacting spheres whose line of centers is cut by the element. For random assemblies, the stress is naturally expressed in terms of the orientational distribution function and the contact force :

$$t_{ij} = -\frac{\sigma n}{2}\iint_{\boldsymbol{\alpha}} A(\boldsymbol{\alpha})F_i(\boldsymbol{\alpha})\alpha_j d\boldsymbol{\alpha}\,, \tag{9}$$

where the integration is over all solid angle. When using the theory to interpret the results of numerical simulations and physical experiments, this and other orientational averages are identified with volume averages over sufficiently large regions of nearly homogeneous strain and uniform rotations.

We relate the displacement $\boldsymbol{u}$ of a contact relative to the center of a sphere to the average strain of the aggregate $\boldsymbol{e}$ and to the difference between the average rotation of the aggregate $\boldsymbol{w}$ and the average rotation of the spheres $\boldsymbol{\omega}$:

$$u_i = \frac{\sigma}{2}(e_{ij} + w_{ij} - \omega_{ij})\alpha_j. \tag{10}$$

As usual, the strain tensor is symmetric and the rotation tensors are antisymmetric. As we shall see, it is important to make the distinction between the two average rotations when considering the static theory for anisotropic aggregates. In general, they will not be equal. Schwartz, Johnson, and Feng [9] and Walton [10] made this distinction when treating the dynamics of isotropic assemblies, but found that in the limit of long wavelengths, the rotations are identical. In formulating static theory for isotropic aggregates, Digby [11] and Walton [12] tacitly and correctly assumed that the rotations were the same.

Of course, even with the incorporation of the additional degrees of freedom associated with the average rotations of the particles, the kinematic assumption (10) may be far from correct. For example, when used with the contact force laws (5) and (7), it requires that contacts with the same orientation transmit the

same force. Also, when the average strain is isotropic and compressive, it requires that the normal components of all contact forces must be equal and all tangential components must vanish. Numerical simulations described by Cundall, Jenkins, & Ishibashi [13] indicate that in isotropic aggregates there are rather large variations in the forces at contacts with the same orientation, even when the mean strain is isotropic. Also, the speed of the shear wave through a compressed isotropic aggregate predicted by Digby [11] and Walton [12] is about three times greater than that measured in numerical simulations and experiments [14]. However in order to make a quantitative evaluation of similar shortcomings of the kinematic assumption (10) in anisotropic aggregates, we must first obtain the predictions of the theory that is based upon it.

We consider a transversely isotropic aggregate that has, through the application of the appropriate combination of isotropic and deviatoric stress, been isotropically compressed to an initial average volume strain of magnitude Δ. In this initial compression, both measures of the average rotation are assumed to be zero. Then, we imagine that small increments of homogeneous strain and uniform rotation are superposed on this. In this event, when the kinematic assumption is used to calculate the normal and tangential components of the contact force, we obtain

$$P = M\Delta^{1/2}(\Delta\delta_{ij} - \frac{9}{2}e_{ij})\alpha_i\alpha_j, \tag{11}$$

and

$$T_i = 9M\frac{(1-\nu)}{(2-\nu)}\Delta^{1/2}(\delta_{ij} - \alpha_i\alpha_j)(e_{jk} + w_{jk} - \omega_{jk})\alpha_k. \tag{12}$$

These, then, are used with the orientational distribution function (3) in the expression (9) for the stress and the integrals over solid angle carried out.

Integrals that facilitate this calculation are

$$I_{ijkl} \equiv \iint_{\boldsymbol{\alpha}} \alpha_i\alpha_j\alpha_k\alpha_l d\boldsymbol{\alpha} = \frac{4\pi}{15}(\delta_{ij}\delta_{kl} + \delta_{ik}\delta_{jl} + \delta_{il}\delta_{jk}) \tag{13}$$

and the more elaborate

$$\iint_{\boldsymbol{\alpha}} \alpha_i\alpha_j\alpha_k\alpha_l\alpha_p\alpha_q d\boldsymbol{\alpha} = \frac{1}{7}(\delta_{iq}I_{jklp} + \delta_{jq}I_{klpi} + \delta_{kq}I_{lpij} + \delta_{lq}I_{pijk} + \delta_{pq}I_{ijkl}). \tag{14}$$

The result of the integration for the stress is

$$\begin{aligned} t_{ij} = \frac{1}{2}n\sigma\frac{k}{4\pi}M\Delta^{1/2}\Big\{ & -\frac{4\pi}{15}[(5-2\varepsilon)\delta_{ij} + 6\varepsilon h_ih_j]\Delta \\ & + \frac{12\pi}{5}\frac{(1-\nu)}{(2-\nu)}[(5-2\varepsilon)(e_{ij} + w_{ij} - \omega_{ij}) + 6\varepsilon h_j(e_{ik} + w_{ik} - \omega_{ik})h_k] \\ & + \frac{6\pi}{35}\frac{\nu}{(2-\nu)}[(7-4\varepsilon)(e_{kk}\delta_{ij} + 2e_{ij}) + 6\varepsilon h_kh_le_{kl}\delta_{ij} + 3\varepsilon e_{kk}h_ih_j \\ & + 12\varepsilon(h_ie_{jk}h_k + h_je_{ik}h_k]\Big\}. \end{aligned} \tag{15}$$

The terms in the first line of equation (15) are those associated with the initial isotropic volume strain. Those in the second line result from the additional increments of strain and rotation and the resistance to these provided by the component of the contact force that is tangent to the surface of the sphere. The terms in the third and fourth lines are incremental contributions associated with both components of the contact force. If the contact force had only a normal component with magnitude given by (11), then the stress would be given by (15) with the first line unchanged, the second deleted, and the factor $\nu/(2-\nu)$ multiplying the third and fourth lines replaced by unity.

When body couples are absent and the deformation is homogeneous, the stress must be symmetric. If the average rotations had been assumed to be the same from the outset, symmetry of the stress could be achieved by discarding the antisymmetric part of the last term in the second line of (15). The resulting expression would be symmetric, but incomplete. The correct method of obtaining a symmetric stress is to make the distinction between the rotations and to determine the average rotations of the particles so that the symmetry of the stress is insured. For example, symmetry of the stress given by (15) requires that

$$\begin{aligned} 2(5-2\varepsilon)(w_{ij}-\omega_{ij}) + 6\varepsilon[(w_{ik}-\omega_{ik})h_j - (w_{jk}-\omega_{jk})h_i]h_k \\ + 6\varepsilon(e_{ik}h_j - e_{jk}h_i)h_k = 0. \end{aligned} \tag{16}$$

Solving this for ω yields

$$\omega_{ij} = w_{ij} + \frac{3\varepsilon}{(5+\varepsilon)}(e_{ik}h_j - e_{jk}h_i)h_k. \tag{17}$$

Thus, given the strength and axis of the anisotropy and the average strain and rotation of the aggregate, equation (17) determines the average rotation of the particles.

Upon employing (17) in (15), we obtain an explicit form for the symmetric stress given in terms of the average strain of the aggregate alone:

$$\begin{aligned} t_{ij} = \frac{1}{2}n\sigma\frac{k}{4\pi}M\Delta^{1/2}\Big\{ & -\frac{4\pi}{15}[(5-2\varepsilon)\delta_{ij} + 6\varepsilon h_i h_j]\Delta \\ & + \frac{12\pi}{5}\frac{(1-\nu)}{(2-\nu)}[(5-2\varepsilon)e_{ij} + 3\varepsilon\frac{(4-2\varepsilon)}{(5+\varepsilon)}(h_j e_{il} + h_i e_{jk})h_k \\ & + 18\varepsilon\frac{\varepsilon}{(5+\varepsilon)}h_k h_l e_{kl} h_i h_j \\ & + \frac{6\pi}{35}\frac{\nu}{(2-\nu)}[(7-4\varepsilon)e_{kk}\delta_{ij} + 2e_{ij}) + 6\varepsilon h_k h_l e_{kl}\delta_{ij} + 3\varepsilon e_{kk}h_i h_j \\ & + 12\varepsilon(h_i e_{jk}h_k + h_j e_{ik}h_k]\Big\}. \end{aligned} \tag{18}$$

This is the form of the stress for a homogeneous deformation of a transversely isotropic but otherwise random array that has been first isotropically compressed and then subjected to a small strain. Of course it is correct only in so far as the characterization (3) of the anisotropy, the contact force laws (5) and (7), and the kinematic assumption (10) are correct.

2 Inhomogeneous Deformations

When the deformation of the aggregate is strongly inhomogeneous, the calculation of the stress is slightly more complicated and a corresponding determination of the couple stress is possible. We consider an infinitesimal plane element of area with unit normal $\boldsymbol{n}$ and a typical pair of contacting particles with their centers on different sides of the plane. The vector $\boldsymbol{s} \equiv \sigma\boldsymbol{\alpha}$ is directed from the center of the particle in the region pierced by $-\boldsymbol{n}$ to the center in the region pierced by $\boldsymbol{n}$. The line joining the centers intersects the plane at the point $\boldsymbol{r}$; and the contact is located at $\boldsymbol{r}_c = \boldsymbol{r} - \xi\boldsymbol{s}$, where $-1/2 \leq \xi \leq 1/2$. The location of the area element is assumed to be fixed by $\boldsymbol{r}$ and variations in the position of the point of intersection over the element are ignored. The number density n, the orientational distribution A, and the contact force $\boldsymbol{F}$ are all taken to be functions of $\boldsymbol{r}_c$ and $\boldsymbol{\alpha}$. Then

$$A(\boldsymbol{r}_c, -\boldsymbol{\alpha}) = A(\boldsymbol{r}, \boldsymbol{\alpha}) \text{ and } \boldsymbol{F}(\boldsymbol{r}_c, -\boldsymbol{\alpha}) = -\boldsymbol{F}(\boldsymbol{r}_c, \boldsymbol{\alpha}) \tag{19}$$

Again the determination of the stress parallels that of Cauchy as outlined by Love [7]. However, because of the strong inhomogeneity, the calculation of the force transmitted across the plane by all pairs of particles with orientation $\boldsymbol{\alpha}$ whose line of centers is cut by the plane involves an integration over ξ. The result is most conveniently expressed in terms of

$$f_i(\boldsymbol{r} - \xi\boldsymbol{s}, \boldsymbol{\alpha}) \equiv n(\boldsymbol{r}_c)A(\boldsymbol{r}_c, \boldsymbol{\alpha})F_i(\boldsymbol{r}_c, \boldsymbol{\alpha}). \tag{20}$$

Then, at $\boldsymbol{r}$, the components of the traction $\boldsymbol{\tau}$ are given in terms of the components of $\boldsymbol{n}$ by

$$\tau_i = t_{ij}n_j, \tag{21}$$

where

$$t_{ij}(\boldsymbol{r}) = -\frac{\sigma}{2}\iint_{\boldsymbol{\alpha}}\int_{-1/2}^{1/2} f_i(\boldsymbol{r} - \xi\boldsymbol{s}, \boldsymbol{\alpha})\alpha_j d\xi d\boldsymbol{\alpha} \tag{22}$$

with the double integral again taken over all solid angle.

The corresponding expression for the couple stress $\boldsymbol{c}$ is obtained by considering the moment of the contact force about $\boldsymbol{r}$:

$$c_{il}(\boldsymbol{r}) = \frac{\sigma}{2}\varepsilon_{ijk} \iint_{\boldsymbol{\alpha}} \int_{-1/2}^{1/2} \xi s_j f_k(\boldsymbol{r} - \xi \boldsymbol{s}, \boldsymbol{\alpha}) \alpha_1 d\xi d\boldsymbol{\alpha} \tag{23}$$

Then the components of the couple per unit area $\boldsymbol{\chi}$ at $\boldsymbol{r}$ are given in terms of those of $\boldsymbol{c}$ and $\boldsymbol{n}$ by

$$\chi_i = c_{il} n_l. \tag{24}$$

The stress and the couple stress are related by the balance of moment. In the absence of body couples, this is

$$\frac{\partial c_{il}}{\partial r_l} + \varepsilon_{ijk} t_{kj} = 0. \tag{25}$$

If the contact forces are assumed to be related to average strains and rotations, then simpler, approximate forms for the stress and the couple stress may be obtained. These are based on the Taylor series expansion of the contact force about $\boldsymbol{r}$:

$$\boldsymbol{f}(\boldsymbol{r} - \xi \boldsymbol{s}) \doteq \boldsymbol{f}(\boldsymbol{r}) - \xi \boldsymbol{s} \cdot \nabla \boldsymbol{f}(\boldsymbol{r}) + \frac{1}{2}\xi^2 (\boldsymbol{s} \cdot \nabla)^2 \boldsymbol{f}(\boldsymbol{r}). \tag{26}$$

When the series is used in (22) and (23) and the integrations over ξ are carried out, we obtain

$$t_{ij}(\boldsymbol{r}) = -\frac{1}{2}\sigma \iint_{\boldsymbol{\alpha}} f_i(\boldsymbol{r}, \boldsymbol{\alpha}) \alpha_j d\boldsymbol{\alpha} - \frac{1}{24}\sigma^3 \frac{\partial^2}{\partial r_k \partial r_l} \iint_{\boldsymbol{\alpha}} f_i(\boldsymbol{r}, \boldsymbol{\alpha}) \alpha_j \alpha_k \alpha_l d\boldsymbol{\alpha} \tag{27}$$

and

$$c_{il}(\boldsymbol{r}) = -\frac{1}{12}\sigma^3 \varepsilon_{ijk} \frac{\partial}{\partial r_m} \iint_{\boldsymbol{\alpha}} f_k(\boldsymbol{r}, \boldsymbol{\alpha}) \alpha_j \alpha_l \alpha_m d\boldsymbol{\alpha}\,, \tag{28}$$

up to an error of order $(\sigma, L)^4$, where L is the length scale over which the average fields vary.

It should be clear from (27) and (28) that the couple stress and the antisymmetric part of the stress depend only upon the tangential component of the contact force. Also, because the expansions for the stress and couple stress have been carried to the same order, there is an additional contribution to the stress that involves the second spatial derivatives. It may be that this term is small in comparison to the classical part of the stress, however the contribution of its antisymmetric part to the balance of moment (25) is exactly the same order as the divergence of the couple stress given by (28). In any case, it is the diameter of the particle that

provides the length scale in terms of which the importance of the new terms may be evaluated.

To illustrate the calculation of the couple stress and new parts of the stress, we suppose that the aggregate is isotropic and the behavior of a contact is governed by (4) through (8). Then, with the help of (13) and (14),

$$\iint_{\boldsymbol{\alpha}} f_i(\boldsymbol{r},\boldsymbol{\alpha})\alpha_j\alpha_k\alpha_l d\boldsymbol{\alpha} = \frac{3}{35}nkM\Delta^{1/2}\left[\frac{7}{9}\Delta(\delta_{ij}\delta_{kl}+\delta_{ik}\delta_{jl}+\delta_{il}\delta_{jk})\right.$$

$$-\frac{(7-6\nu)}{(2-\nu)}(e_{ij}\delta_{kl}+e_{ik}\delta_{jl}+e_{il}\delta_{jk})-\frac{\nu}{(2-\nu)}(e_{jk}\delta_{il}+e_{jl}\delta_{ik}+e_{kl}\delta_{ij})$$

$$\left.-7\frac{(1-\nu)}{(2-\nu)}(\Omega_{ij}\delta_{kl}+\Omega_{ik}\delta_{jl}+\Omega_{il}\delta_{jk})\right], \tag{29}$$

where $\boldsymbol{\Omega} \equiv \boldsymbol{w}-\boldsymbol{\omega}$. Using this, for example, in (28) an explicit form of the couple stress may be obtained :

$$c_{pk} = \frac{1}{20}nk\sigma^3M\Delta^{1/2}\frac{(1-\nu)}{(2-\nu)}\frac{\partial}{\partial r_l}[\varepsilon_{pjil}\Omega_{ij}\delta_{kl}$$

$$+\varepsilon_{pli}(e_{ik}+\Omega_{ik})+\varepsilon_{pki}(e_{il}+\Omega_{il})]. \tag{30}$$

We note that, as a consequence of the assumptions made concerning the contact forces and the kinematics, the gradient of the difference between the two rotations appears in the couple stress, often accompanied by spatial derivatives of the strain. This is in contrast to the classical Cosserat theory for isotropic materials as outlined, for example, by Toupin [15], in which the gradients of the average particle rotations alone appear. Also, in this classical couple stress theory, the antisymmetric part of the stress is associated with the difference in the average rotations alone, not with the spatial gradients of the difference or those of the strain. However, the structure of the theory that results from the approach outlined above does depend rather strongly on the nature of the contact. For example, if slip rather than deformation were to predominate at contacts, then particle rotations might be expected to be large relative to the classical strains and rotations. In this case, the resulting theory for the inelastic deformations of the aggregate is likely to bear a stronger resemblance to the Cosserat theory. In any event, given the relation of the contact forces to the average fields of interest and a characterization of the orientational distribution of contacts, the expressions (27) and (28) may be used to calculate the stress and couple stress. Of course, the relationship between the results of this calculation and what is measured in numerical simulations and physical experiments

will depend upon how closely the assumptions upon which the theory is based are realized.

References

1. Arthur, J. R. F., and Menzies, B. K. 1972. Inherent anisotropy in a sand. *Géotechnique*, Vol. 22, No. 1, pp. 115–128.

2. Chen, Y. C., Ishibashi, I., and Jenkins, J. T. 1988. Dynamic shear modulus and fabric: part I, depositional and induced fabric. *Géotechnique*, Vol. 38, No. 1, pp. 25–32.

3. Jenkins, J. T. 1988. Volume change in small strain axisymmetric deformations of a granular material. In *Micromechanics of Granular Materials* (Satake, M. and Jenkins, J. T., Eds.) pp. 245–252, Elsevier: Amsterdam.

4. Mühlhaus, H.-B. and Vardoulakis, I. 1987. The thickness of shear bands in granular materials. *Géotechnique*, Vol. 37, No. 3, pp. 271–283.

5. Kanatani, K. 1984. Distribution of directional data and fabric tensors. *International Journal of Engineering Science*, Vol. 22, pp. 149–164.

6. Cowin, S.C. 1985. The relationship between the elasticity tensor and the fabric tensor. *Mechanics of Materials*, Vol. 4, pp. 137–147.

7. Love, A. E. H. 1927. *A Treatise on the Mathematical Theory of Elasticity.* Cambridge University Press: Cambridge.

8. Mindlin, R. D. 1949. Compliance of elastic bodies in contact. Journal of Applied Mechanics, Vol. 16, pp. 259–268.

9. Schwartz, L. M., Johnson, D. L., and Feng, S. 1984. Vibrational modes in granular materials. *Physical Review Letters*, Vol. 52, pp. 831–834.

10. Walton, K. 1988. Wave propagation within random packings of spheres. *Geophysical Journal*, Vol. 92, pp. 89–97.

11. Digby, P. J. 1981. The effective elastic moduli of porous granular rocks. *Journal of Applied Mechanics*, Vol. 16, pp. 803–808.

12. Walton, K. 1987. The effective elastic modulus of a random packing of spheres. *Journal of the Mechanics and Physics of Solids*, Vol. 35, pp. 213–216.

13. Cundall, P. A., Jenkins, J T., and Ishibashi, I. 1988. Evolution of elastic moduli in a deforming granular assembly. In *Powders an Grains* (Bizrez, J. and Gourvès. R., Eds.) pp. 319–322, Balkema:Rotterman.

14. Jenkins, J. T., Cundall, P. A., and Ishibashi, I. 1988. Micromechanical modeling of granular materials with the assistance of experiments and numerical simulations. In *Powders and Grains* (Biarez, J. and Gourvs. R., Eds.) pp. 257–264, Balkema: Rotterdam.

15. Toupin, R. A. 1964. Theories of elasticity with couple stress. *Archive for Rational Mechanics and Analysis*, Vol. 11, pp. 385–414.

Chapter Six

Evolution of Elastic Moduli in a Deforming Granular Assembly

Peter A.Cundall

Abstract

Numerical experiments are performed by the distinct element method on a sample of 432 spheres in three dimensions. During axisymmetric loading and unloading of the sample, measurements are made of incremental elastic moduli. The initial elastic shear modulus compares well with shear-wave results from similar physical tests, but the reduction in modulus with shear straining is greater than that observed physically. The evolution of confined moduli (corresponding to p-waves) is a sensitive measure of strain-induced anisotropy.

1 Background

Chen et al. (1988) present the results of physical experiments on samples consisting of a mixture of two sizes of glass spheres. The experiments, which employed a torsional simple shear device, produced a number of interesting results that may be interpreted by means of similar numerical experiments. One set of numerical experiments was performed by Cundall (1988) with the objective of reproducing the stress/strain behavior in shear and the associated volumetric changes. These experiments, and a related theoretical study by Jenkins (1988), suggest that the physical samples contained considerable depositional anisotropy.

Similar numerical experiments are reported here, but the emphasis now is on the variation of elastic wave speeds as the sample is loaded and unloaded.

The results are compared to the physical measurements, and are related to changes in sample fabric.

2 Numerical Procedure

The distinct element method (Cundall & Strack 1979a) was used to perform the tests, using program TRUBAL (Cundall & Strack 1979b, Strack & Cundall 1984) to load a sample contained within a periodic volume (see Cundall 1988). A 432-sphere sample was prepared with the following characteristics for the intact material (glass spheres) and for the assembly. Note that the elastic and frictional properties of glass were confirmed by direct loading on individual glass beads (Ishibashi 1989).

Shear modulus of glass	$G = 2.9 \times 10^{10}$ Pa
Poisson's ratio of glass	$\nu = 0.2$
Friction coefficient	$\mu = 0.3$
Number of particles:	40 of 0.1825mm rad.
	392 of 0.1075mm rad.
Isotropic stress	$\sigma_o = 1.38 \times 10^5$ Pa
Initial porosity	$n_o = 0.368$
Initial coordination number	$K_o = 5.37$

Hertz theory applies in the normal contact direction. In the shear direction, the stiffness depends on normal force but not on shear displacement (see Cundall 1988). In order to achieve, simultaneously, a given isotropic stress and a given porosity, some adjustment of the friction coefficient is necessary during compaction. The following sequence of steps was used to create the initial isotropic sample.

1. Random placement of all particles within a cubic space of 19 mm^3; no particle touches any other.
2. Isotropic shrinking of the periodic volume to a porosity of $n = 0.367$, under a friction coefficient of $\mu = 0.01$.
3. Isotropic compaction or expansion of the periodic volume under $\mu = 0.05$, until a mean stress of $\sigma_o = 1.38 \times 10^5$ Pa is achieved.
4. Setting of friction coefficient μ to 0.15, and further isotropic volume adjustments as necessary to keep the mean stress at 1.38×10^5 Pa. The final porosity stabilized at $n = 0.368$. The friction coefficient was then set to 0.3.

For comparison, the physical tests (Chen et al. 1988) were done under conditions of $\sigma_o = 138$ KPa, $n = 0.367$.

Compression/extension shear tests are performed by applying strain rates to the periodic space as follows

$$\dot{e}_{11} = \frac{2\dot{\gamma}_m}{3} + \frac{\dot{e}_v}{3}$$

$$\dot{e}_{22} = -\frac{\dot{\gamma}_m}{3} + \frac{\dot{e}_v}{3} \qquad (1)$$

$$\dot{e}_{33} = -\frac{\dot{\gamma}_m}{3} + \frac{\dot{e}_v}{3},$$

where γ_m is the maximum shear strain plotted in the figures that follow. Constant isotropic stress is maintained with a numerical servo-control that adjusts $\dot{e}_v$.

3 Results

Figure 1 provides three orthogonal views of the sample after volumetric compaction: the intensity of shading is related to the mean stress carried by each particle. White (unshaded) particles carry no load - i.e. they are "floating." It is clear that there is a wide variation in the average load carried by the particles, even though the compaction was carried out at a very low friction coefficient.

A histogram of normal forces is presented in Figure 2 for the same starting state.

Figure 3 records the stress/strain response of the sample for axisymmetric loading and unloading according to equations (1).

Figure 4 shows the corresponding volumetric response, and Figure 5 the evolution of coordination number, K, with strain.

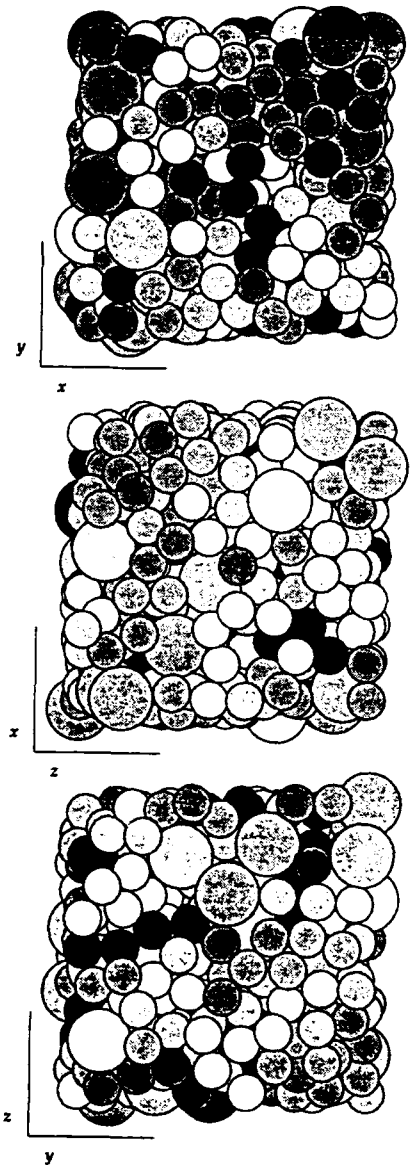

Figure 1: Three orthogonal views of the numerical assembly at its initial state; the intensity of shading is proportional to the mean stress carried by each sphere.

The maximum applied strain was about 0.45%, to correspond with the physical tests performed by Chen et al. (1988) and Ishibashi et al. (1988).

In the physical tests of Chen et al. (1988), long wavelength shear waves of low amplitude were propagated through the samples in order to assess the changing elastic shear modulus. For low amplitude oscillations, contact sliding does not occur—sliding stops at the instant of unloading; upon reloading, sliding only resumes again at the original point of loading.

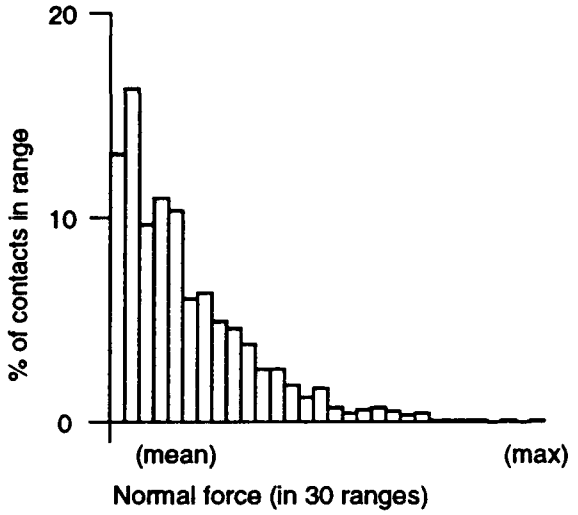

Figure 2: Histogram of contact normal forces at the initial state (A).

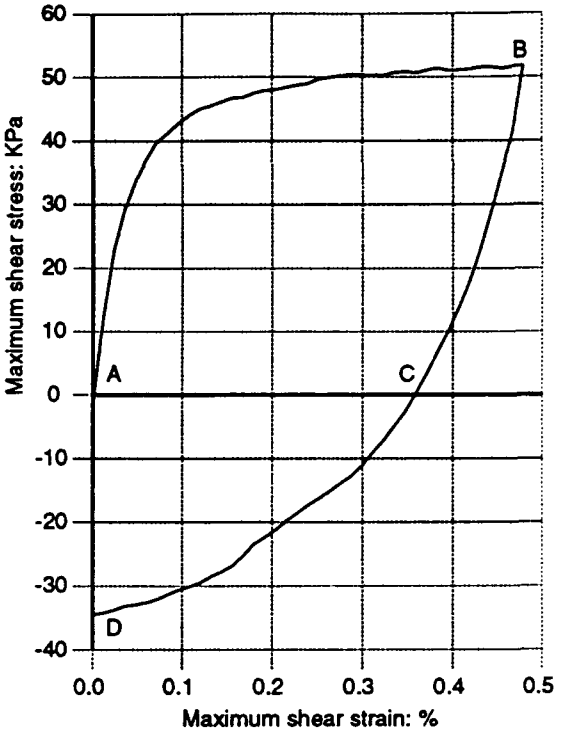

Figure 3: Histogram of contact normal forces at the initial state (A).

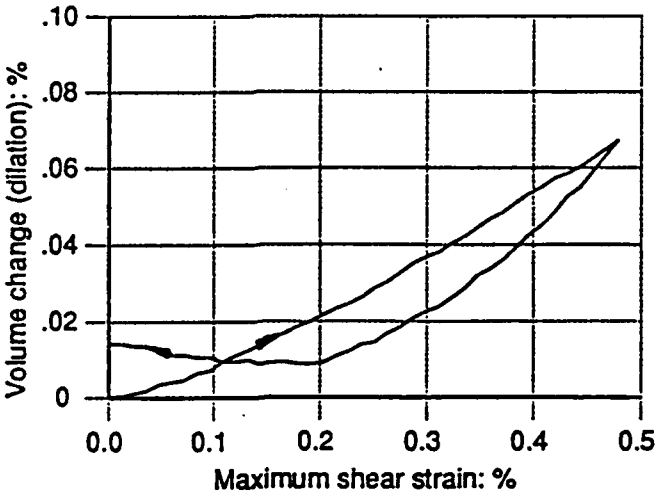

Figure 4: Volume changes corresponding to Figure 3.

Such "probes" are simulated numerically by making small strain increments, Δe_{12}, at infinite friction to prevent sliding. The probes were done at several points along the loading/unloading path, and corresponding shear modulus values plotted

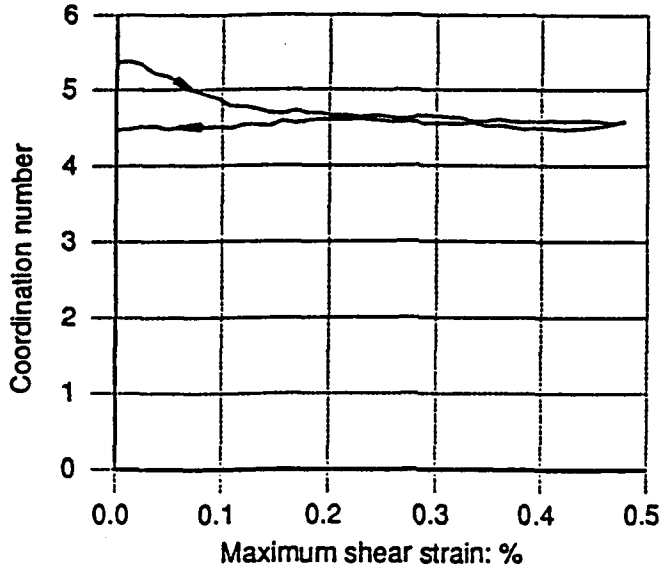

Figure 5: Evolution of coordination number during loading and unloading test of Figure 3.

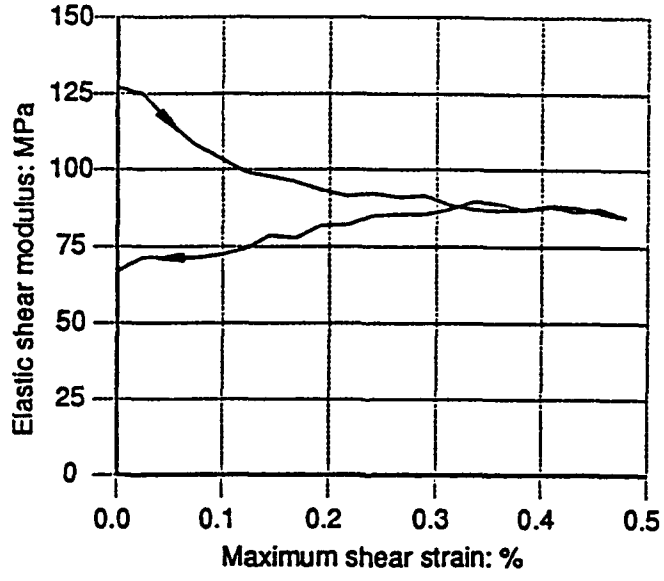

Figure 6: Evolution of elastic shear modulus (in $\dot{e}_{12}$ direction) during the test of Figure 3.

The initial modulus (at zero shear strain) is 127 MPa, which compares with 161 MPa derived from propagating shear waves in the physical tests (Chen et al.). The reduction in numerical shear modulus at 0.45% strain is 32%, while the physical tests give a reduction of around 20% for the same shear strain.

It is known that a granular material becomes elastically anisotropic when

loaded in shear. Partly, this is due to preferential contact loss in the minor principal strain direction: i.e. a geometric fabric develops. But when contacts obey the Hertzian law, they become stiffer in the major direction and softer in the minor direction: this dependence on the angular force distribution may be termed a *kinetic fabric*. Both geometric and kinetic effects occur in the numerical tests, but there does not appear to be an accepted way to measure the combined fabric. We can quantify the anisotropy by making small-strain probes that correspond to propagating compressional waves in three orthogonal directions; recall that $\dot{e}_{11}$ is in the major principal direction of the axisymmetric sample. Table 1 records the modulus values at various states of the loading/unloading test—refer to Figure 3. The probes are applied as strain increments in the given directions; all other strain components are zero.

State	(11)	(22)	(33)
A	341.1	357.6	356.9
B	366.0	204.5	173.1
C	310.4	279.7	248.7
D	157.5	289.8	307.1

Table 1: Confined modulus values in MPa for probes in three orthogonal directions.

Figures 7 and 8 record the distributions of contact normal forces at states B and C, respectively.

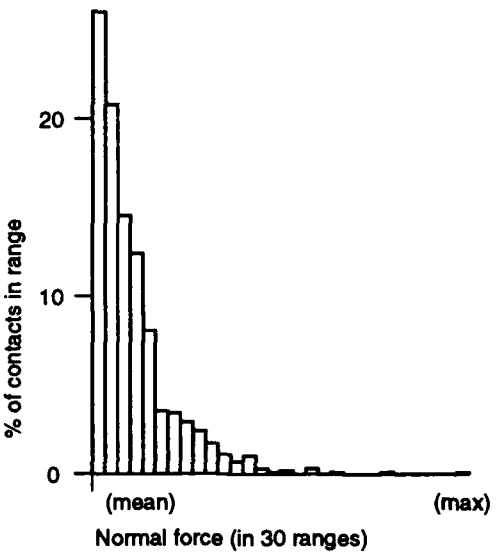

Figure 7: Histogram of contact normal forces at state B (maximum shear strain).

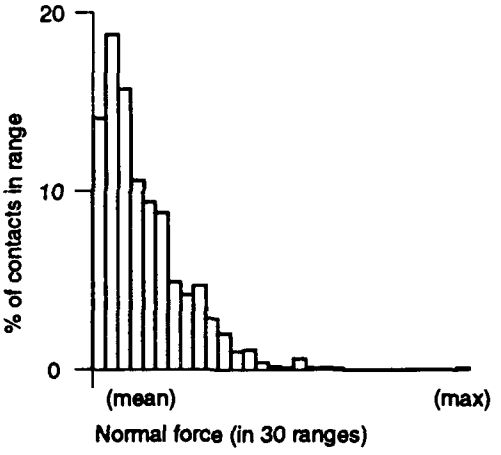

Figure 8: Histogram of contact normal forces at state C (zero shear stress, after unloading).

4 Conclusions

The agreement in initial elastic shear moduli between physical and numerical tests is considered to be quite good, bearing in mind that the numerical simulations were based on properties of intact glass, and incorporated no arbitrary factors. However, the numerical tests show a 50% greater reduction in modulus with straining than the physical tests. Table 1 suggests that p-wave measurements in tests on granular material may be used as a sensitive measure of anisotropy, and how it evolves with shear strain. The ratio between orthogonal modulus values is almost 2:1 at 0.45%

shear strain.

The histograms of normal force show that force distributions are heavily biased towards the low values; theories that assume symmetrical distributions about the mean may be seriously in error.

The simulations were all done on an 80386-based micro-computer, and each stage (e.g. compaction; loading) takes two to four hours to compute; each probe takes 25 minutes.

References

Chen, Y.-C, I.Ishibashi & J.T.Jenkins 1988. Dynamic shear modulus and fabric: part I, depositional and induced anisotropy. Géotechnique **38**:25-32.

Cundall, P.A. 1988. Computer simulations of dense sphere assemblies. In M.Satake & J.T.Jenkins (eds.) Micromechanics of granular materials, p.113-123. Amsterdam: Elsevier Science Publishers.

Cundall, P.A. & O.D.L.Strack 1979a. A discrete numerical model for granular assemblies. Géotechnique **29**:47-65.

Cundall, P.A. & O.D.L.Strack 1979b. The distinct element method as a tool for research in granular media, Part II. Report to NSF concerning Grant ENG76-20771, Dept of Civil & Mineral Engineering, University of Minnesota.

Ishibashi, I. 1989. Personal communication.

Ishibashi, I, Y.-C.Chen & J.T.Jenkins 1988. Dynamic shear modulus and fabric: part II, stress reversal. Géotechnique **38**:33-37.

Jenkins, J.T. 1988. Volume changes in small strain axisymmetric deformations of a granular material. In M.Satake & J.T.Jenkins (eds.) Micromechanics of granular materials, p.245-252. Amsterdam: Elsevier Science Publishers.

Strack, O.D.L. & P.A.Cundall 1984. Fundamental studies of fabric in granular material. Interim report to NSF concerning Grant CEE-8310729, Dept of Civil & Mineral Engineering, University of Minnesota.

Chapter Seven

Measurement of Local Strainrate in a TRUBAL Sample

Peter A. Cundall

Abstract

The numerical simulation TRUBAL is employed together with a least-squares procedure to determine the local strain tensor experienced by a particle. The average of the straing tensor determined from the local strain tensors is compared to the overall strain tensor the difference between the two is calculated.

1 Discussion

Most theoretical models of a granular material contain the assumption that a representative particle is embedded in a uniform strain field, in order to compute the relative displacements at particle contacts. It is instructive to use TRUBAL to measure the local strain tensor experienced by each particle, and develop statistics that express the spacial fluctuations in strainrate.

The measurement of local strain is not as simple as the measurement of local stress. To determine the average stress tensor of a particle we use an expression that contains the discrete forces acting at the particle's contacts; the forces elsewhere are zero. It is not correct to use the displacements in a similar way to find strains, because the displacements in the voids are not zero. The method adopted here is to find the strainrate tensor that minimizes the error between the predicted displacements and the measured displacements. A least-squares procedure is used

to derive the tensor, given a set of displacement vectors and corresponding position vectors. The general procedure is described first, and tested on manufactured data, consisting of displacements at random points derived from random components of a displacement gradient tensor. It should be noted that, in general, the displacement vector components do not sum to zero — i.e. there is a rigid-body movement. The least-squares procedure also determines this.

1 General Least-Squares Procedure

We wish to find the displacement gradient tensor, e_{ij}, and the rigid-body displacement, u_i°, that represent the best fit to a set of n measured displacement values, U_i^m, where $m = 1, n$. The displacement vector U_i^m is located at a coordinate of x_i^m. The *predicted* displacements, u_i^m at the n points are:

$$u_i^m = e_{ij} x_j^m + u_i^\circ \tag{3}$$

A measure of the error is the sum of the squares of the deviations between predicted and measured displacements:

$$z = \sum_{m=1}^{n} \sum_{i=1}^{3} \left(u_i^m - U_i^m \right)^2 \tag{4}$$

The condition for minimum z is that

$$\frac{\partial z}{\partial e_{ij}} = 0 \qquad \text{and} \qquad \frac{\partial z}{\partial u_i^\circ} = 0 \tag{5}$$

Substituting (3) into (4) and differentiating, a set of twelve equations is obtained as follows, where $i = 1, 3$:

$$e_{i1} \sum_m x_1^m x_1^m + e_{i2} \sum_m x_2^m x_1^m + e_{i3} \sum_m x_3^m x_1^m + u_i^\circ \sum_m x_1^m = \sum_m U_i^m x_1^m \tag{6}$$

$$e_{i1} \sum_m x_1^m x_2^m + e_{i2} \sum_m x_2^m x_2^m + e_{i3} \sum_m x_3^m x_2^m + u_i^\circ \sum_m x_2^m = \sum_m U_i^m x_2^m \tag{7}$$

$$e_{i1} \sum_m x_1^m x_3^m + e_{i2} \sum_m x_2^m x_3^m + e_{i3} \sum_m x_3^m x_3^m + u_i^\circ \sum_m x_3^m = \sum_m U_i^m x_3^m \tag{8}$$

$$e_{i1} \sum_m x_1^m + e_{i2} \sum_m x_2^m + e_{i3} \sum_m x_3^m + u_i^\circ = \sum_m U_i^m \tag{9}$$

Since the coefficients of e_{ij} and u_i° on the left-hand sides are independent of i, we need only evaluate sixteen coefficients, and then apply a solution procedure three times, with different right-hand sides. The LU-decomposition routine LUDCMP given in Press, et al. (1986) is applied to the 4×4 coefficient matrix, and the accompanying back-substitution routine LUBKSB used three times; in this way, all twelve unknowns (nine strains and three displacements) are obtained.

The scheme is tested by starting with random strain and rigid-body components. These are used to generate displacement vectors at n random locations, using (3). The solution process described above then produces computed strain and rigid-body components: these are compared to the assumed starting values. It is found that the computed and assumed values are very close for $n \geq 4$. The program TEST, listed in Appendix, performs this comparison.

2 Least-Squares Procedure Applied to TRUBAL Data

m The above procedure is applied to sets of velocity vectors derived from a sphere assembly undergoing continuous straining. For each sphere (the "target" sphere) in the assembly, all contacting spheres are identified. Two separate ways of providing velocity data are used (yielding two distinct measures of local strainrate):

1. The translational velocities of contacting spheres relative to the target sphere are taken; there is no contribution from the spins of any particle. The coordinates inserted into equations 6 - 9 are the relative centroid coordinates.
2. At each contact on the target sphere, the relative velocity vector between two coincident points on the two spheres is used in the equations. This strain measure is affected by the spins of the target particle and all contacting particles. The coordinates of the contact points are used, rather than the centroids.

The procedure outlined above is implemented into subroutine JSTAT, and called from TRUBAL. It was checked with a number of two- and five-particle simulations, in which the spheres are given fixed velocities. Various combinations of rotations, spins and translations produced strainrates and rigid-body motions that were compared with predicted values. At this level, the procedure appeared to work as intended.

3 Preliminary Rresults From TRUBAL Simulations

Some preliminary tests have been done with the 54-sphere assembly used in

previous tests (Cundall, 1988). These tests use Hertzian contact laws. An unexpected result is that significant relative rigid-body motions are observed — i.e. the target particle appears to have a continuous translational velocity relative to its contacting neighbors. At first sight this does not seem to be reasonable. However the combination of anisotropic contact distribution and a nonlinear contact law means that overall tangent stiffnesses vary with angle around a sphere. If, say, one principal stress is increased, the relative contact displacements on opposite sides of a sphere must be different, if equilibrium is to be maintained. Hence the target sphere moves relative to its neighbors.

The following results are for four stages in an axisymmetric compression test, starting with the isotropic state produced by data file `SR1.DAT`. The sample is compressed in the σ_{11} direction, using a servo-control to keep the mean stress σ_o constant at 138 KPa. The shear stress ratio, τ/σ_o, is shown for each stage, where

$$\tau = \frac{1}{2}\left\{\sigma_{11} - \frac{\sigma_{22}+\sigma_{33}}{2}\right\}$$

The applied strainrate components (of the periodic space) are shown first, in the form

$$\begin{pmatrix} \dot{e}_{11} & \dot{e}_{12} & \dot{e}_{13} \\ \dot{e}_{21} & \dot{e}_{22} & \dot{e}_{23} \\ \dot{e}_{31} & \dot{e}_{32} & \dot{e}_{33} \end{pmatrix}$$

The strainrates represent averages of computed values for all particles that have four or more contacts: the actual number of particles is shown. The two measured strainrate tensors are then given, in the same form, followed by the relative rigid-body velocities for the two cases discussed previously. The velocities are given in the form: $(\dot{u}_1, \dot{u}_2, \dot{u}_3)$.

State at cycle 29050; $\tau\sigma_o = 0.31$.

```
Applied strainrates ...
     -1.304e-07           0           0
              0  7.956e-08           0
              0           0  7.956e-08      (45 particles considered)
        Strainrate measure 1 ...            Strainrate measure 2 ...
     -1.317E-07 -2.702E-09 -1.365E-08   -1.220E-07 -1.166E-08
-1.100E-07
      7.851E-09  7.306E-08 -1.185E-09    7.623E-09  6.717E-08
-2.181E-08
     -9.145E-09 -3.549E-09  7.914E-08    7.862E-08  7.423E-09
5.862E-08
```

```
Relative velocities ...
      1.606E-06  1.273E-06  1.306E-06    1.265E-06  9.717E-07
9.694E-07
```

State at cycle 30050; $\tau/\sigma_o = 0.42$.

```
Applied strainrates ...
     -1.296e-07          0          0
              0  8.042e-08          0
              0          0  8.042e-08      (47 particles considered)
        Strainrate measure 1 ...          Strainrate measure 2 ...
     -1.385E-07  4.289E-08 -7.000E-08   -1.153E-07  5.952E-09
-1.005E-07
      1.570E-08  8.747E-08  1.317E-08    1.233E-08  5.250E-08
-4.322E-08
      1.959E-08 -4.749E-08  1.065E-07    6.215E-08  3.052E-08
4.659E-08
Relative velocities ...
      1.898E-06  2.127E-06  1.998E-06    1.620E-06  1.124E-06
1.248E-06
```

State at cycle 31050; $\tau/\sigma_o = 0.47$.

```
Applied strainrates ...
     -1.263e-07          0          0
              0  8.370e-08          0
              0          0  8.370e-08      (45 particles considered)
        Strainrate measure 1 ...          Strainrate measure 2 ...
     -1.374E-07  1.033E-08 -3.049E-08   -1.072E-07  3.644E-09
-3.847E-08
     -1.388E-08  6.290E-08  1.228E-08   -1.917E-08  3.997E-08
1.332E-08
      3.278E-08  2.573E-08  8.349E-08    1.102E-07  6.303E-08
6.426E-08
Relative velocities ...
      2.246E-06  2.606E-06  2.842E-06    2.233E-06  1.502E-06
1.707E-06
```

State at cycle 32050; $\tau/\sigma_o = 0.49$.

```
Applied strainrates ...
     -1.259e-07          0          0
              0  8.408e-08          0
```

```
             0          0  8.408e-08      (44 particles considered)
       Strainrate measure 1 ...            Strainrate measure 2 ...
    -1.349E-07  2.004E-08 -3.243E-08   -2.061E-07  4.816E-08
-1.774E-09
    -3.121E-08  6.634E-08  1.840E-08   -2.584E-08  6.380E-08
-1.067E-08
     2.262E-08  5.704E-08  8.106E-08    7.896E-08  9.321E-08
1.072E-07
Relative velocities ...
     2.732E-06  3.337E-06  3.007E-06    2.984E-06  1.677E-06
2.401E-06
```

The main observation concerning the results is that the ensemble averages do not correspond very well with the applied strainrates; furthermore, there are large asymmetric components. It seems pointless to try to study *fluctuations* in strain (i.e. deviations from the average), when the *averages* are themselves exhibit such noisy behavior. The noise may come from an error in the procedure or coding, or it may be real. In either case, further work is needed to gain understanding.

REFERENCES

Cundall, P.A. *Computer simulations of dense sphere assemblies.* In M. Satake & J.T. Jenkins (Eds.) Micromechanics of granular materials: 113-123. Elsevier Science Publishers, 1988.

Press, H., B.P. Flannery, S.A. Teukolsky, W.T. Vetterling. *Numerical Recipes*, Cambridge University Press, 1986.

APPENDIX: listing of TEST program for strain calculation

```
      program test
c
c Test of least-squares recovery of strainrate tensors from
velocities
c
      logical flag
      parameter (ns=4,np=10)
      dimension a(ns,ns),b(ns),indx(ns),etarg(3,3),ecomp(3,3)
      dimension x(3,np),v(3,np),rbv(3)
   10 write (*,1001)
      read  (*,*)   num
      if (num .eq.  0) stop
c--- random rigid-body motions ---
      rbv(1) = (uran() - 0.5) * 1e-5
      rbv(2) = (uran() - 0.5) * 1e-5
      rbv(3) = (uran() - 0.5) * 1e-5
      write (*,1006)
c--- generate target strain tensor ---
      do 20 i = 1,3
        do 15 j = 1,3
          etarg(i,j) = 1e-6 * (uran() - 0.5)
   15   continue
        write (*,1002) (etarg(i,j),j=1,3),rbv(i)
   20 continue
      write (*,1004)
c--- generate measurement points ---
      do 40 n = 1,num
        do 25 i = 1,3
          x(i,n) = 10.0 * uran()
   25   continue
        do 35 i = 1,3
          v(i,n) = rbv(i)
          do 30 j = 1,3
            v(i,n) = v(i,n) + etarg(i,j) * x(j,n)
   30     continue
   35   continue
        write (*,1003) n,(x(i,n),i=1,3), (v(i,n),i=1,3)
```

```
   40 continue
      flag = .false.
c--- assemble A matrix ---
      do 60 j = 1,3
        do 50 i = 1,3
          a(i,j) = 0.0
          do 45 n = 1,num
            a(i,j) = a(i,j) + x(i,n) * x(j,n)
   45     continue
   50   continue
   60 continue
      do 68 k = 1,3
        a(4,k) = 0.0
        a(k,4) = 0.0
        do 65 n = 1,num
          a(4,k) = a(4,k) + x(k,n)
          a(k,4) = a(k,4) + x(k,n)
   65   continue
   68 continue
      a(4,4) = float(num)
c--- LU decomposition ---
      call ludcmp (a,ns,ns,indx,d,flag)
      if (flag) then
        write (*,1000)
        goto 500
      else
        write (*,1007)
c--- assemble b vector for each axis ---
        err = 0.0
        do 85 irow = 1,3
          do 75 i = 1,ns
            b(i) = 0.0
            do 70 n = 1,num
              if (i .eq.  4) then
                b(i) = b(i) + v(irow,n)
              else
                b(i) = b(i) + v(irow,n) * x(i,n)
              endif
```

```
   70       continue
   75     continue
          call lubksb (a,ns,ns,indx,b)
          write (*,1005) (b(i),i=1,ns)
   85   continue
      endif
  500 goto 10
 1000 format (' *** singular matrix')
 1001 format (' Number of points (0 to quit) ?'$)
 1002 format (4x,1p,3e11.3,3x,e11.3)
 1003 format (1x,i3,1p,3e11.3,5x,3e11.3)
 1004 format (' Random locations; computed velocities ...')
 1005 format (4x,1p,3e11.3,3x,e11.3)
 1006 format (' Target strains & rigid-body velocities ...')
 1007 format (' Generated strains & rigid-body velocities ...')
      end
      function uran ()
c
c Uniform random number generator, according to Wichman & Hill,
c Byte, March 1987.
c Seed is set in data statement.
c
      save ix,iy,iz
      data ix,iy,iz /1,10000,3000/
      j  = ix / 177
      k  = ix - 177 * j
      ix = 171 * k - 2 * j
      if (ix .lt.  0) ix = ix + 30269
      j  = iy / 176
      k  = iy - 176 * j
      iy = 172 * k - 35 * j
      if (iy .lt.  0) iy = iy + 30307
      j  = iz / 178
      k  = iz - 178 * j
      iz = 170 * k - 63 * j
      if (iz .lt.  0) iz = iz + 30323
      temp = float(ix)/30269.0 + float(iy)/30307.0 +
float(iz)/30323.0
```

```
uran  = temp - float(ifix(temp))
return
end
```

Chapter Eight

Mean-field Inelastic Behavior of Random Arrays of Identical Spheres

James T. Jenkins Otto D. L. Strack

Abstract

We consider a random array of identical spheres that interact through noncentral contact forces. We assume that the displacement of a contact relative to a center may be calculated from the average strain of the aggregate. The normal component of the contact force is assumed to be Hertzian and the tangential component is assumed to be linearly elastic until frictional sliding occurs. We consider the response of the material in triaxial compression. For monotone deformations, we calculate the evolution of the contact distribution, the volume change, the stress-strain response, the plastic strain, and the strain hardening.

1 Introduction

We are interested in the average small strain response of random granular assemblies that interact through contacts that may slide. This interest originated in attempts to explain the stress-strain behavior, volume changes, and wave propagation observed in deformations of a granular material carried out at a fixed pressure. These experiments were done on hollow cylindrical samples of essentially identical glass spheres confined within a membrane in a true triaxial/torsion device (Chen, Ishibashi, & Jenkins, 198). Consequently, we focus our attention on an idealized material consisting of identical spherical grains and assume that the location of their centers is random.

In triaxial compression and extension, we assume that the deformation of a

sphere in the neighborhood of a contact can be expressed in terms of the average strain of the aggregate. We are aware that, because of irregularities in the arrangement of the particles, differences in the number of contacts per particle, and variations in the magnitude of the contact forces, this mean field assumption is only approximately true. However, we feel that it is worthwhile to derive a complete a theory based on it in order to determine its structure and to obtain its predictions. The structure of more complicated theories can be expected to contain the elements of the simplest theory, and the predictions of the simplest theory can be obtained analytically.

2 Theory

We suppose that the diameter of a sphere is D and that there are n of them per unit volume. We take $\boldsymbol{\alpha}$ to be the unit vector from the center of a sphere to a contact on its surface. The rectangular Cartesian components of the unit vector $\boldsymbol{\alpha}$ are $(\cos\phi\sin\theta, \sin\phi\sin\theta, \cos\theta)$, where θ is the polar angle from the axis of symmetry.

3 Contact Displacement

As mentioned above, we assume that the displacement $\boldsymbol{u}$ of a contact point relative to the center of its sphere is given in terms of the average strain $\boldsymbol{e}$ of the aggregate and the vector from the center of the sphere to the contact by

$$u_i = \frac{D}{2} e_{ij}\alpha_j. \tag{1}$$

In more complicated deformations involving average rotations, the corresponding mean field assumption involves both the average rotation of the aggregate and the average spin of the spheres (Jenkins, 1991).

In triaxial compression or extension, the volume strain Δ (taken positive for a decrease in volume) is

$$\Delta = -(e_{33} + 2e_{11}) \tag{2}$$

and the shear strain γ (half the maximum shear strain) is

$$\gamma = -\frac{1}{2}(e_{33} - e_{11}). \tag{3}$$

The normal displacement δ of a contact point toward a center is, from (1),

$$\delta = \frac{D}{6}(\Delta - 2\gamma + 6\gamma\cos^2\theta). \tag{4}$$

The corresponding tangential displacement $\boldsymbol{s}$ is

$$\boldsymbol{s} = D\gamma \sin\theta \cos\theta \boldsymbol{e}_\theta, \tag{5}$$

where $\boldsymbol{e}_\theta$ is the unit vector in the direction of increasing θ.

4 Contact Force

The force $\boldsymbol{F}(\boldsymbol{\alpha})$ exerted by the sphere at a contact with orientation $\boldsymbol{\alpha}$ has components parallel and perpendicular to $\boldsymbol{\alpha}$:

$$F_i = P\alpha_i - T_i, \tag{6}$$

where $\boldsymbol{T} \cdot \boldsymbol{\alpha} = 0$. In a homogeneous deformation, F is independent of position. Then, because the force exerted on the sphere at a contact is equal and opposite to the force exerted by the sphere, $\boldsymbol{F}(-\boldsymbol{\alpha}) = -\boldsymbol{F}(\boldsymbol{\alpha})$. The magnitudes of the normal and tangential components depend upon the displacement of a contact relative to the center and are, in general, functions of $\boldsymbol{\alpha}$.

Following Hertz, the normal component P is related to the normal component of the displacement (Love, 1927):

$$P = M(6\delta/D)^{3/2}, \tag{7}$$

where M is given in terms of the shear modulus G and Poisson's ratio ν of the material of the spheres by

$$M = \frac{2}{9\sqrt{3}} \frac{GD^2}{(1-\nu)}. \tag{8}$$

Here, for the tangential component of the contact force, we employ a bilinear relationship that incorporates elastic displacement and frictional sliding. Its form depends on the magnitude T of the tangential component relative to the product of the coefficient of friction μ between the spheres and the normal force P. Provided that $T \leq \mu P$, T is related to the magnitude s of the tangential displacement through

$$T = Ks, \tag{9}$$

where the modulus K is that determined by Mindlin (1949) for the initial shearing at a contact subsequent to the application of the normal force:

$$K = \frac{2^{5/3} G^{2/3}}{(2-\nu)} [3(1-\nu)DP]^{1/3}. \tag{10}$$

Otherwise,

$$T = \mu P. \tag{11}$$

Equations (9) through (11) are an integrated bilinear approximation to the more elaborate incremental inelastic behavior discussed by Mindlin and Deresiewicz (1953).

5 Contact Deletion and Sliding

The results concerning contact deletion and sliding in triaxial compression ($\gamma > 0$) are most compactly expressed in terms of

$$b \equiv \Delta - 2\gamma = -3e_{11} \text{ and } c \equiv 6\gamma. \tag{12}$$

Also, it is convenient to restrict our attention to the range $0 \leq \theta \leq \pi/2$.

At the onset of sliding, the tangential displacement s^E is completely elastic. With the help of (9), (11), (7), (8) and (10), its magnitude s^E is given by

$$s^E = T/K = \mu P/K = \hat{\mu}\delta, \tag{13}$$

where

$$\hat{\mu} \equiv \frac{\mu}{3}\frac{2-\nu}{1-\nu}. \tag{14}$$

When (5) and (4) are used in (13), the condition for sliding to begin may be expressed in terms of b, c, and θ as

$$c \sin\theta \cos\theta = \hat{\mu}(b + c\cos^2\theta). \tag{15}$$

Sliding does not occur while the function $g(\theta)$, defined as

$$g(\theta) \equiv s - \hat{\mu}\delta = \frac{D}{12}[c(\sin 2\theta - \hat{\mu}\cos 2\theta - \hat{\mu}) - 2\hat{\mu}b] \tag{16}$$

is negative. The first zero for $g(\theta)$ occurs in the interior of the interval at the value θ_c for which $dg/d\theta = 0$. We have, from (16), that

$$\frac{dg}{d\theta} = \frac{Dc}{6}(\cos 2\theta_c + \hat{\mu}\sin 2\theta_c) = 0 \tag{17}$$

or

$$\cot 2\theta_c = -\hat{\mu} \tag{18}$$

Note that θ_c is independent of b and c and greater than $\pi/4$.

Substitution of θ_c for θ in $g(\theta_c) = 0$ yields the relation between b and c at the onset of sliding:

$$c = -2b\frac{\cos 2\theta_c}{1 + \cos 2\theta_c}. \tag{19}$$

With (18), (16) may be written as

$$g(\theta) = \frac{D}{12}\cot 2\theta_c \left\{ c\left[\frac{\cos 2(\theta - \theta_c)}{\cos 2\theta_c} + 1\right] + 2b \right\}. \tag{20}$$

In further shearing,

$$c \geq -2b\frac{\cos 2\theta_c}{1 + \cos 2\theta_c} \geq 0. \tag{21}$$

Sliding then occurs over a range of angles $\theta_m \leq \theta \leq \theta_M$, where, when $b \geq 0$, θ_m and θ_M are obtained as the roots of $g(\theta) = 0$:

$$\cos 2(\theta - \theta_c) = -\left(1 + 2\frac{b}{c}\right)\cos 2\theta_c. \tag{22}$$

The roots are

$$\theta_m = \theta_c - \tfrac{1}{2}\arccos\left[\left(1 + 2\frac{b}{c}\right)\cos 2\theta_c\right] \tag{23}$$

and

$$\theta_M = \theta_c + \tfrac{1}{2}\arccos\left[\left(1 + 2\frac{b}{c}\right)\cos 2\theta_c\right]. \tag{24}$$

Contact is effectively lost at those contacts at which the normal component of the contact force has relaxed to zero or, equivalently, when δ, given by (4), vanishes. In triaxial compression, contact is first lost at $\theta = \pi/2$ when $b = 0$. In order to characterize further loss of contact, we define an angle θ_1 by

$$\theta_1 \equiv \begin{cases} \pi/2, & \text{when } b \geq 0 \\ \arccos\sqrt{-b/c}, & \text{when } b \leq 0. \end{cases} \tag{25}$$

Then, when $b \leq 0$, contact is lost over the range in angle $\theta_1 \leq \theta \leq \pi/2$ and sliding takes place over the range $\theta_m \leq \theta \leq \theta_M$, with θ_M given by (24) and $\theta_M = \theta_1$.

When sliding occurs, the magnitude s^P of the part of the tangential displacement associated with it is equal to the function $g(\theta)$:

$$s^P \equiv g(\theta) = \frac{D}{6}[c\sin\theta\cos\theta - \hat{\mu}(b + c\cos^2\theta)], \tag{26}$$

where $\theta_m \leq \theta \leq \theta_M$.

For glass, typical values of μ and ν are 0.3 and 0.2, respectively, so $\hat{\mu} = 0.225$. This value of $\hat{\mu}$ is used when displaying the results of the calculations.

6 Contact Distribution

Let $d\omega = \sin\theta d\theta d\phi$ be the element of solid angle centered at $\boldsymbol{\alpha}$. The orientational distribution of contacts $A(\boldsymbol{\alpha})$ is defined so that $A(\boldsymbol{\alpha})d\omega$ is the probable number of contacts in this element of solid angle. Then the average number k of contacts per particle, called the coordination number, is

$$k = \iint A(\boldsymbol{\alpha})d\omega, \tag{27}$$

where the integration is over all solid angle. In homogeneous situations, the distribution function is independent of position and, because a contact is common to two spheres, $A(-\boldsymbol{\alpha}) = A(\boldsymbol{\alpha})$.

When the distribution of contacts is isotropic, $A(\boldsymbol{\alpha}) = k/4\pi$. When the contact distribution is not isotropic, but there are orthogonal planes of symmetry or an axis of symmetry, the distribution function may be approximated by the first two terms in an expansion in terms of completely symmetric, traceless tensors (Cowin, 1985; Onat & Leckie, 1988):

$$A(\boldsymbol{\alpha}) \doteq \frac{k}{4\pi}(1 + a_{ij}\alpha_i\alpha_j), \tag{28}$$

where

$$a_{ij} \equiv \frac{15}{2}\frac{1}{k}\iint A(\boldsymbol{\alpha})(\alpha_i\alpha_j - \frac{1}{3}\delta_{ij})d\omega. \tag{29}$$

When the distribution exhibits transverse isotropy, $\boldsymbol{\alpha}$ may be expressed in terms of the unit vector $\boldsymbol{h}$ in the direction of the axis of anisotropy and the strength ε of the anisotropy (Jenkins, 1988):

$$a_{ij} = -\varepsilon(\delta_{ij} - 3h_ih_j), \tag{30}$$

where $0 \leq \varepsilon \leq 1$. In this event, the approximation to the distribution function is

$$A(\boldsymbol{\alpha}) \doteq \frac{k}{4\pi}[(1-\varepsilon) + 3\varepsilon(h_i\alpha_i)^2] \tag{31}$$

and ε is related to the exact distribution function by

$$\varepsilon(h_ih_j - \frac{1}{3}\delta_{ij}) = \frac{5}{2}\frac{1}{k}\iint A(\boldsymbol{\alpha})(\alpha_i\alpha_j - \frac{1}{3}\delta_{ij})d\omega. \tag{32}$$

7 Evolution of the Contact Distribution

As grains slide at contacts, the orientational anisotropy of the granular material will change. For example, an initially isotropic distribution will, when subjected

to triaxial compression, develop transverse anisotropy along the axis of loading. The magnitude of the anisotropy will increase with increasing deformation and it will be reinforced when the average strain increases to the point where contacts are deleted. It follows from equation (26) that the sliding displacement is of the order of magnitude of the strains and from (25) that the contact deletion depends upon the ratio of the strains. Consequently, when contact deletion occurs, its contribution to the fabric is much larger than that of contact sliding. For this reason we neglect the effect of sliding on the fabric and focus on that due to contact deletion. The fabric associated with contact deletion influences the propagation of waves through the aggregate (Cundall, Jenkins and Ishibashi, 1989).

There is a relatively simple relationship between the coordination number k_1 of a deformed aggregate and the coordination number k of its initial, supposedly isotropic, state. For example, in triaxial compression, we have

$$k_1 = 4\pi \int_0^{\theta_1} \frac{k}{4\pi} \sin\theta d\theta, \tag{33}$$

where θ_1 is defined by (25). The integration gives

$$k_1 = k(1 - \cos\theta_1). \tag{34}$$

In order to obtain an analogous equation of evolution for the strength of the anisotropy ε, we employ the initial distribution function $A(\boldsymbol{\alpha}) = k/4\pi$ in (32):

$$\varepsilon = \frac{15}{4}\frac{k}{k_1}\int_0^{\theta_1} (\cos^2\theta - \frac{1}{3})\sin\theta d\theta \quad . \tag{35}$$

In this case,the integration yields

$$\varepsilon = \frac{5}{4}\frac{k}{k_1}\sin^2\theta_1\cos\theta_1 = \frac{5}{4}(1+\cos\theta_1)\cos\theta_1. \tag{36}$$

Once a relation between the volume strain and the shear strain is known, this provides the explicit expression for the evolution of the fabric with increasing shear strain.

We note that in our subsequent calculations of the stress, we employ the exact distribution function based upon the deletion of contacts from the initial isotropic distribution function rather than the approximate distribution function based on the fabric tensor (30).

8 Stress

Following Cauchy, an expression for the average stress tensor $\boldsymbol{t}$ associated with a homogeneous deformation of the aggregate may be obtained by considering the force transmitted over an arbitrary element of area by pairs of contacting spheres whose line of centers is cut by the area element (Love, 1927, Note B). For random assemblies, the stress is naturally expressed in terms of the orientational distribution function and the contact force:

$$t_{ij} = -\frac{Dn}{2} \iint A(\boldsymbol{\alpha}) F_i(\boldsymbol{\alpha}) \alpha_j d\omega, \tag{37}$$

where the integration is taken over the entire solid angle.

When the orientational distribution of contacts is initially isotropic, the stress may be expressed in terms of the coordination number, the solid volume fraction $v \equiv \pi D^3 n/6$, and the components of the contact force (6):

$$t_{ij} = -\frac{3}{4\pi^2} \frac{kv}{D^2} \iint (P\alpha_i - T_i)\alpha_j d\omega. \tag{38}$$

where the integrals are taken over all contacts.

9 Pressure

The relation between the pressure p and the strain for an initially isotropic contact distribution is, from (38),

$$p \equiv -\frac{1}{3} t_{ii} = \frac{1}{4\pi^2} \frac{kv}{D^2} \iint P d\omega. \tag{39}$$

where the integration is over all contacts. We note that the pressure does not depend on the tangential component of the contact force. When (8) and (4) are used in (39) and the result integrated over ϕ from 0 to 2π, we obtain

$$p = \frac{kvM}{\pi D^2} \int_0^{\theta_1} (b + c\cos^2\theta)^{3/2} \sin\theta d\theta. \tag{40}$$

If there were no shear strain, the volume strain Δ_0 and the pressure p would be related by

$$\Delta_0^{3/2} = \frac{\pi D^2}{kvM} p. \tag{41}$$

This volume strain provides a natural scale for both the volume strain and the shear strain in triaxial compression. Jenkins, Cundall, and Ishibashi (1989) indicate how to obtain Δ_0 in numerical simulations and physical experiments from the incremental form of (41) applied at the initial isotropic state of the sample.

For triaxial compression, the integral in (40) gives (Jenkins, 1988)

$$8\Delta_0^{3/2} = (5b + 2c)\sqrt{b + c} + \frac{3b^2}{\sqrt{c}} \ln\left(\frac{\sqrt{c} + \sqrt{b + c}}{\sqrt{|b|}}\right). \tag{42}$$

When expressed in terms of Δ/Δ_0 and γ/Δ_0, equation (42) provides an implicit relation between the normalized volume strain and the normalized shear strain in triaxial compression. Because the pressure enters only through Δ_0, a single relation between these normalized variables applies no matter what the variation of the pressure.

In Figure 1 we plot Δ/Δ_0 versus γ/Δ_0.

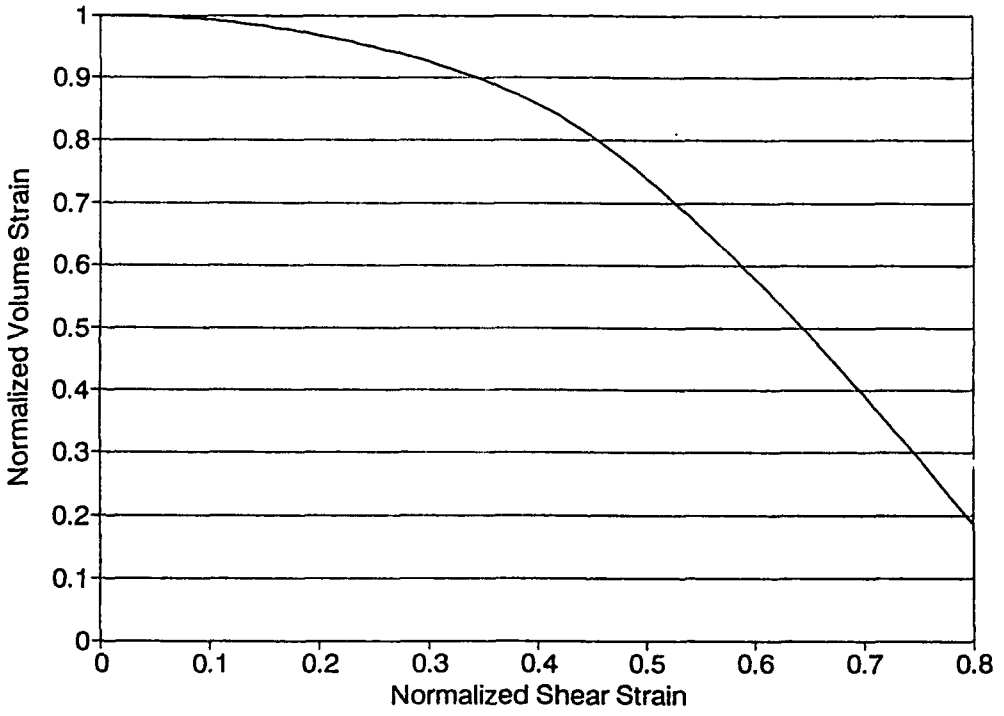

Figure 1: Δ/Δ_0 versus γ/Δ_0.

With (42) providing the relationship between b and c, we can graph the variation of θ_m, θ_M, θ_1, and ε with shear strain in triaxial compression. In Figure 2 we show the evolution of the regions of slip and lost contact with normalized shear strain γ/Δ_0.

In Figure 3 we indicate how ε varies with γ/Δ_0 as contact are deleted. Values of ε greater than one correspond to negative values of the approximate distribution function and indicate a breakdown of the approximation.

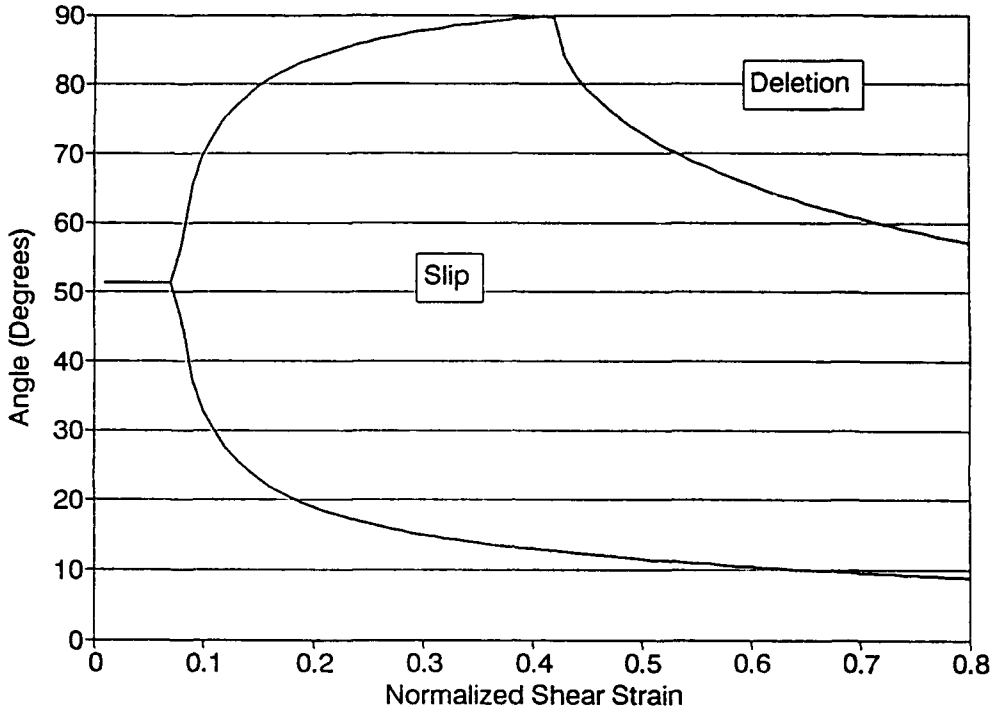

Figure 2: θ_M and θ_l bounding the region of slip from above and θ_m bounding the region of slip from below.

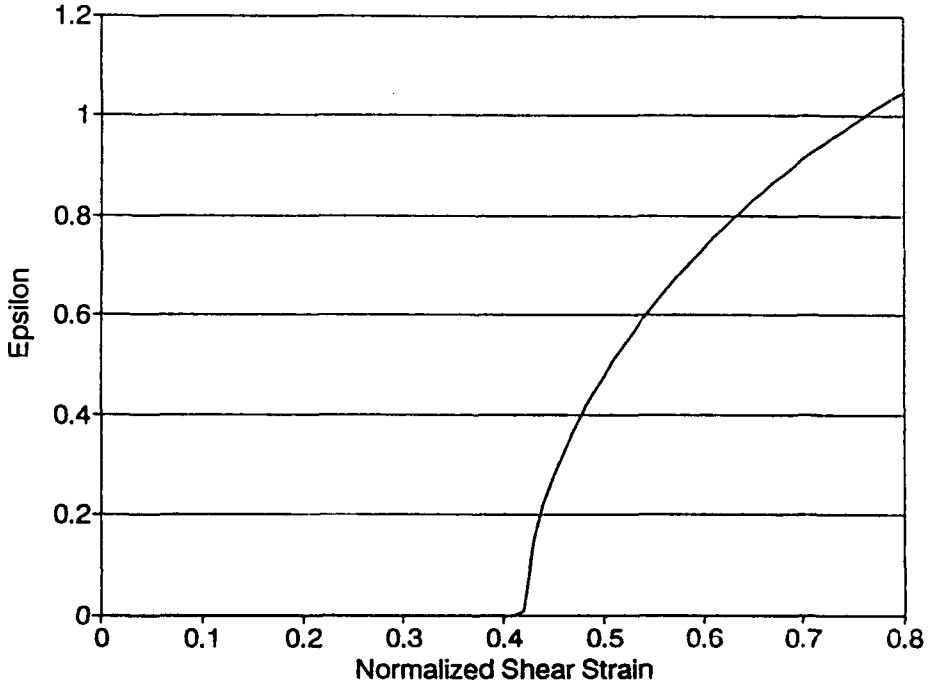

Figure 3: ϵ versus γ/Δ_0.

10 Shear Stress

The shear stress q,

$$q \equiv -\frac{1}{2}(t_{33} - t_{11}), \tag{43}$$

contains contributions from the normal and tangential components of the contact force. We first consider the part q^N contributed by the normal component.

From (38),

$$q^N = \frac{3}{8\pi^2}\frac{kv}{D^2}\iint P(\alpha_3^2 - \alpha_1^2)d\omega \tag{44}$$

Upon using (7) and (4) in (44) and carrying out the integral over ϕ, we obtain

$$q^N = \frac{3}{2\pi}\frac{kvM}{D^2}\int_0^{\theta_1}(b + c\cos^2\theta)^{3/2}(3\cos^2\theta - 1)\sin\theta d\theta. \tag{45}$$

Upon carrying out the remaining integration and using (41), we have, for triaxial compression,

$$q^N = \frac{3}{64}\frac{p}{\Delta_0^{3/2}}\left[\frac{\sqrt{b+c}}{c}(3b^2 + 4bc + 4c^2) - 3\frac{b^2}{c^{3/2}}(b + 2c)\ln\left(\frac{\sqrt{c} + \sqrt{b+c}}{\sqrt{|b|}}\right)\right] \tag{46}$$

Equation (46), used with (42) gives q^N/p as a function of γ/Δ_0. We note that smooth particles can sustain a shear stress and that the angle of internal friction, $\sin^{-1}(q^N/p)$ varies with the shear strain.

The calculation of the part q^T of the shear stress associated with the tangential component of the contact force is more complicated because its bilinear nature requires us to employ our characterizations of the onset and extent of contact sliding. When the forms of the bilinear relation (9) - (11) that are appropriate to the elastic and frictional regions are employed in (43), q^T may be written, after an integration over ϕ, as

$$\begin{aligned} q^T = &\frac{27}{4}\frac{p}{\Delta_0^{3/2}}\frac{(1-\nu)}{(2-\nu)}\left\{\int_0^{\theta_1} c(b + c\cos^2\theta)^{1/2}\sin^3\theta\cos^2\theta d\theta\right. \\ &\left. - \int_{\theta_m}^{\theta_M}[c\sin\theta\cos\theta - \hat{\mu}(b + c\cos^2\theta)](b + c\cos^2\theta)^{1/2}\sin^2\theta\cos\theta d\theta\right\} \end{aligned} \tag{47}$$

Upon carrying out the integrals using the definition (25) of θ_1, we obtain

$$
\begin{aligned}
q^T = & \frac{p}{\Delta_0^{3/2}} \frac{(1-\nu)}{(2-\nu)} \frac{27}{4} \Bigg\{ \frac{\sqrt{b+c}}{48c}(3b^2+4bc+4c^2) \\
& - \frac{b^2}{16c^{3/2}}(b+2c)\ln\left(\frac{\sqrt{c}+\sqrt{b+c}}{\sqrt{|b|}}\right) \\
& - \hat{\mu}\sin\theta_M \frac{(b+c\cos^2\theta_M)^{1/2}}{48c}[8(b+c\cos^2\theta_M)^2 \\
& - 2(b+c)(b+c\cos^2\theta_M) - 3(b+c)^2] \\
& + \hat{\mu}\sin\theta_m \frac{(b+c\cos^2\theta_m)^{1/2}}{48c}[8(b+c\cos^2\theta_m)^2 \\
& - 2(b+c)(b+c\cos^2\theta_m) - 3(b+c)^2] \\
& + \hat{\mu}\frac{(b+c)^3}{16c}[J(\sin\theta_M) - J(\sin\theta_m)]
\end{aligned}
$$

$$
\begin{aligned}
& - \frac{(b+c\cos^2\theta_M)^{1/2}}{48c}\cos\theta_M[8\cos^2\theta_M c(b+c\cos^2\theta_M) \\
& - 6(b+2c)(b+c\cos^2\theta_M) + 3b(b+2c)] \\
& + \frac{(b+c\cos^2\theta_m)^{1/2}}{48c}\cos\theta_m[8\cos^2\theta_m c(b+c\cos^2\theta_m) \\
& - 6(b+2c)(b+c\cos^2\theta_m) + 3b(b+2c)] \\
& - \frac{b^2}{16c}(b+2c)[I(\cos\theta_M) - I(\cos\theta_m)]\Bigg\}, \qquad (48)
\end{aligned}
$$

where

$$
I(u) \equiv \frac{1}{\sqrt{c}}\ln(u\sqrt{c}+\sqrt{b+cu^2}) \qquad (49)
$$

and

$$
J(u) \equiv \frac{1}{\sqrt{c}}\arcsin\left(u\sqrt{\frac{c}{b+c}}\right), \qquad (50)
$$

with θ_m given by (23) and θ_M given by (24) when $b \geq 0$ or $\theta_M = \arccos\sqrt{-b/c}$ when $b \leq 0$. Equation (48) used with (42) determines the part of the shear stress associated with the tangential component of the contact force as a function of the shear strain. It corrects the corresponding exprssion for q^T given by Jenkins and Strack (1992).

In Figure 4 we plot the q^T and q^N, normalized by the pressure, versus the normalized shear strain.

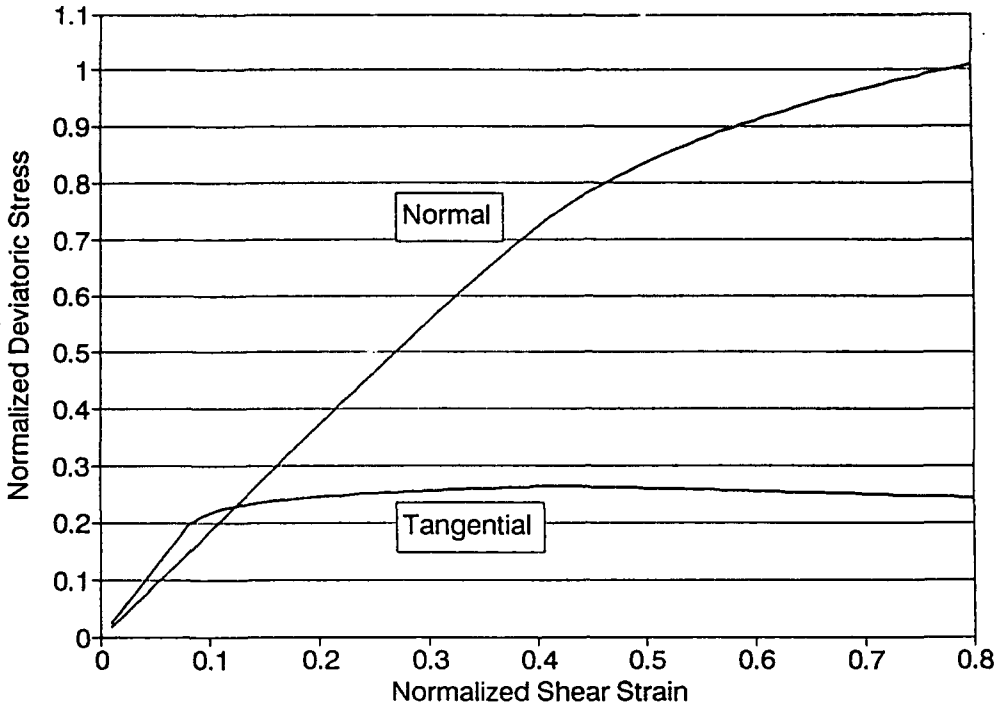

Figure 4: q^N/p and q^T/p versus γ/Δ_0.

The relative magnitudes of q^N and q^T are consistent with Cundall's (1988) observation that in a corresponding numerical simulation q^T was only about fifteen percent of q^N.

11 Plastic Strain

The average plastic strain e^P associated with the sliding displacement s^P has the components

$$e_{ij}^P = \frac{3}{8\pi D} \iint (s_i^P \alpha_j + s_j^P \alpha_i) d\omega \tag{51}$$

where the integration is over the solid angle subtended by the region of sliding. We note that $e_{ii}^P = 0$, so that there is no plastic volume change. This is not inconsistent with the relatively small inelasticity in the volume strain in a corresponding numerical simulation by Cundall, Jenkins, and Ishibashi (1989).

The plastic shear strain γ^P is

$$\gamma^P = -\frac{1}{2}(e_{33}^P - e_{11}^P) = -\frac{3}{8\pi D} \iint (s_3^P \alpha_3 - s_1^P \alpha_1) d\omega \tag{52}$$

or, after an integration over ϕ,

$$\gamma^P = \frac{3}{4} \int_{\theta_m}^{\theta_M} [c \sin\theta \cos\theta - \hat{\mu}(b + \cos^2\theta)] \sin^2\theta \cos\theta d\theta \tag{53}$$

So,

$$\gamma^P = -\frac{1}{20}c[(2+3\sin^2\theta_M)\cos^3\theta_M - (2+3\sin^2\theta_m)\cos^3\theta_m]$$
$$-\hat{\mu}[\frac{1}{4}(b+c)(\sin^3\theta_M - \sin^3\theta_m) - \frac{3}{20}c(\sin^5\theta_M - \sin^5\theta_m)]. \qquad (54)$$

In Figure 5 we plot γ^P/Δ_0 versus γ/Δ_0.

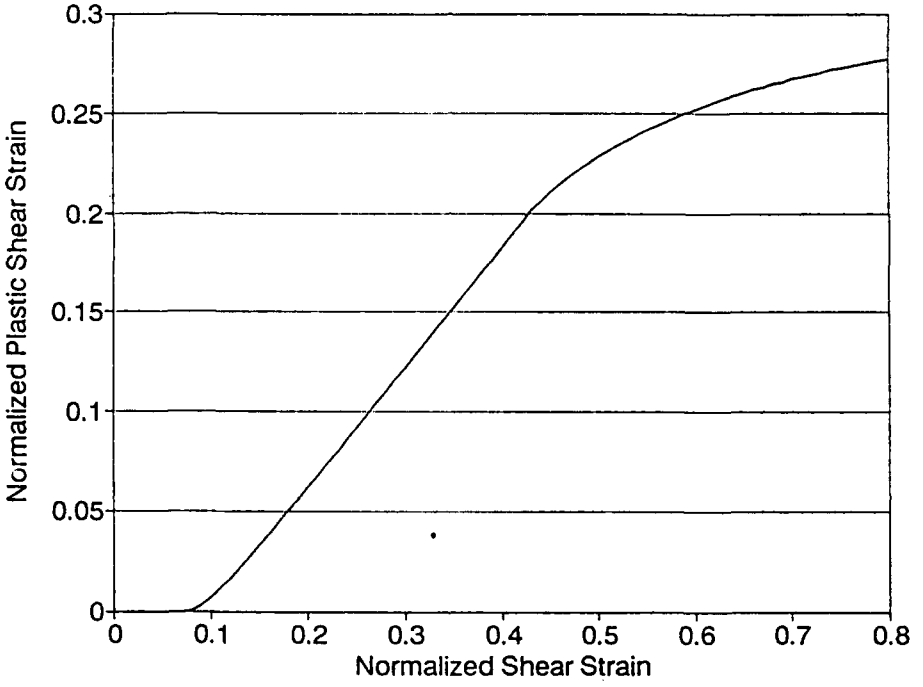

Figure 5: γ^P/Δ_0 versus γ/Δ_0.

12 Strain Hardening

For a given value of the plastic strain, yield in the q-p plane occurs on the family of straight lines

$$q/p = h(\gamma^P), \qquad (55)$$

where $h(\gamma^P)$ is the strain hardening function. Because as a consequence of the kinematic assumption (1) there is no plastic volume strain, curves of constant plastic potential are straight lines parallel to the p axis. The strain hardening function may be obtained numerically by first determining q/p from (46) and (48), then by using (42) to express q/p and γ^P/Δ_0 as functions of γ/Δ_0 alone, and, finally, by

eliminating the parameter γ/Δ_0 to obtain q/p in terms of γ^P/Δ_0. In Figure 6 we show the normalized shear stress versus the normalized plastic strain. This shows the initial elastic response, yield, and the subsequent strain hardening.

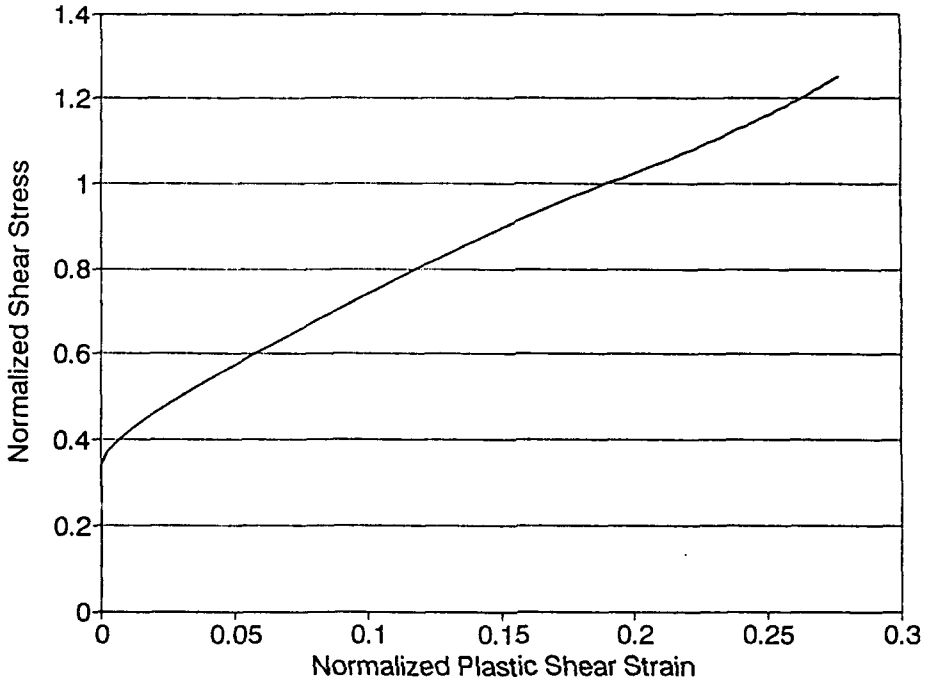

Figure 6: q/p versus γ^P/Δ_0.

Concluding Remarks

Although the results obtained apply most naturally to situations in which the variation of the shear strain is prescribed and the pressure is held fixed, it is important to emphasize that they are not so restricted. For example, they also apply when both the shear strain and the pressure are varied arbitrarily. In any case, the relations obtained are universal in the sense that, when the stresses are normalized by p and the strains are normalized by Δ_0, a single curve describes the results of all triaxial compression experiments.

Numerical simulations are in progress to determine the ways in which the kinematic hypothesis (1), on which the analysis is based, might be improved.

References

Chen, Y. C., Ishibashi, I. and Jenkins, J. T. 1988. Dynamic shear modulus and

fabric: part I, depositional and induced fabric. *Géotechnique*, Vol. 38, No. 1, pp. 25–32.

Cowin, S.C. 1985 The relationship between the elasticity tensor and the fabric tensor. *Mechanics of Materials*, Vol. 4, pp. 137–147.

Cundall, P.A. 1988. Computer simulations of dense sphere assemblies. In *Micromechanics of Granular Materials.* (Satake, M. and Jenkins, J.T., Eds.) pp.113–125, Elsevier: Amsterdam.

Cundall, P.A., Jenkins, J.T. and Ishibashi, I. 1989. Evolution of elastic moduli in a deforming granular assembly. In *Powders and Grains.* (Biarez, J. and Gourvès, R., Eds.) pp.319-322, Balkema:Rotterdam.

Jenkins, J. T. 1988. Volume change in small strain axisymmetric deformations of a granular material. In *Micromechanics of Granular Materials* (Satake, M. and Jenkins, J. T., Eds.) pp. 245–252, Elsevier: Amsterdam.

Jenkins, J. T. 1991. Anisotropic elasticity for random arrays of identical spheres. In *Modern Theory of Anisotropic Elasticity and Applications* (Wu, J.J., Ting, T.C.T., and Barnett, D.M., Ed.) pp. 368-377 SIAM: Philadelphia.

Jenkins, J.T., Cundall, P.A. and Ishibashi, I. 1989. Micromechanical modeling of granular materials with the assistance of experiments and numerical simulations. In *Powders and Grains* (Biarez, J. and Gourvès, R. Eds.) pp. 257-264,Balkema :Rotterdam.

Jenkins, J.T. and Strack, O.D.L. Mean-field stress-strain reelations for random arrays of identical spheres in triaxial compression. In *Advances in Micromechanics of Granular Materials* (Shen, H. et. al., Eds.) pp. 41–50, Elsevier :Amsterdam.

Love, A. E. H. 1927. *A Treatise on the Mathematical Theory of Elasticity.* Cambridge University Press: Cambridge.

Mindlin, R. D. 1949. Compliance of elastic bodies in contact. *Journal of Applied Mechanics*, Vol. 16, pp. 259–268.

Mindlin, R. D. and Deresiewicz, H. 1953. Elastic spheres in contact under varying oblique forces. *Journal of Applied Mechanics*, Vol. 20, pp. 327–344.

Onat, E.T. and Leckie, F.A. 1988. Representation of mechanical behavior in the presence of changing internal structure. *Journal of Applied Mechanics, Vol. 55, pp.1–10.*

Chapter Nine

The Plastic Anisotropy and Average Plastic Spin for Planar Polycrystalline Aggregates

Vincent C. Prantil James T. Jenkins Paul R. Dawson

Abstract

Significant changes in the mechanical state of polycrystalline metals accompany the large deformations associated with forming operations. For example, crystallographic texture is one important source of the developing anisotropy in the flow stress in these materials. In order to construct a continuum description of such anisotropy, we examine the texturing of an idealized planar assembly of two-dimensional grains. We derive equations of evolution for the grain orientation and express them in terms of the macroscopic deformation rate and a single microstructural parameter. An analytic expression for the plastic spin is determined in terms of this parameter. We introduce a continuous distribution function to describe the orientations of the grains in the aggregate. We focus on the second moment of the distribution and derive the differential equations governing its evolution. We derive the equation for the average plastic spin and express it in terms of the microstructural parameter and the second moment. This provides a micromechanical foundation for recent phenomenological proposals for the form of the plastic spin.

1 Introduction

Many metal alloys produced and formed commercially are inherently polycrystalline in nature. Each continuum point is composed of many anisotropic grains or single crystals. When such metals undergo extensive inelastic flow and the grains preferentially reorient, the response of the polycrystalline aggregate can become anisotropic. The resulting anisotropy is often referred to as texture. The material properties are defined by a suitable average response of the collection of individual grains. The focus of this work involves using a polycrystalline plasticity model to construct analytical expressions describing the aggregate texturing and the anisotropic macroscopic response

of the material. In the process, natural microstructural variables are identified that survive averaging and determine the macroscopic anisotropy. Here we concentrate on obtaining such an expression for the continuum plastic spin.

We begin with a brief description of the geometry of crystallographic slip in a single crystal undergoing primary-conjugate multiple slip. This is followed by an outline of the polycrystalline framework. A mean field assumption is introduced to link the macroscopic and microscopic length scales. This is followed by a relatively detailed description of the kinematics appropriate at the microscopic level of the single crystal. For the case of the kinematically determined multiple slip, the slip system shearing rates are determined and a microstructural parameter is identified that enters naturally into expressions for the plastic spin.

The polycrystalline aggregate is incorporated by means of an orientation distribution function (ODF). Using an expansion introduced by Onat and Leckie (1988), a set of even order tensors that characterize the moments of the distribution are identified. Appealing to the conservation principle governing the field of grain orientations outlined by Clément (1982) and Arminjon (1987), evolution equations for the moment tensors based on analogous treatments by Advani and Tucker (1987,1990) are presented. In planar flows, these can be used to continually update the ODF. A continuum level expression for the plastic spin is derived by orientation averaging. We show how the average plastic spin depends on the microstructural parameter characterizing the single crystal anisotropy and how this spin is related to the spin of the principal directions of the developing anisotropy.

2 Polycrystalline framework

We investigate the material behavior of a planar single crystal undergoing primary-conjugate double slip. The material point is assumed to be composed of a large number of grains, each characterized by its orientation relative to some fixed reference frame. The developing texture manifests itself in a non-uniform distribution of grain orientations, modeled here by a continuous orientation distribution function. We proceed from the polycrystalline model and adopt a mean field assumption to determine the flow at the microscopic level. We use this in conjunction with a multiplicative decomposition of the grain deformation gradient to determine the single crystal response. The evolving ODF is then used to compute orientation averages for the macroscopic behavior of the crystalline aggregate.

To construct the model, we adopt several simplifying assumptions that allow us to capture the pertinent features of the anisotropy at the grain level and understand how their averages deliver anisotropic descriptions on the macroscopic level. We assume the point is undergoing fully developed

plastic flow and neglect elasticity; suppose the plastic flow is isochoric; and restrict our attention to planar motions.

2.1 Microstructural Geometry of a Double Slip Single Crystal

We consider a double slip single crystal as described by Asaro (1983). In each grain the deformation can be accommodated by slip on two independent slip planes, each identified with their unit normal vector, $\boldsymbol{\eta}^{(\alpha)}$. Further, the crystallographic slip occurs along a unique slip direction, $\boldsymbol{\nu}^{(\alpha)}$, defined in each plane. We, thus, characterize the crystal by the set of time-dependent, orthonormal pairs $(\boldsymbol{\eta}^{(\alpha)},\boldsymbol{\nu}^{(\alpha)})$ imbedded in the lattice. These slip systems are fixed relative to the lattice frame and to one another, as illustrated in Figure 1.

For convenience, two Cartesian reference frames are employed to describe individual grain orientations with respect to the macroscopic material point. One is fixed in space and characterized by the time-independent orthonormal basis, $\{\boldsymbol{e}_1, \boldsymbol{e}_2\}$. The second is fixed in the lattice frame and identified with the time-dependent, orthonormal basis, $\{\boldsymbol{\alpha}, \boldsymbol{\alpha}_\perp\}$, where $\boldsymbol{\alpha}$ is a vector in the plane which bisects the acute angle formed by the pair of slip directions. This vector can be used to uniquely describe the orientation of the lattice frame, and therefore the crystal, in space. The initial texture of the aggregate is defined by the distribution of initial scalar orientations, θ_n for n individual grains. To resolve the evolving texture, it is necessary to compute the reorientation of individual grains with continuing deformation.

2.2 Mean Field Assumption

In order to resolve the response of the individual crystals, it is necessary to understand the kinematics and constitutive response on the slip system level. In the context of polycrystalline plasticity this is accomplished by adopting one of several hypotheses relating the kinematics on the grain level to those on the macroscopic level. Because we appeal to the microstructure underlying the material point to describe its anisotropy, we must make physically motivated assumptions in traversing these length scales. Based on the classical work of Taylor (1938), we assume a homogeneous deformation throughout the aggregate. The deformation gradient experienced by each grain is equal to the deformation gradient experienced by the collection of grains underlying the material point

$$\mathbf{F}^{\mathbf{g}} = \mathbf{F} = \frac{\partial \boldsymbol{x}}{\partial \boldsymbol{X}} \; ; \; \boldsymbol{x} = \boldsymbol{x}(\boldsymbol{X}, t). \tag{1}$$

Therefore, each individual grain experiences the macroscopic or continuum deformation gradient. This assumption ensures an entirely compatible de-

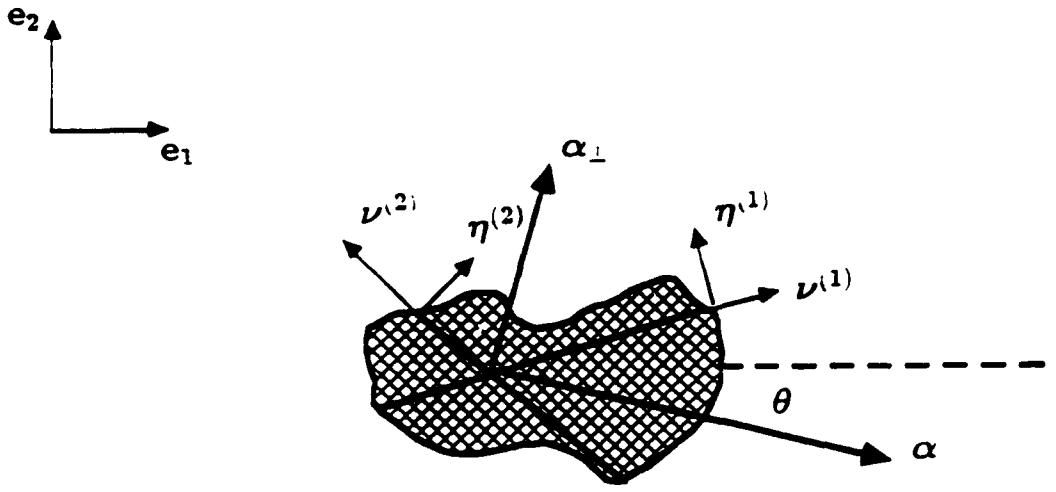

Figure 1: The microstructural unit model: a planar single crystal oriented at angle θ, the scalar measure of grain orientation corresponding to the vector $\boldsymbol{\alpha}$.

formation field. It has been shown to be reasonable for moderate amounts of deformation in single phase metals whose single crystals are characterized by a number of slip systems sufficient to allow an arbitrary motion.

3 Kinematics

At the grain level, we adopt a multiplicative decomposition of the deformation as illustrated in Figure 2. The first portion, $\mathbf{F}^{\mathbf{p}}$, consists solely of volume preserving plastic slip, defining an intermediate configuration, $\bar{\mathcal{B}}$, in which the lattice remains fixed. This crystallographic slip takes place by the relative shearing of neighboring close-packed planes of atoms. In the absence of elasticity, the remainder of the deformation consists of a rigid rotation, $\mathbf{R}^{*}$, of the lattice frame to the current configuration, $\mathcal{B}$. The total deformation experienced by the grain is given by

$$\mathbf{F}^{\mathbf{g}} = \mathbf{R}^{*}\mathbf{F}^{\mathbf{p}} \tag{2}$$

The rate form of the multiplicative decomposition is an additive decomposition of the form

$$\mathbf{L} = \mathbf{L}^{\mathbf{g}} = \dot{\mathbf{F}}\mathbf{F}^{-1} = \dot{\mathbf{R}}^{*}\mathbf{R}^{*\mathbf{T}} + \mathbf{R}^{*}\bar{\mathbf{L}}^{\mathbf{p}}\mathbf{R}^{*\mathbf{T}} \tag{3}$$

where

$$\bar{\mathbf{L}}^{\mathbf{p}} = \dot{\mathbf{F}}^{\mathbf{p}}\mathbf{F}^{\mathbf{p}-1} \tag{4}$$

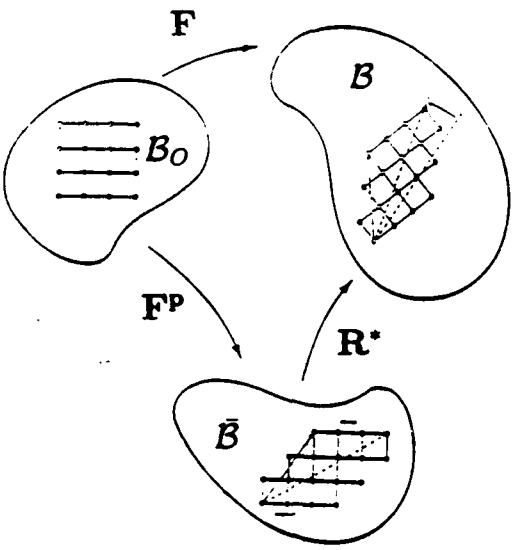

Figure 2: Multiplicative decomposition describing the kinematics of crystallographic slip in the single crystal.

is the microscopic velocity gradient in the intermediate configuration. When crystallographic slip is the only mechanism for plastic flow in the crystal, the velocity gradient in the current configuration can be defined in terms of the slip system geometry

$$\mathbf{L}^{\mathbf{P}} = \sum_{\alpha=1,2} \dot{\gamma}^{(\alpha)} \mathbf{T}^{(\alpha)} \tag{5}$$

where $\dot{\gamma}^{(\alpha)}$ is the rate of shearing along slip system α and

$$\mathbf{T}^{(\alpha)} = \boldsymbol{\nu}^{(\alpha)} \otimes \boldsymbol{\eta}^{(\alpha)} \tag{6}$$

is the slip system Schmid orientation tensor. Physically, $\bar{\mathbf{L}}^{\mathbf{P}}$ is the velocity gradient accommodated by plastic flow through the fixed lattice. In general, the spin associated with this plastic flow, $\boldsymbol{\omega}^{\mathbf{P}}$, will differ from the overall spin of material in the grain, $\boldsymbol{\omega}$. This occurs because the crystal has available to it only a limited number of deformation modes to accommodate plastic deformation. The difference between these rates of rotation then results in a subsequent rigid rotation of the imbedded lattice

$$\boldsymbol{\omega}^{\boldsymbol{\ell}} = \dot{\mathbf{R}}^* \mathbf{R}^{*\mathbf{T}} \tag{7}$$

necessary to enforce the mean field assumption and maintain compatibility across grain boundaries. The grain velocity gradient can also be decomposed into its symmetric and skew portions. It follows directly from (1) that the Taylor assumption carries through the rate form so that from (3) the grain rate of deformation and grain spin can be written

$$\mathbf{d} = \mathbf{d}^{\mathbf{P}} = \mathbf{R}^* (\bar{\mathbf{L}}^{\mathbf{P}})_{sym} \mathbf{R}^{*\mathbf{T}} \tag{8}$$

$$\omega = \omega^{\prime} + \omega^{\mathrm{P}} \tag{9}$$

where

$$\omega^{\mathrm{P}} = \mathbf{R}^{*}(\bar{\mathbf{L}}^{\mathrm{P}})_{skew}\mathbf{R}^{*\mathrm{T}} \tag{10}$$

As a consequence of the slip geometry, the symmetric and skew portions of the microscopic velocity gradient can be expressed in terms of the respective portions of the Schmidt tensors as

$$\begin{aligned} \mathbf{d}^{\mathrm{P}} &= \sum_{\alpha=1,2} \frac{\dot{\gamma}^{(\alpha)}}{2}(\boldsymbol{\nu}^{(\alpha)} \otimes \boldsymbol{\eta}^{(\alpha)} + \boldsymbol{\eta}^{(\alpha)} \otimes \boldsymbol{\nu}^{(\alpha)}) \\ &= \sum_{\alpha=1,2} \dot{\gamma}^{(\alpha)}\mathbf{P}^{(\alpha)} \end{aligned} \tag{11}$$

$$\begin{aligned} \boldsymbol{\omega}^{\mathrm{P}} &= \sum_{\alpha=1,2} \frac{\dot{\gamma}^{(\alpha)}}{2}(\boldsymbol{\nu}^{(\alpha)} \otimes \boldsymbol{\eta}^{(\alpha)} - \boldsymbol{\eta}^{(\alpha)} \otimes \boldsymbol{\nu}^{(\alpha)}) \\ &= \sum_{\alpha=1,2} \dot{\gamma}^{(\alpha)}\mathbf{Q}^{(\alpha)} \end{aligned} \tag{12}$$

where

$$\mathbf{T}^{(\alpha)} = \mathbf{P}^{(\alpha)} + \mathbf{Q}^{(\alpha)} \tag{13}$$

Combining (9) and (12), the lattice spin accompanying plastic straining can be written

$$\boldsymbol{\omega}^{\prime} = \dot{\mathbf{R}}^{*}\mathbf{R}^{*\mathrm{T}} = \boldsymbol{\omega} - \sum_{\alpha=1,2} \dot{\gamma}^{(\alpha)}\mathbf{Q}^{(\alpha)} \tag{14}$$

So, in order to update the grain orientation, it is necessary to resolve the partitioning of shearing rates, $\dot{\gamma}^{(\alpha)}$, among the available slip systems.

4 Kinematic Solution for the Slip System Shear Distribution

The geometry of planar slip dictates that exactly two active slip systems, whose Schmid tensors are linearly independent, are necessary to uniquely accommodate an arbitrary deformation. In the plane, any additional slip system will be linearly dependent upon this set. For such redundant systems, there is no unique kinematic prescription of the slip system shearing rates.

For the planar crystal undergoing double slip, the available number of degrees of freedom is identical to the number of independent components in an incompressible but otherwise arbitrary rate of deformation. In this special case there is a one-to-one correspondence between these two independent components and the shearing rates on the two slip systems. For general isochoric planar flows the velocity gradient has three independent components

that one can associate with a rate of stretching, $\dot{\Gamma}$, a rate of shearing, $\dot{\Lambda}$, and a spin, $\dot{\Omega}$.

$$\begin{aligned} \mathbf{L} &= \dot{\Gamma}(t)(\mathbf{e}_1 \otimes \mathbf{e}_1 - \mathbf{e}_2 \otimes \mathbf{e}_2) \\ &= \dot{\Lambda}(t)(\mathbf{e}_1 \odot \mathbf{e}_2 + \mathbf{e}_2 \odot \mathbf{e}_1) \\ &= \dot{\Omega}(t)(\mathbf{e}_1 \otimes \mathbf{e}_2 - \mathbf{e}_2 \otimes \mathbf{e}_1). \end{aligned} \tag{15}$$

Thus, there is a unique relationship between $\{\dot{\Gamma}, \dot{\Lambda}\}$ and $\{\dot{\gamma}^{(1)}, \dot{\gamma}^{(2)}\}$ in (11). This limited number of degrees of freedom permits one to kinematically determine the pair of shearing rates by projecting the rate of deformation onto the set of basis tensors, $\mathbf{P}^{(\alpha)}$

$$d_\beta = \mathbf{d} : \mathbf{P}^{(\beta)} = \sum_\alpha \dot{\gamma}^{(\alpha)} \mathbf{P}^{(\alpha)} : \mathbf{P}^{(\beta)} = \sum_\alpha \mathcal{P}_{\beta\alpha} \dot{\gamma}^{(\alpha)}, \tag{16}$$

or

$$\dot{\gamma}^{(\alpha)} = \sum_\beta \mathcal{P}^{-1}_{\alpha\beta} d_\beta, \tag{17}$$

where $\mathcal{P}^{-1}$ always exists for $\alpha, \beta = 1, 2$ but becomes rank deficient for redundant systems. Even though straightforward, this step has powerful implications for determining the grain reorientation and updating the texture. In this limit, the slip system shearing rates are determined solely as a function of the macroscopic rate of deformation. And this, in turn, directly determines the plastic spin of material through the lattice in terms of $\mathbf{d}$

$$\begin{aligned} \boldsymbol{\omega}^{\mathrm{p}} &= \sum \dot{\gamma}^{(\alpha)} \mathbf{Q}^{(\alpha)} \\ &= \sum_{\alpha,\beta} \mathcal{P}_{\alpha\beta}{}^{-1} \left[\mathbf{Q}^{(\alpha)} \otimes \mathbf{P}^{(\beta)} \right] : \mathbf{d}. \end{aligned} \tag{18}$$

From this straightforward relation the grain reorientation is cast in a form that explicitly represents the anisotropy inherent in the single crystal.

5 Grain Orientation Update

Recall that the mean field assumption governing the spin of the material on the crystal level dictates the necessary grain reorientation in accordance with (14). In the plane, we can recast this equation in a form that isolates the anisotropy in terms of a single parameter. For planar flows, the two-dimensional rotation tensor is simply a function of the scalar θ

$$[\mathbf{R}^*] = \begin{bmatrix} cos\theta & -sin\theta \\ sin\theta & cos\theta \end{bmatrix}.$$

Combining equation (14) and the solution for the shearing rates given by (17), we obtain an evolution equation for the grain orientation in terms of the current orientation and the macroscopic kinematic quantities

$$\mathring{\boldsymbol{\alpha}} = \dot{\boldsymbol{\alpha}} - \boldsymbol{\omega}\boldsymbol{\alpha} = -\boldsymbol{\omega}^{\mathrm{P}}\boldsymbol{\alpha} \tag{19}$$

The plastic spin is determined explicitly by the relative slip system arrangement in the lattice frame according to (18)

$$-\boldsymbol{\omega}^{\mathrm{P}}\boldsymbol{\alpha} = -\sum_{\alpha=1,2} \dot{\gamma}^{(\alpha)}\mathbf{Q}^{(\alpha)}\boldsymbol{\alpha} = \lambda\boldsymbol{\Xi}\mathbf{d}\boldsymbol{\alpha}, \tag{20}$$

in which $\boldsymbol{\Xi}$ is the projection operator onto the direction $\boldsymbol{\alpha}_\perp$ given by

$$\boldsymbol{\Xi} = \boldsymbol{\alpha}_\perp \otimes \boldsymbol{\alpha}_\perp = \mathbf{I} - \boldsymbol{\alpha} \otimes \boldsymbol{\alpha} \tag{21}$$

and λ is a nondimensional scalar microstructural parameter. This parameter takes a relatively simple form when the lattice reference frame is appropriately chosen so that $\boldsymbol{\alpha}$ bisects the acute angle subtended by the slip directions

$$\lambda = \frac{\tilde{Q}_{12}}{\tilde{P}_{12}} \tag{22}$$

where $\tilde{Q}_{12} = \tilde{Q}_{12}^{(1)} = \tilde{Q}_{12}^{(2)}$ and $\tilde{P}_{12} = \tilde{P}_{12}^{(1)} = \tilde{P}_{12}^{(2)}$ are the components of the Schmid orientation tensors relative to the basis $\{\boldsymbol{\alpha}, \boldsymbol{\alpha}_\perp\}$. Equation (19) can be rewritten as

$$\begin{aligned} \mathring{\boldsymbol{\alpha}} &= \dot{\boldsymbol{\alpha}} - \boldsymbol{\omega}\boldsymbol{\alpha} = \lambda\mathbf{d}\boldsymbol{\alpha} - \lambda(\boldsymbol{\alpha}\cdot\mathbf{d}\boldsymbol{\alpha})\boldsymbol{\alpha} \\ &= \lambda[(\mathbf{d}(\boldsymbol{\alpha}\otimes\boldsymbol{\alpha}) - (\boldsymbol{\alpha}\otimes\boldsymbol{\alpha})\mathbf{d})]\boldsymbol{\alpha}. \end{aligned} \tag{23}$$

So

$$\boldsymbol{\omega}^{\mathrm{P}} = \lambda[(\boldsymbol{\alpha}\otimes\boldsymbol{\alpha})\mathbf{d} - \mathbf{d}(\boldsymbol{\alpha}\otimes\boldsymbol{\alpha})]. \tag{24}$$

Here, several features of the limit behavior of the microstructural parameter for single crystals give a geometric interpretation consistent with single slip. The ratio in (22) indicates λ is a scalar measure of the amount of material spin relative to the amount of shearing within a crystal subjected to an applied deformation field. Due to the symmetry of the dual slip system arrangement, λ will vary continuously in a one-to-one correspondence with the acute angle, 2β, between the slip directions where $1 < \lambda < \infty$ for $0 < \beta < \pi/4$ as illustrated in Figure 3. Further, the variation of λ with β indicates that λ never vanishes. Thus, from (20), no crystal undergoing double slip can accommodate a prescribed deformation without some plastic spin. Therefore, there can be no inherently isotropic limit for double slip planar single crystals, *i.e.* no slip system arrangement that will allow the crystal to spin with the

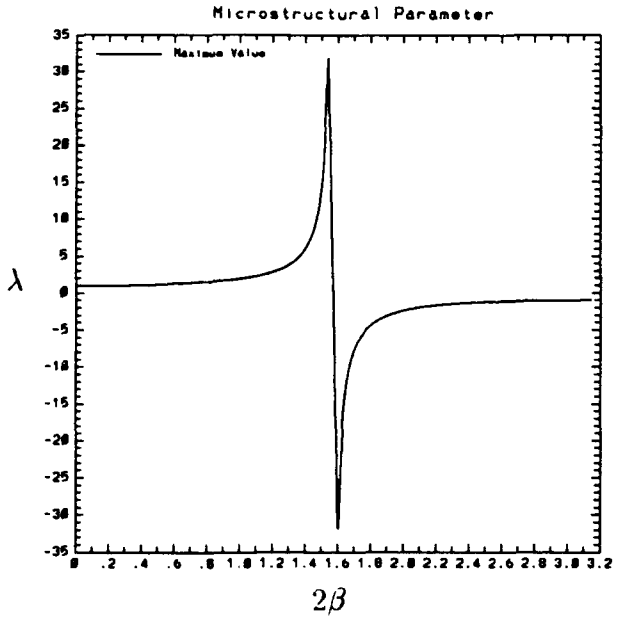

Figure 3: Variation of the microstructural parameter λ with slip system separation 2β

macroscopic spin of the material point for all arbitrarily applied deformation fields.

There are then two explicit factors affecting the individual grain reorientation. First, the mean field assumption which directly affects the update relation (19) through ω. Second, the geometric characteristic of the grain, λ, which dictates the degree to which the crystal will accommodate deformation through shearing and spin. With these effects quantified and separated, populations of grains can be considered at the material point, providing natural measures for a continuum level description of anisotropic material properties.

6 The Orientation State

Considering a distribution of grain orientations to be representative of the aggregate, the ODF is the most general continuous description of the crystal orientation state underlying the continuum point. The orientation distribution $A(\boldsymbol{\alpha})$ is defined so that $A(\boldsymbol{\alpha})d\boldsymbol{\alpha}$ is the probability that a grain with director vector $\boldsymbol{\alpha}$ is in the infinitesimal sector $d\boldsymbol{\alpha}$ centered at $\boldsymbol{\alpha}$. Because the subspace of possible orientation states is closed, the grain orientation can be regarded as a conserved quantity. Consequently its local change is governed by the conservation equation

$$\dot{A}(\boldsymbol{\alpha}) + A(\boldsymbol{\alpha})\,\mathrm{div}(\dot{\boldsymbol{\alpha}}) = 0. \tag{25}$$

One efficient method for tracking the induced anisotropy with a limited set of parameters has been to expand the ODF over an appropriately chosen set of basis functions (Advani and Tucker(1987), Onat and Leckie (1988)). What results is an infinite series whose tensor coefficients represent progressively higher moments of the distribution. A convenient set of basis functions is provided by the deviatoric subspace of dyadic products of $\boldsymbol{\alpha}$. Such basis functions provide a special symmetric, traceless set of corresponding orientation moment tensors which recover the distribution function. Expanding about the isotropic state and retaining only the first moment, we obtain

$$A(\boldsymbol{\alpha}) = \frac{1}{2\pi} + \frac{2}{\pi}\mathcal{A}_{ij} f_{ij}(\boldsymbol{\alpha}), \tag{26}$$

where

$$f_{ij}(\boldsymbol{\alpha}) \;=\; \alpha_i\alpha_j - \frac{1}{2}\delta_{ij} \tag{27}$$

and

$$\mathcal{A}_{ij} \;=\; \oint A(\boldsymbol{\alpha}) f_{ij}(\boldsymbol{\alpha}) d\boldsymbol{\alpha}. \tag{28}$$

Such basis functions are appealing for several reasons. First, they are general, depend on no particular orientation state or frame of reference, and transform as tensors. Thus, for deformation paths leading to anisotropy whose principal directions may vary, one can follow the axes of the developing anisotropy directly. Second, the lower moment tensors provide an approximate means by which to characterize the fixed state anisotropy with a limited number of independent components. Third, when properly chosen, they allow the fully isotropic description to be lumped into a single term of the series. Finally, the evolution equations for the moment tensors follow directly from the conservation equation and their solution provides a means to update the material state.

6.1 Orientation Moment Evolution Equations

One of the advantages of employing the moment tensors to describe the orientation distribution is our ability to evolve their components with continued deformation. As outlined by Advani (1987) there are several methods by which to obtain such equations. Here we start with the evolution equation for the orientation of a single grain and combine this with the continuity equation. Substituting (26) for the ODF and the definition (28) of the orientation tensor, an objective evolution equation for the second order moment tensor results:

$$\dot{\mathcal{A}} = \boldsymbol{\omega}\mathcal{A} - \mathcal{A}\boldsymbol{\omega} + \lambda(\mathbf{G} + \mathbf{d}) - 2\lambda\mathbf{a} : \mathbf{d}, \tag{29}$$

where

$$\mathbf{G} = \mathbf{d}\mathcal{A} + \mathcal{A}\mathbf{d} \tag{30}$$

and

$$\mathbf{a} = a_{ijkl}\ \mathbf{e}_i \otimes \mathbf{e}_j \otimes \mathbf{e}_k \otimes \mathbf{e}_l \tag{31}$$

$$a_{ijkl} = \oint A(\boldsymbol{\alpha}) \alpha_i \alpha_j \alpha_k \alpha_l d\boldsymbol{\alpha}. \tag{32}$$

6.2 Closure Approximation

As a natural consequence of this procedure, however, the evolution equation for the second order tensor depends on the current value of the fourth order tensor. Therefore a closure approximation is necessary to resolve a complete set of equations. Various types of closure approximation have been discussed previously (Advani and Tucker (1990)). For illustrative purposes, we adopt the simplest linear closure rule which corresponds to the deviatoric portion of the fourth order tensor vanishing (Advani and Tucker (1987, 1990)). The objective rate then becomes

$$\mathring{\mathcal{A}} = \dot{\mathcal{A}} - \boldsymbol{\omega}\mathcal{A} + \mathcal{A}\boldsymbol{\omega} = \frac{\lambda}{2}\mathbf{d}. \tag{33}$$

This is consistent with the truncated series adopted in (26). With the rate written in terms of a microstructural constitutive parameter and the kinematic field variables, we now have the means to update the developing texture with continued deformation.

7 Continuum Plastic Spin

In discrete polycrystalline simulations, macroscopic quantities such as the continuum stress are evaluated as a weighted average of the grain stress over all orientations. The direct analog in a continuous model is provided by the orientation average. For the plastic spin of the crystal this average is

$$\mathcal{W}^{\mathrm{P}} = \oint A(\boldsymbol{\alpha}) \boldsymbol{\omega}^{\mathrm{P}}(\boldsymbol{\alpha}) d\boldsymbol{\alpha} \tag{34}$$

Using (24) and (28)

$$\mathcal{W}^{\mathrm{P}} = \lambda(\mathcal{A}\mathbf{d} - \mathbf{d}\mathcal{A}) \tag{35}$$

This result has several important features. It is based on a simple and definite model of polycrystalline slip and an equally clear and definite characterization of the anisotropy of the aggregate. The orientation average provides expression (35) directly and no heuristic averaging arguments are needed.

The microstructural significance of the parameter λ and the second rank tensor $\mathcal{A}$ are known; λ is determined purely by the geometry of slip planes in the crystal lattice frame and the second moment tensor can be continually updated with the evolution equation discussed in section 6.1. Questions that remain concern the restriction to two dimensions, the accuracy of the approximation to the distribution function, and the correctness of the closure assumption made when generating the evolution equation.

Expressions for the plastic spin that result from heuristic micromechanical arguments involving single slip and dislocation substructure also have the structure of (35) (Dafalias and Aifantis (1986), Bammann and Aifantis (1987), Dafalias (1990)). However, because the second rank tensor quantifying the internal structure is identified as a back stress, it is not clear how these expressions for the plastic spin relate to a plastic spin based on polycrystalline slip. Equation (35) has the same form as phenomenological expressions proposed earlier by Dafalias (1985) and Loret (1983) using a second order "structure tensor" and an arbitrary parameter.

One of the key features of any anisotropic constitutive model is its ability to determine the orientation of the principal directions of the anisotropy. This provides one reason to focus on the average plastic spin; it enters naturally in expressions for the relative spin of the axes of anisotropy (Zbib and Aifantis (1988)). In fact, the orientation average of the lattice spin is the difference between the macroscopic spin and the average plastic spin.

$$\begin{aligned} W &= <\omega'> \\ &= \omega - <\omega^{\mathrm{p}}> \\ &= \omega - \lambda(\mathcal{A}\mathbf{d} - \mathbf{d}\mathcal{A}). \end{aligned} \tag{36}$$

When simple shear is initiated in an initially isotropic distribution, the average plastic spin vanishes and the eigenvectors of the second moment tensor begin to spin with the macroscopic spin. This is also true in general for initially textured aggregates when $\mathcal{A}$ and $\mathbf{d}$ are coaxial. With continued shearing, the average plastic spin approaches the macroscopic spin and the eigenvectors of the moment tensor approach stable positions in orientation space (Prantil (1991)).

An averaging argument employed by Dafalias (1985) has been used by Aravas and Aifantis (1991) to obtain an expression for this relative spin. They assume that the spin of the eigenvectors of the "structure tensor" corresponds to a weighted average of the spins of "material fibers" instantaneously underlying the eigenvectors. When the microstructural parameter derived here is chosen as the scaling parameter for the spin of the material fibers, the resulting expression for the relative spin takes the form of (36).

8 Conclusions

Using a relatively simple polycrystalline model, we link the anisotropy on the microstructural level to that on the macroscopic level. In particular, three features of this new approach are of interest. First, we identify a microstructural parameter for the grain. It characterizes the single crystal anisotropy in terms of the geometry of slip systems active in plastic flow. Second, we introduce the second moment of the orientation distribution function as the measure of material anisotropy and use polycrystalline theory to derive its evolution equation. Third, we calculate the average plastic spin of the polycrystalline aggregate and write it in terms of the moment tensor, the macroscopic flow and the microstructural parameter. On the continuum level, the averaged plastic spin provides the constitutive information necessary to track the principal directions of the developing anisotropy.

References

[1] Advani, S. G. and Tucker, C. L. "The Use of Tensors to Describe and Predict Fiber Orientation in Short Fiber Composites," *J. Rheol.*, **31**, 751-784, 1987.

[2] Advani, S. G. and Tucker, C. L. "Closure Approximations for Three-Dimensional Structure Tensors," *J. Rheol.*, **34**, 367-386, 1990.

[3] Aravas, N. and Aifantis, E. C. "On the Geometry of Slip and Spin in Finite Plastic Deformation," *Intl. J. Plast.*, **7**, 141-160, 1991.

[4] Arminjon, M. "Sur le Champ de Rotation des Cristaux dans un Polycristal Déformé Plastiquement," *Journal de Mécanique Théorique et Appliquée*, **6**, no. 4, 511-523, 1987.

[5] Asaro, R. J. "Micromechanics of Crystals and Polycrystals," *Advances in Applied Mechanics*, **23**, 1-115, 1983a.

[6] Asaro, R. J. "Crystal Plasticity," *J. Appl. Mech.*, **50**, 554, 1983b.

[7] Bammann, D. J. and Aifantis, E. C. "A Model for Finite-Deformation Plasticity," *Acta Mechanica*, **69**, 97, 1987.

[8] Clément, A. "Prediction of Deformation Texture Using a Physical Principle of Conservation," *Mater. Sci. Engin.*, **55**, 203-210, 1982.

[9] Dafalias, Y. F. "The Plastic Spin," *J. Appl. Mechanics*, **52**, 865, 1985a.

[10] Dafalias, Y. F. "A Missing Link in the Macroscopic Constitutive Formulation of Large Plastic Deformations," in Sawczuk, A. and Bianchi, G. (eds.), *Plasticity Today*, Elsevier, Appl. Sci., U.K., pp. 135-151, 1985b.

[11] Dafalias, Y. F. and Aifantis, E. C. "On the Origin of Plastic Rotations and Spin," Appendix to the article Aifantis, E. C. "On the Structure of Single Slip and its Implications to Inelasticity" in: Gittus, J. et al. (eds.), *Physical Basis and Modeling of Finite Deformations of Aggregates*, Elsevier Appl. Sci. Publ., Amsterdam, p. 283, 1986.

[12] Dafalias, Y. F. and Aifantis, E. C. "On the Microscopic Origin of the Plastic Spin," *Acta Mechanica*, **82**, 31, 1990.

[13] Loret, B. "On the Effects of Plastic Rotation in the Finite Deformation of Anisotropic Elastoplastic Materials," *Mech. Materials*, **2**, 287.

[14] Onat, E. T. and Leckie, F. A. "Representation of Mechanical Behavior in the Presence of Changing Internal Structure," *J. Appl. Mech.*, **55**, 1-10, 1988.

[15] Prantil, V. C. "A Formalism For Providing A Macroscopic Measure Of Material Anisotropy Based On Polycrystalline Theory," Ph.D. Thesis, Cornell University, Ithaca, New York, in preparation.

[16] Taylor, G. I. " Plastic Strain in Metals," *J. Inst. Metals*, **62**, 307, 1938.

[17] Zbib, H. M. and Aifantis, E. C. "On the Concept of Relative Spin and its Implications to Large Deformation Theories. Part I: Hypoelasticity and Vertex-Type Plasticity," *Acta Mechanica*, **74**, 15, 1988a.

[18] Zbib, H. M. and Aifantis, E. C. "On the Concept of Relative Spin and its Implications to Large Deformation Theories. Part II: Anisotropic Hardening Plasticity," *Acta Mechanica*, **74**, 35, 1988b.